Development of highly scattering distributed fibre optic sensing for structural health monitoring

Wang, X.

DOI
10.4233/uuid:16e5e2f5-e491-4f86-8a47-6ee0c9ffd000

Publication date
2023

Document Version
Final published version

Citation (APA)
Wang, X. (2023). *Development of highly scattering distributed fibre optic sensing for structural health monitoring*. [Dissertation (TU Delft), Delft University of Technology]. https://doi.org/10.4233/uuid:16e5e2f5-e491-4f86-8a47-6ee0c9ffd000

Development of Highly Scattering Distributed Fibre Optic Sensing for Structural Health Monitoring XIANG WANG

Development of Highly Scattering Distributed Fibre Optic Sensing for Structural Health Monitoring

XIANG WANG
王 翔

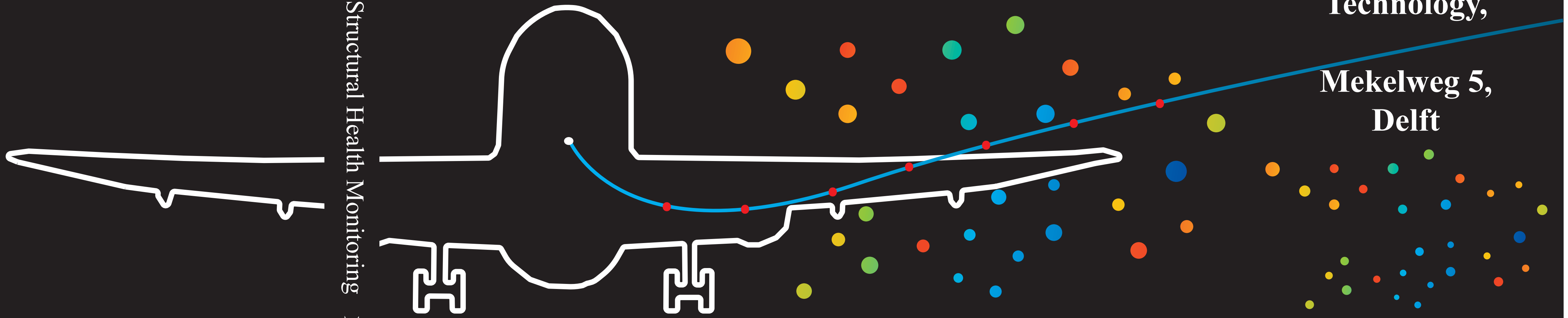

Development of Highly Scattering Distributed Fibre Optic Sensing for Structural Health Monitoring

INVITATION

On Monday,
13 March 2023
at 12:30

in the Senate Hall of
the Aula of the
Delft Universtiy of
Technology,

Mekelweg 5,
Delft

XIANG WANG

DEVELOPMENT OF HIGHLY SCATTERING DISTRIBUTED FIBRE OPTIC SENSING FOR STRUCTURAL HEALTH MONITORING

DEVELOPMENT OF HIGHLY SCATTERING DISTRIBUTED FIBRE OPTIC SENSING FOR STRUCTURAL HEALTH MONITORING

Dissertation

for the purpose of obtaining the degree of doctor
at Delft University of Technology,
by the authority of the Rector Magnificus Prof.dr.ir. T.H.J.J. van der Hagen,
chair of the Board for Doctorates,
to be defended publicly on
Monday 13 March 2023 at 12.30 o'clock

by

Xiang WANG

Master of Engineering in Optical Engineering, Beihang University, China
born in Jiangsu, China

This dissertation has been approved by the promotors.

Composition of the doctoral committee:

Rector Magnificus,	chairperson
Dr. R. M. Groves,	Delft University of Technology, promotor
Prof. dr. ir. R. Benedictus,	Delft University of Technology, promotor

Independent members:

Dr. ir. R. Loendersloot	University of Twente
Prof. dr. A. Güemes	Polytechnic University of Madrid
Prof. dr. S. J. Watson	Delft University of Technology
Prof. dr. B. R. Brandl	Delft University of Technology
Dr. ir. S. F. Pereira	Delft University of Technology

Keywords: optical fibre sensor, structural health monitoring, strain sensing, nanoparticle, light scattering
Printed by: Ipskamp Printing

ISBN 978-94-6366-663-3

An electronic version of this dissertation is available at
http://repository.tudelft.nl/.

To my beloved parents

CONTENTS

SUMMARY

In this thesis, fibre optic sensing has been investigated as an important technique for structural health monitoring. Distributed fibre optic sensing based on Rayleigh scattering is a fibre optic sensing technique to achieve the spatially continuous strain monitoring for critical locations for the structures.

However, the Rayleigh backscattering intensity in commercial optical fibres is low which is a limitation to Rayleigh scattering based fibre optic sensing. In recent years, methods to improve the intensity of the backscattered light in optical fibres have been proposed. By doping nanoparticles into the optical fibre, the backscattered light increases dramatically. Then, the signal-to-noise ratio may increase which would be beneficial for strain measurement with this Rayleigh scattering based method for structural health monitoring.

The main research question is 'how can the enhancement of light scattering used in distributed fibre optic sensing be an advantage for structural health monitoring'. The aim of this research is to develop the enhancement of light scattering in the distributed fibre optic sensing as an advantage for structural health monitoring. Gold spherical nanoparticles were chosen as the contrast agents for backscattered light enhancement. The spectral characteristics (light intensity, spectral shift, etc.) have been investigated in detail in this thesis.

In this dissertation, firstly, a model of light scattering by gold nanoparticles at optical fibre interfaces was proposed to overcome the difficulty of manufacturing nanoparticle doped optical fibre in an optical laboratory. Gold nanoparticle liquids were dropped to the optical fibre interfaces to evaluate the backscattered light levels from the nanoparticles.

Secondly, a model of light scattering by gold nanoparticles in the core of the optical fibres was proposed and an optimisation of light scattering enhancement by gold nanoparticles in fused silica optical fibres was investigated. By comparing the models of light scattering by gold nanoparticles in the core of the optical fibres and at optical fibre interfaces, the relationship between them has been built to evaluate the light scattering level in the optical fibre from the results obtained from the optical fibre interfaces.

Then, the characteristics of the backscattered light spectra from the nanoparticle doped optical fibres and the characteristics of the spectral shift under axial strain were investigated. The backscattered light spectral shifts have been compared with the cases of commercial optical fibres and fibre Bragg gratings.

A case study of strain acquisition of gold nanoparticle doped distributed optical fibre sensing based on backscattering was investigated with different typical gauge lengths and spectral ranges. Different noise levels were applied to the spectra to analyse the influence on the strain acquisition with signal-to-noise ratio improvement.

Lastly, due to the use of gold as the material for nanoparticles, plasmon resonance is induced by gold nanoparticles. The plasmon resonance based gold nanoparticle doped optical fibre strain sensing was studied to make it a potential auxiliary strain detection method along with distributed fibre optic sensing based on Rayleigh scattering.

SAMENVATTING

In deze thesis, is glasvezeldetectie onderzocht als een techniek om de structurele gezondheid te monitoren. Glasvezeldetectie op basis van Rayleigh-verstrooiing is een glasvezeldetectie techniek die het mogelijk maakt om ruimtelijk doorlopende deformatie langs de vezel te monitoren. Hiermee kan een structuur continu bewaakt worden op kritieke locaties voor de constructies.

De toegepaste techniek is echter gebaseerd op de Rayleigh-terugverstrooiingg in de optische vezel. Over het algemeen is de terugverstrooiing in de commerciële optische vezel laag, wat een beperking is voor deze methode. De laatste jaren zijn methoden voorgesteld om de intensiteit van het terugverstrooide licht in de optische vezels te verbeteren. Door nanodeeltjes op de optische vezel te doteren, zal het terugverstrooide licht drastisch toenemen. Dit verbeterd de signaal-ruisverhouding, wat gunstig is voor het meten van deformatie met deze, op Rayleigh-verstrooiing gebaseerde, methode voor structurele gezondheidsmonitoring.

Het doel van dit onderzoek is om de verbetering van lichtverstrooiing in de gedistribueerde glasvezeldetectie een voordeel te maken voor structurele gezondheidsmonitoring. Gouden sferische nanodeeltjes zijn gekozen als contrastmiddelen voor de verbetering van de lichtverstrooiing. Hierbij zijn in deze thesis de spectrale kenmerken in detail onderzocht.

In dit proefschrift is allereerst een model van lichtverstrooiing door gouden nanodeeltjes op optische vezelinterfaces voorgesteld. Hiermee is het vervaardigen van met nanodeeltjes gedoteerde optische vezel in een optisch laboratorium mogelijk gemaakt. Vloeistoffen met gouden nanodeeltjes zijn op de optische vezelinterfaces gedotteerd om de terugverstrooide lichtniveaus van de nanodeeltjes te evalueren.

Ten tweede is een model van lichtverstrooiing door gouden nanodeeltjes in de kern van de optische vezels voorgesteld. Ook is de optimalisatie van de lichtverstrooiing door gouden nanodeeltjes in optische vezels van gesmolten silica onderzocht. Door het model van lichtverstrooiing door gouden nanodeeltjes in de kern van de optische vezels en op optische vezelinterfaces te vergelijken, is de relatie tussen deze twee opgebouwd.

Vervolgens zijn de kenmerken van de terugverstrooide lichtspectra van de met nanodeeltjes gedoteerde optische vezels onderzocht. Hierbij is ook gekeken naar de spectrale verschuiving van terugverstrooid licht onder axiale deformatie. Deze verschuivingen zijn vergeleken met die van commerciële optische vezels en Bragg Gratings.

Een casus is uitgevoerd om de deformatiemetingen van de met gouden nanodeeltjes gedoteerde gedistribueerde optische vezeldetectie op basis van terugverstrooiing te onderzoeken voor verschillende typische meetlengtes en spectrale bereiken. Verschillende ruisniveaus zijn toegepast op de spectra om de invloed op de deformatiemetingen te analyseren met een verbetering van de signaal ruisverhouding.

Ten slotte is, door het gebruik van goud als materiaal voor de nanodeeltjes, de plasmonresonantie geïnduceerd. De op plasmonresonantie gebaseerde goud nanodeeltjes gedoteerde optische deformatiemetingen is bestudeerd om er een potentiële aanvullende deformatiemeetmethode van te maken, samen met gedistribueerde glasvezeldetectie op basis van Rayleigh-verstrooiing.

1

INTRODUCTION

1.1. BACKGROUND

Distributed fibre optic sensing can obtain parameters such as strain, temperature, etc. for structural health monitoring (SHM) [1], [2] by using the light scattering, for example Rayleigh scattering, Brillouin scattering, and Raman scattering [3]. Distributed fibre optic sensors not only have the advantages of optic sensors, such as small size, low weight, immunity to electromagnetic interference etc., but also have the advantages of having the ability to acquire information along the whole length of the sensing fibre, which corresponds to hundreds or thousands of sensors existing in the sensing fibre. For different applications, a variety of distributed fibre optic sensing systems have been developed according to different principles. These distributed fibre optic sensing systems realise the measurement for different measurement ranges, from centimetres to hundreds of kilometres, and for different spatial resolutions, from millimetres to several hundreds of meters [3]. Therefore, they can be used in different fields.

Structural health monitoring is mainly used in civil engineering [3] (bridge, building, etc.), vehicles [4], watercrafts [5], aircrafts [6] (aeroplanes, unmanned air vehicles [7]), etc. For the applications of SHM for aircraft, distributed fibre optic sensors are mainly used for strain monitoring in structural elements [8], and shape reconstruction based on strain [9] and damage detection [10]. High spatial resolution and high sensitivity to strain play an important role in these applications and are also beneficial for SHM [5], [9].

Distributed fibre optic sensing based on Rayleigh scattering with an optical frequency domain reflectometer (OFDR) [11] has as high as millimetre spatial resolution for strain/temperature detection [12]. With its high spatial resolution and strain or temperature resolution, it has been used for SHM to detect small deformations, debonding [13], etc. Some scholars [14]–[16] point out that the weak Rayleigh scattering signal is the limitation to this type of sensing.

However, the situation of low Rayleigh scattering in optical fibre has been changing. In recent years, some methods have been implemented to overcome this issue.

For example, using ultraviolet (UV) laser exposure (213 nm wavelength) [14] or femtosecond laser radiation (800 nm wavelength) [15] to increase the scattered light in optical fibre. These methods can improve the distributed fibre optic sensors' sensitivity to strain/temperature or its stability at high temperatures. With this sensitivity improvement, distributed sensing has been used for applications which need precise strain information such as for shape sensing for bio-medical devices [17], [18]. If these scattering enhancement techniques are used for the monitoring of materials, this more precise strain information along with a higher spatial resolution may be beneficial for the SHM for material and structural monitoring.

Introducing nanometre size to micrometre size particles into optical fibre has the potential of increasing the scattered light dramatically because with an increase in small size particles (from nanometres to micrometres) in the optical fibre, the Rayleigh scattered light has the possibility to increase and for larger particles has the tendency to transit to Mie scattering whose intensity is much greater than Rayleigh scattering. Some previous research has partly verified this idea. For example, some researchers used nanoparticles (NPs) as contrast agents in tissues [19], [20]. In recent years, by doping nanoparticles [21], [22], the backscattered light intensity increase in the core of optical fibres has been obtained [18], [23], for example doping magnesium oxide (MgO) NPs [24]. These preliminary results show the potential of making use of particles to overcome the drawback of current distributed fibre optic sensing based on Rayleigh scattering.

This research will be based on the assumption that low Rayleigh scattering is the limitation to distributed fibre optic sensing. Introducing small particles into an optical fibre will be explored to enhance the scattered light in optical fibres. The improvement of these highly scattering optical fibres is expected to be used in SHM.

1.2. RESEARCH QUESTIONS

The main research question and four sub-research questions for the main research question were identified at the beginning of this research and are listed here. Further details of the reasons for choosing these questions will be described in the next chapter.

Main research question: How can the enhancement of light scattering used in distributed fibre optic sensing be an advantage for SHM?

To answer the main research question, four sub-research questions were proposed at the Go/NoGo meeting in the first year of my PhD study and are listed below:

Question 1: What are the potential methods to enhance the intensity of scattered light in optical fibre in distributed fibre optic sensing detected based on the conventional LUNA (LUNA Innovations Company) interrogator available in the laboratory?

Question 2: If nanometre to micrometre size particles are introduced into an optical fibre, what is the intensity characteristic of the scattered light in optical fibre with these particles?

Question 3: The increased scattered light is also likely to reduce the transmission of light along the optical sensing fibre. What is the optimised scattering increase at some key areas?

Question 4: What is the effect of the sensitivity change and their effect for SHM for material?

The first question is related to the methods for backscattered light enhancement. The second question is related to the characteristics of the scattered light from small particles in optical fibre. The third question is related to the whole length scattered light enhancement as a preparation for application. The fourth question is about applications with these techniques. Unfortunately, the final goal of making light scattering enhancement being an advantage for SHM cannot be reached even if the four sub-research questions are answered because there are gaps between the sub-research questions when the research is implemented. To bridge these gaps, much work has been done in addition to the scope of the initial proposed sub-research questions and details will be shown in the following chapters. In order to make the thesis' story clear, a thesis outline is presented below, which includes the main contents of the following chapters and the methodology used for reaching the answers to the main research question.

1.3. THESIS OUTLINE

This thesis is mainly divided into the following chapters:

Chapter 2 (Literature review):

In this chapter, a brief literature review will be given. The concept of structural health monitoring will be introduced first followed by the reasons why structural health monitoring is needed for engineering. The different optical fibre sensing technologies and especially distributed fibre optic sensing will be introduced and the advantages of distributed fibre optic sensing based on Rayleigh backscattering will be presented. Some applications of distributed fibre optic sensing for SHM based on Rayleigh scattering will be shown. A state of the art of distributed fibre optic sensing based on Rayleigh scattering will be discussed from the aspect of overcoming the low backscattering signal in the optical fibre in recent years.

From Chapter 3 to Chapter 7, the NP doping method is chosen to be investigated to enhance the backscattered light in the optical fibres and to make these NP-doped optical fibre sensors to be an advantage for SHM.

Chapter 3 (Modelling of light scattering by gold NPs at optical fibre interfaces):

In this chapter, the characteristics of the intensity of backscattered light by the gold NPs will be investigated. A scattered light coupling model for the setup of dropping refractive index matching liquid containing NPs onto optical fibre interfaces will be proposed. Experiments with commercial gold NP suspensions are used to evaluate the model. By simulated results from modelling and using an experimental case study of different sizes of gold NPs, it is expected to obtain some insights in choosing NPs for NP-doped optical fibre sensors from the aspect of increasing the backscattering intensity.

Chapter 4 (Optimisation of light scattering enhancement by gold nanoparticles in fused silica optical fibre):

In this chapter, the characteristics of the intensity of backscattered light by the gold NPs will continue to be studied based on the model which is presented in Chapter 3. A model of backscattering light in the core of NP-doped optical fibre will be proposed and the relationship between the light scattering model at optical fibre interfaces and the light scattering model in the optical fibre will be obtained. The optimised sizes for light scattering enhancement will be investigated with or without consideration of the penetration depth.

Chapter 5 (Spectral characteristics of gold nanoparticle (NP) doped optical fibre under axial strain):

In this chapter, further spectral characteristics (spectral shift, spectral fluctuations, spectral intensity) of NP-doped fibre optic sensors will be investigated.

Chapter 6 (Case study of strain acquisition of gold nanoparticle doped distributed optical fibre sensing based on backscattering):

The accuracy and sensitivity of strain detection with NP-doped optical fibres will be investigated with the traditional cross-correlation method. By setting specific noise levels to change the signal to noise ratios of the detected spectral signals, the sensitivity or namely the minimum spectral shift which corresponds to the minimum strain can be detected will be investigated.

Chapter 7 (Plasmon resonance based gold nanoparticle doped optical fibre strain sensing):

Plasmon resonance caused by gold nanoparticles in the optical fibres will be investigated. The wavelengths of the plasmon resonance and the spectral shift under axial strain will be investigated.

Chapter 8 (Conclusion and recommendations):

Conclusions from this research are presented and some recommendations for future work are given in this chapter.

BIBLIOGRAPHY

[1] J. M. López-Higuera, L. R. Cobo, A. Q. Incera, and A. Cobo, "Fiber optic sensors in structural health monitoring", *Journal of Lightwave Technology*, vol. 29, no. 4, pp. 587–608, 2011.

[2] R. Zinno, S. Artese, G. Clausi, F. Magarò, S. Meduri, A. Miceli, and A. Venneri, "Structural health monitoring (SHM)", in *The Internet of Things for Smart Urban Ecosystems*, Springer, 2019, pp. 225–249.

[3] X. Bao and L. Chen, "Recent progress in distributed fiber optic sensors", *Sensors*, vol. 12, no. 7, pp. 8601–8639, 2012.

[4] S. T. Kreger, N. A. A. Rahim, N. Garg, S. M. Klute, D. R. Metrey, N. Beaty, J. W. Jeans, and R. Gamber, "Optical frequency domain reflectometry: Principles and applications in fiber optic sensing", in *Fiber Optic Sensors and Applications XIII*, International Society for Optics and Photonics, vol. 9852, 2016, 98520T.

[5] H. Murayama, D. Wada, and H. Igawa, "Structural health monitoring by using fiber-optic distributed strain sensors with high spatial resolution", *Photonic Sensors*, vol. 3, no. 4, pp. 355–376, 2013.

[6] R. D. Sante, "Fibre optic sensors for Structural Health Monitoring of aircraft composite structures: Recent advances and applications", *Sensors*, vol. 15, no. 8, pp. 18 666–18 713, 2015.

[7] P. M. Bueno, M. Martinez, C. Rans, and R. Benedictus, "Strain monitoring using a Rayleigh backscattering system for a composite UAV wing instrumented with an embedded optical fiber", *Advanced Materials Research*, vol. 1135, pp. 1–19, 2016.

[8] J. Bussières, M. Martinez, D. Barazanchy, D. Debruyne, and P. Lava, "Load monitoring using a Rayleigh backscattering fiber optic system", in *International conference of Adapative Structures and Technologies, Aruba*, 2013.

[9] C. Xu and Z. Sharif Khodaei, "Shape sensing with Rayleigh backscattering fibre optic sensor", *Sensors*, vol. 20, no. 14, p. 4040, 2020.

[10] A. Datta, M. Augustin, K. M. Gaddikeri, S. Viswamurthy, N. Gupta, and R. Sundaram, "Damage detection in composite aircraft wing-like test-box using distributed fiber optic sensors", *Optical Fiber Technology*, vol. 66, p. 102 651, 2021.

[11] M. Froggatt and J. Moore, "High-spatial-resolution distributed strain measurement in optical fiber with Rayleigh scatter", *Applied Optics*, vol. 37, no. 10, pp. 1735–1740, 1998.

[12] B. Soller, D. Gifford, M. Wolfe, M. Froggatt, M. Yu, and P. Wysocki, “Measurement of localized heating in fiber optic components with millimeter spatial resolution”, in *2006 Optical Fiber Communication Conference and the National Fiber Optic Engineers Conference*, IEEE, 2006.

[13] J. H. L. Grave, M. L. Håheim, and A. T. Echtermeyer, “Measuring changing strain fields in composites with distributed fiber-optic sensing using the optical backscatter reflectometer”, *Composites Part B: Engineering*, vol. 74, pp. 138–146, 2015.

[14] S. Loranger, M. Gagné, V. Lambin-Iezzi, and R. Kashyap, “Rayleigh scatter based order of magnitude increase in distributed temperature and strain sensing by simple UV exposure of optical fibre”, *Scientific Reports*, vol. 5, no. 1, pp. 1–7, 2015.

[15] A. Yan, S. Huang, S. Li, R. Chen, P. Ohodnicki, M. Buric, S. Lee, M. Li, and K. P. Chen, “Distributed optical fiber sensors with ultrafast laser enhanced Rayleigh backscattering profiles for real-time monitoring of solid oxide fuel cell operations”, *Scientific Reports*, vol. 7, no. 1, pp. 1–9, 2017.

[16] P. Lu, S. J. Mihailov, D. Coulas, H. Ding, and X. Bao, “Random fiber gratings fabricated using Fs-IR laser for distributed temperature sensor application”, in *26th International Conference on Optical Fiber Sensors*, OSA, 2018, FA2.

[17] F. Parent, S. Loranger, K. K. Mandal, V. L. Iezzi, J. Lapointe, J. S. Boisvert, M. D. Baiad, S. Kadoury, and R. Kashyap, “Enhancement of accuracy in shape sensing of surgical needles using optical frequency domain reflectometry in optical fibers”, *Biomedical Optics Express*, vol. 8, no. 4, pp. 2210–2221, 2017.

[18] A. Beisenova, A. Issatayeva, I. Iordachita, W. Blanc, C. Molardi, and D. Tosi, “Distributed fiber optics 3D shape sensing by means of high scattering NP-doped fibers simultaneous spatial multiplexing”, *Optics Express*, vol. 27, no. 16, pp. 22 074–22 087, 2019.

[19] C. S. Kim, P. Wilder-Smith, Y. Ahn, L. L. Liaw, Z. Chen, and Y. J. Kwon, “Enhanced detection of early-stage oral cancer in vivo by optical coherence tomography using multimodal delivery of gold nanoparticles”, *Journal of Biomedical Optics*, vol. 14, no. 3, p. 034 008, 2009.

[20] Y. Ponce de León, J. Pichardo-Molina, N. Alcalá Ochoa, and D. Luna-Moreno, “Contrast enhancement of optical coherence tomography images using branched gold nanoparticles”, *Journal of Nanomaterials*, vol. 2012, pp. 1–9, 2012.

[21] W. Blanc and B. Dussardier, “Formation and applications of nanoparticles in silica optical fibers”, *Journal of Optics*, vol. 45, no. 3, pp. 247–254, 2015.

[22] W. Blanc, M. Vermillac, H. Fneich, J. Turlier, M. Cabié, C. Kucera, D. Borschneck, F. Peters, P. Vennéguès, S. Chaussedent, D. R. Neuville, A. Mehdi, J. M. Ballato, and J. Lupi, “Thalium-doped nanoparticles and their properties in silica-based optical fibers”, in *Fiber Lasers and Glass Photonics: Materials through Applications*, S. Taccheo, M. Ferrari, and J. I. Mackenzie, Eds., SPIE, 2018, 106831F.

[23] P. Bulot, O. Cristini, M. Bouet, A. Demol, L. Bigot, G. Bouwmans, S. Plus, R. Habert, G. Laffont, and M. Douay, “OFDR distributed temperature sensing at 800 °C on a fiber with enhanced Rayleigh scattering profile by doping”, in *Bragg Gratings, Photosensitivity and Poling in Glass Waveguides and Materials*, Optical Society of America, 2018, BM3A–2.

[24] C. Molardi, S. Korganbayev, W. Blanc, and D. Tosi, “Characterization of a nanoparticles-doped optical fiber by the use of optical backscatter reflectometry”, in *Advanced Sensor Systems and Applications VIII*, International Society for Optics and Photonics, vol. 10821, 2018, p. 1 082 121.

2

LITERATURE REVIEW

In the manufacturing process or in-service, defects may be generated in the materials or the structures of aircraft. For example, fatigue, corrosion, and impact will cause defects in metallic materials; for composite materials, delamination, debonding, fibre breakage and other defects may occur [1]. These defects may reduce the performance of the originally designed materials or structures and even induce failure or accidents which threaten the safety of the operation of aircrafts [1]. It is important to find the defects which may cause failure/accidents as early as possible to avoid catastrophes and to reduce maintenance costs. For safety reason, generally aircrafts need to obtain regular maintenance. If defects or damage is found, the materials or structures with defects should be repaired or be replaced. In scheduled maintenance, with the advanced non-destructive testing techniques for example ultrasonic inspection [2], laser shearography [3], thermal imaging [4], etc., the technicians can make full use of these techniques to find the issues. However, it is still labour-intensive. In addition, this scheduled maintenance is generally off-line, so the aircrafts are not available during these regular checks. In this case, an automatic online monitoring allows information about the structure of the aircraft to be obtained during the lifetime of the aircraft. The automated approaches will relieve the labour intense and the regular offline maintenance could be replaced by condition based maintenance to reduce the maintenance time and improve the efficiency of the operation of the airlines [1]. Structural health monitoring has been proposed to achieve this goal partly [1]. By using structural health monitoring, it is expected that 40 % of the maintaining time can be saved and the more that 40 % of the maintaining cost can be reduced [1], [5]. In order to achieve structural health monitoring, as key components of the structural health monitoring system, a variety of sensors are implemented or developed and then can be used for structural health monitoring. Among these sensors, the fibre optic sensors developed in this dissertation are one of them which is investigated as strain sensors.

2.1. WHAT IS STRUCTURAL HEALTH MONITORING?

Structural health monitoring (SHM) is defined as 'the integration of sensing and possibly also actuation devices to allow the loading and damaging conditions of a structure to be recorded, analyzed, localized, and predicted in a way that non-destructive testing (NDT) becomes an integral part of the structure and a material' from Christian Boller's expression [6]. The ultimate aim of SHM is to give an automated and real-time assessment of the structure [7].

To provide SHM for the structure, a SHM system needs to be designed and built [8]. A schematic of an SHM system is shown in Figure 2.1. Figure 2.1 is used to illustrate the basic components for SHM and a procedure for SHM. The SHM system shown in Figure 2.1 (adapted from [9]) consists of two monitoring components. They are the monitoring of the structural health and the usage of the structure. The monitoring of the structural health provides information about load and damage on the structure. According to the phrase from Worden and Dulieu-Barton [10], damage is described as 'when the structure is no longer operating in its ideal conditions but can still function satisfactorily'. For example, for metallic materials, corrosion, crack, fatigue and other damages may occur. For composite structures, delamination, debonding, crack and other damages may occur. By SHM, these damages could be detected. There are four levels of damage identification based on the work from Rytter [11]. Level 1 is to justify whether there is damage or not. Level 2 is to justify where is the damage. Level 3 is to estimate the quantification of the damage. Level 4 provides prediction of the residual life of the structure. Damage classification is also important for SHM and the prediction in level 4 may based on the understanding of the characteristic of the damage [10]. Therefore, the level of damage classification is also appended. By load monitoring, the structure is monitored to operate within the designed limit load. Usage monitoring records the historic usage of the structure used for scheduled maintenance.

The data for SHM are from the signals obtained by the sensors attached or embedded in the structure [12]. For example, by the actuation of transducers [13] or loading of the structure [14], the response from the damage will be obtained by the sensors used for SHM. The data for the usage monitoring can be obtained from damage detection sensors and/or from the usage recording. By the health and usage monitoring, the current state of the structure can be obtained. Then to the residual life of the structure may be predicted from the evaluation from the SHM and usage monitoring to make decisions for example organizing maintenance, repairing or replacing the structure.

A specific full system, for example an aeroplane, is composed of sub-components. The sub-components include fuselage, wing, landing gear etc. In order to obtain the damage information better, the optimisation of the integrity monitoring system should be designed for critical positions on the monitored structures using specific types of sensors based on the physical phenomenon of the potential damage. For example, the areas close to the rivet holes in the aluminium fuselage [15] can be the critical positions. The optimisation of the number and the location of the sensors is related to sensor multiplexing and networking is also an important research field for SHM [15]. The data collected by the sensors directly is resource-consuming and

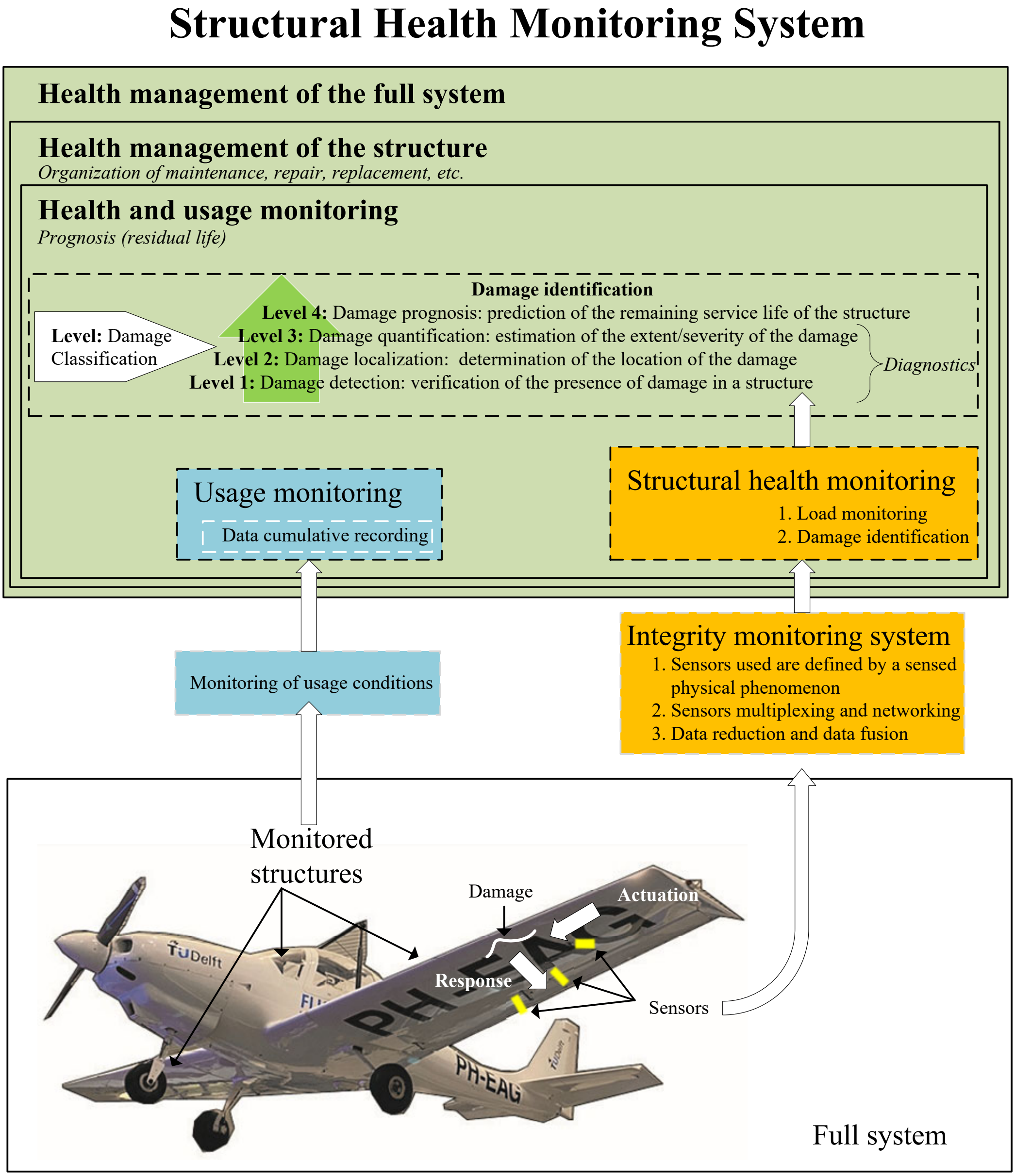

Figure 2.1: Diagram of a structural health monitoring system. (adapted from ref. [9])

needs to have a process of data reduction. By data fusion from multiple sensors or different kinds of sensors, different levels of damage identification can be achieved [16].

2.2. WHY STRUCTURAL HEALTH MONITORING IS NEEDED?

Safety is a reason for introducing SHM and SHM may help to improve the safety. There are some accidents happened in history due to the lacking of effective maintenance or monitoring of the structures. For example, the corrosion induced accident of Aloha Airlines flight 243 and the ill-controlled manufacturing induced collapse of Injak bridge [9]. SHM can be used for monitoring the structures to evaluate for example the heath conditions of the aircraft and the infrastructures. Then, organising effective maintenance to repair or replace the unhealthy structures in order to improve the safety of the structures and to reduce the possibility of the accidents.

SHM is used to in-situ real-time monitoring of the structures. Sensors are embedded or installed on the surfaces of the structures to provide data of the structures [17]. By analysing the data obtained from the SHM system, the health and usage monitoring of the structures can be obtained continuously. It may induce a reduction of the maintenance time for the structures, so it can be more economical, which is a main reason for using SHM [5].

Providing in-situ structure condition for example the shape or load is also an important purpose for SHM. By recording the real-time load or shape, to make sure the structure is operating within the designed load restrictions or deformation restrictions. NASA's Helios wing is a case for the need for monitoring the shape of the wing. As shown in Figure 2.2, the wing broke highly due to the over deformed wing structure [18].


(a) (b)

Figure 2.2: The break of NASA's Helios wing. (a) A photo of NASA's Helios wing. (b) A photo of the break of the wing. [18]

2.3. DISTRIBUTED FIBRE OPTIC SENSING

Optical fibre sensors obtain data from the structure itself or the environment around the sensors. Distributed fibre optic sensing relies on optical fibres to transmit light to the sensing regions in the core of the optical fibres and to sense parameters such as strain, temperature, etc. spatial continuously along the whole length of the sensing fibre [19].

There are many advantages for using distributed fibre optic sensors for SHM. These advantages include the advantages of optical sensors. For example, small size and low weight are its obvious advantages. The diameter of an optical fibre including coating is only about 250 µm for standard single mode fibre and can be smaller that 250 µm (the diameter of the cladding is about 125 µm) [20].For some special optical fibres, the diameters of the cladding can be 40 µm [21] in diameter. With its small size, it has the advantage to be integrated in composite materials [18] to monitor the condition of the material for potentially the whole life cycle of the material. Immunity to electromagnetic interference [22], [23] is another obvious advantage. Fibre optics can be used in a complex electromagnetic environment and can also avoid the problems of wiring [24] for many electrical sensors, such as electrical strain gauges. Distributed optical fibre sensing not only has the advantages of optical sensors, but can detect parameters such as temperature, strain, pressure, vibration etc. along the sensing fibre [25], which means that it can detect every part of the sensing fibre other than discrete points as some optical sensors do [26]. Therefore, with distributed fibre optic sensing, the quantity of the optical sensors used can be decreased dramatically with one sensing fibre because one sensing fibre equals hundreds or thousands of sensors combined together [27].

Fibre Bragg gratings are most widely used fibre optic sensors for structural health monitoring [28]. Compared with distributed fibre optic sensing, an obvious advantage of distributed fibre optic sensing is that the sensing fibre used can be commercial optical fibres for communications (The drawback of this will be discussed below where the development of distributed fibre optic sensing will be investigated.). However, the interrogator hardware for distributed fibre optic sensing is more expensive and bulkier than that for fibre Bragg gratings [29].

According to the different components of scattered light used in distributed fibre optic sensing, distributed fibre optic sensing can be divided into three categories, namely distributed fibre optic sensing based on Rayleigh scattering, Brillouin scattering and Raman scattering as shown in Figure 2.3. (Note, there is normally no large size diameter particles in low-loss optical fibre, so the Mie scattering for small particles is not relevant to consider) [18]. Light scattering is a typical spontaneous scattering spectrum including Rayleigh scattering, Brillouin scattering and Raman scattering.

Rayleigh scattering [30] is caused by the fluctuations of refractive index along the optical fibre. Every optical fibre has its own refractive index fluctuation distribution, which is like the ‘fingerprint’ of the optical fibre [31]. However, Rayleigh scattering cannot be used without calibration of the optical fibre to obtain information such as strain or temperature [32]. It uses the change of scattering signal in a small spatial range to reflect the change of strain or temperature as strain or temperature changes cause a change in the refractive index of the optical fibre [33]. The spectral response of Rayleigh scattering sensing can be divided into temperature and strain compo-

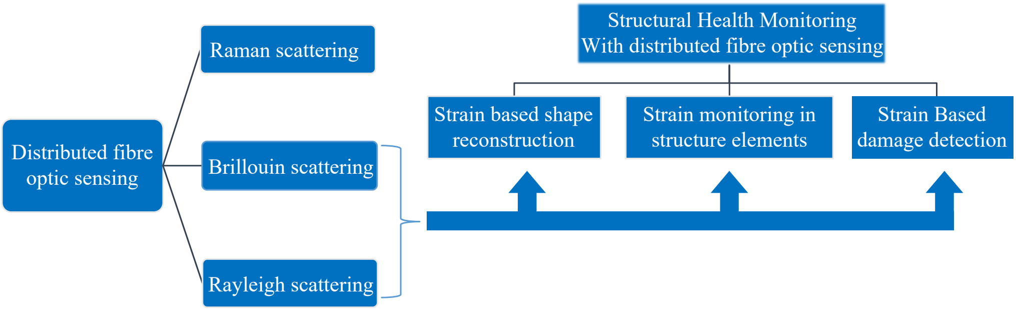

Figure 2.3: The categories of distributed fibre optic sensing based on scattered light and some application fields for structural health monitoring.

nents using an equation similar to that used for fibre Bragg gratings:

$$\frac{\Delta\lambda}{\lambda_B} = K_T \Delta T + K_\varepsilon \Delta\varepsilon, \tag{2.1}$$

where, $\Delta\lambda$ is the wavelength shift caused by strain or temperature change, λ_B is the Bragg wavelength, K_T is the sum of the thermal expansion coefficient and the thermos-optic coefficient, ΔT is the temperature change, K_ε is the strain coefficient and $\Delta\varepsilon$ is the strain change [31].

Distributed fibre optic sensing based on Rayleigh scattering relies on the comparison of Rayleigh signals and Rayleigh backscattering is weak, e.g. $-100\,\mathrm{dB/mm}$ [34], so the weak signal is the main limitation to this form of sensing.

In optical fibres, the power of Brillouin scattering [35] and Raman scattering [36] are even weaker than for Rayleigh scattering. The Brillouin scattering is $15\,\mathrm{dB}-20\,\mathrm{dB}$ weaker than the intensity of Rayleigh scattering and the anti-Stokes Raman signal is the weakest, $20\,\mathrm{dB}-30\,\mathrm{dB}$ weaker than the intensity of Rayleigh scattering [25].

Brillouin scattering is caused by the collective acoustic oscillations in the optical fibre [25]. Distributed fibre optic sensing based on Brillouin scattering uses the Brillouin frequency shift to obtain the strain or temperature not the comparison of intensity. Equation 2.2 is the expression for Brillouin scattering [25]:

$$\Delta\nu_B = C_T \Delta T + C_\varepsilon \Delta\varepsilon, \tag{2.2}$$

where $\Delta\nu_B$ is the Brillouin frequency shift caused by strain or temperature change, C_T is the temperature coefficient and C_ε is the strain coefficient.

Raman scattering uses the ratio of the intensity of the Raman Stokes peak and the anti-Stokes Raman peak to obtain the absolute temperature. Equation 2.3 is the expression used for the temperature calculation from Raman scattering [25]:

$$\frac{I_{AS}}{I_S} = \left(\frac{\lambda_S}{\lambda_{AS}}\right)^4 \exp\left(-\frac{\hbar\omega_m}{k_B T}\right), \tag{2.3}$$

where I_{AS} is the intensity of the anti-Stokes Raman peak, I_S is the intensity of the Raman Stokes peak, λ_{AS} is the wavelength of the anti-Stokes Raman peak, λ_S is the wavelength of the Raman Stokes peak, k_B is the Boltzmann constant, $\hbar$ is the reduced Planck constant and ω_m is the angular frequency for a harmonic oscillator.

Both Rayleigh and Brillouin scattering are sensitive to both temperature and strain, so they are the techniques applied for structural health monitoring. Raman scattering is mainly used for temperature detection [25].

2.4. DISTRIBUTED FIBRE OPTIC SENSING USED FOR STRAIN-BASED STRUCTURAL HEALTH MONITORING

There have been some applications of structural health monitoring for aircraft with the distributed fibre optic sensing methods mentioned above, distributed fibre optic sensing based on Rayleigh scattering and distributed fibre optic sensors based on Brillouin scattering. The main applications included: strain monitoring in structure elements, strain-based shape reconstruction, strain-based damage detection [18], which are also drawn in Figure 2.3. There three topics will be discussed in more detail below.

1. Strain monitoring in structure elements

Distributed fibre optic sensors obtain strain information along the sensing fibre, so they can be used to detect the strain distribution of the structure elements directly. For example, in [18] with distributed fibre optic sensing based on Rayleigh scattering, the dynamic strain detection on composite fan blade was obtained. There was a good agreement of strain between distributed fibre optic sensing and resistance foil strain gauges, with only 3.25 % absolute different observed in dynamic measurement [18].

2. Strain-based shape reconstruction

Excessive deformation will cause the failure of the aircraft, so the monitoring of shape and deformation is an important part of structural health monitoring for aircraft [18]. For example, after the wreckage of NASA(National Aeronautics and Space Administration)'s Helios wing, NASA was aware that excessive wing deformation was probably one reason for the wing breaking. Then a shape detection method with fibre Bragg gratings sensors was developed by NASA Dryden Flight Research Centre [37]. Compared to the fibre Bragg gratings used in strain-based shape reconstruction, the advantage of distributed fibre optic sensor in strain monitoring is that a distributed fibre optic sensor can have a whole length strain detection with even micrometre spatial resolution. However, the temporal resolution is reduced [38]. Therefore, potentially this additional strain data can be used for shape reconstruction.

3. Strain-based damage detection

Damage causes a local strain change and the local strain change can be detected by the distributed strain sensing method. For example, distributed fibre optic sensing has also been used for damage detection based on strain detection. Minakuchi et al. [39] used the Brillouin Optical Correlation Domain Analysis technique to detect failure in carbon fibre reinforced polymer bolted joints. Also using distributed fibre optic sensing based on Rayleigh scattering [40], the debonding in a structural element were investigated.

These applications rely on the spatial resolution and strain sensitivity of the distributed fibre optic sensors. High spatial resolution [41] and strain sensitivity [42] is good for structural health monitoring based on strain detection. As mentioned above, distributed fibre optic sensing based on Rayleigh scattering has a high spatial resolution (millimetres to centimetres), a relatively long sensing range (tens of meters to hundreds of meters), and a high strain sensitivity. It is noticeable that due to some new developments in recent years, the sensitivity and stability of this technique has been improved a lot [43]–[45].

As mentioned before, distributed strain sensing based on Rayleigh backscattering shows a high spatial resolution which is an advantage for strain sensing and the low backscattered light intensity limits this method. This introduces the first sub-research question of this PhD work:

'What are the potential methods to enhance the intensity of scattered light in optical fibre?'

and introduces the main research question:

'How can the enhancement of light scattering used in distributed fibre optic sensing be an advantage for SHM?'

In the next section, a state of the art of light improvement of distributed fibre optic sensing based on Rayleigh scattering will be given.

2.5. STATE OF THE ART OF DISTRIBUTED FIBRE OPTIC SENSING BASED ON RAYLEIGH SCATTERING

As mentioned in Section 2.4, distributed fibre optic sensing based on Rayleigh scattering has a high spatial resolution for strain or temperature sensing. In addition, high resolution and relatively low costs drive the development of distributed fibre optic sensing system based on Rayleigh scattering.

However, some scholars [43]–[45] believe that the weak Rayleigh scattering signal is the restriction to this type of sensing. In recent years, some methods have been implemented to overcome this issue.

Scholars have put forward methods to increase the intensity of Rayleigh scattering by ultraviolet (UV) light exposure of the sensing fibre [43]. A hydrogen-loaded optical fibre was exposed to UV laser light (213 nm wavelength, 50 mW, pulsed irradiation) for several seconds. The Rayleigh scattered light from the optical fibre improved by about 20 dB and the sensitivity of the strain or temperature measurement also improved by an order of magnitude.

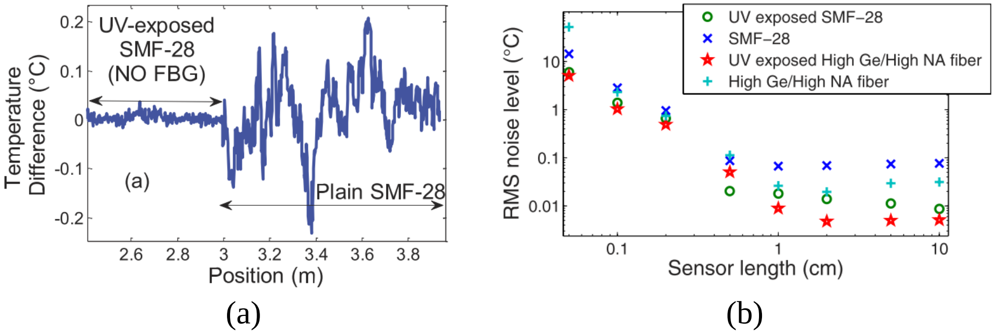

Figure 2.4: The sensitivity improvement by UV exposure on optical fibres. (a) Noise for UV exposed SMF-28 and SMF-28 in a same temperature. (b) Root mean square noise level for different kind of optical fibres in a constant temperature insulated container. [43]

Compared with the single mode fibre (SMF)-28 without UV exposure and a high Germanium(Ge)/high numerical aperture (NA) optical fibre, the optical fibre UV exposure SMF-28 and UV exposure high Ge/high NA optical fibre's noise level improved. According to [43], for a UV exposed high Ge/high NA optical fibre, the best noise level is at about 2 cm, where the equivalent noise level is about 5 mK. For a silica fibre, the factor for strain and temperature is about 8.32 $\mu\varepsilon$/K, so the noise level for strain is only about 40 nε. Figure 2.4 (a) and (b) show the sensitivity improvement with UV exposure on a SMF-28 compared with a SMF-28 via temperature difference in a temperature constant environment and the root mean square (RMS) noise levels for different kind of optical fibres for different gauge lengths. This method promotes the use of distributed fibre optic sensing based on Rayleigh scattering for shape sensing such as enhancing the precision of surgical needle shape track [42] which needs high accuracy.

Irradiation by a femtosecond laser is another way to increase the Rayleigh scattering in optical fibre [44]. A femtosecond laser can cause a microstructure like micro gratings in the optical fibre, which results in the enhancement of Rayleigh backscattering, giving a 40 dB improvement in intensity. This Rayleigh scattering enhancement causes higher stability in a high temperature (800 °C) environment for the detection of temperature. Figure 2.5 (a) and (b) show the experimental setup used for manufacturing microstructures in the core of optical fibres and a photo of the cross-section of a core of optical fibre with these microstructures. In 2018, Lu et al. [45] also used a femtosecond infrared radiation (fs-IR) laser to generate random fibre gratings in an optical fibre improved temperature measurement of root mean square of temperature to 0.001 °C with 10 mm spatial resolution.

The methods mentioned above make defects in the optical fibre to obtain a higher Rayleigh scattering level for strain or temperature measurement. If these scattering enhanced distributed fibre optic sensors are applied to the structural monitoring of materials, the advantages of higher spatial resolution or more sensitivity to strain

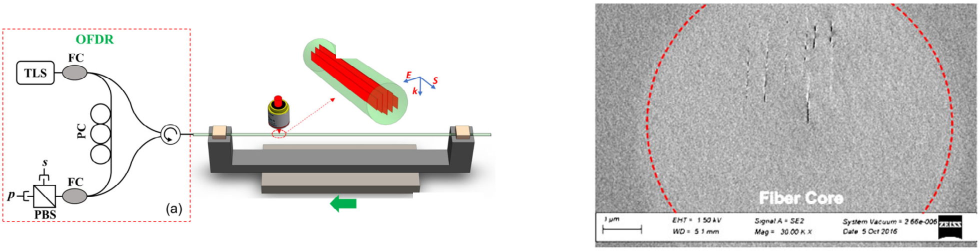

(a) (b)

Figure 2.5: Manufacturing microstructures in an optical fibre with ultrafast laser. (a) The experiment setup to manufacture microstructures. (Tunable laser source (TLS); Fibre coupler (FC); Polarization controller (PC); Polarizing beam splitter (PBS); P-polarized light (p); S-polarized light (s); Optical frequency domain reflectometry (OFDR)); E is the electrical field; k is the direction of light propagation; S is the direction of laser scanning. (b) The microstructures in an optical fibre. [44]

may provide better results for structural health monitoring.

To improve the scattering signal to a higher level, introducing small particles (diameter from several nanometers to several micrometers) into the optical fibre is a potential approach.

With the size of the small particles increasing in the optical fibre, the Rayleigh scattered light has the possibility to increase dramatically and has the tendency to transition to Mie scattering whose intensity is much greater than Rayleigh scattering. Therefore, introducing small particles into an optical fibre may be a way to improve the intensity of the scattered light further, which can overcome the drawback of the low intensity of Rayleigh scattering in optical fibre. It is expected that improving the scattered light intensity using small particles will also increase the sensitivity of the sensing fibre and give more details about strain information over a smaller range.

Recently, Bulto et al. reported that the scattered light in an optical fibre can be increased by doping with zirconia-coated gold nanoparticles [46]. In that conference paper, they observed a 40.6 dB backscattering increase when using the LUNA OBR-4600 system. The developed distributed fibre optic sensor had a better temperature measurement performance at high temperatures than SMF-28 optical fibre without doping nanoparticles. Zirconium dioxide (ZrO_2) nanoparticle-doped optical fibre has also been used for a better high temperature measurement [47]. The error in the temperature range from 200 °C to 800 °C was 5.8 %. In addition, Molardi et.al. pointed out that optical fibre doped with nanoparticles (Magnesium oxide (MgO) nanoparticles, 20 nm-100 nm size) has the same responsivity to strain and temperature [48]. Figure 2.6 (a) and (b) show photos of the core of the MgO nanoparticle-doped optical fibre and the Calcium oxide (CaO) nanoparticle-doped optical fibre. Nanoparticles in the core of the optical fibres increase the backscattered light in the optical fibres.

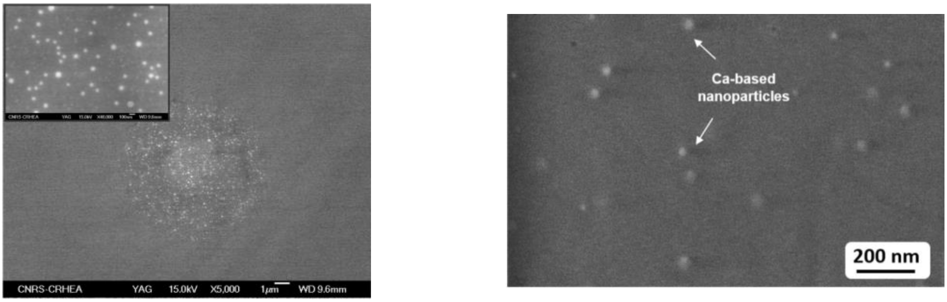

(a) (b)

Figure 2.6: Nanoparticle-doped optical fibres. (a) A photo of the core of a MgO nanparticle-doped optical fibres [48]. (b) A photo of the core of a CaO nanparticle-doped optical fibres. [49]

These are the potential methods to answer sub-research question 1. There methods are 1. UV exposure on optical fibre (there is a high power UV laser (Sirius laser) in our lab); 2. fs-IR irradiation on the optical fibres; 3. Doping nanoparticles into the core of the optical fibres.

In this dissertation, the nanoparticle-doping method was chosen because of its higher backscattered light intensity and its flexibility for example variety of material can be chosen. The first material chosen and for the whole research is gold. As a metallic material, it has potential to show a high reflection. The characteristics of gold nanoparticle-doped optical fibres will be investigated to make the gold nanoparticle-doped optical fibre sensors an advantage for SHM.

What is a suitable situation for nanoparticle doping? This introduces the sub-research question 2:

'If nanometre to micrometre size particles are introduced into an optical fibre, what is the intensity characteristic of the scattered light in optical fibre with these particles?'

and sub-research question 3:

'The increased scattered light is also likely to reduce the transmission of light along the optical sensing fibre. What is the optimised scattering increase at some key areas?'

The performance of the strain sensing based on these nanoparticle-doped sensors is expected to know, which introduces the sub-research question 4:

'What is the effect of the sensitivity change and their effect for SHM for material?'

A complete guideline of the thesis which includes chapter's numbers and the work for these relevant questions is shown in Figure 2.7. In the conclusion chapter, there is also a guideline to conclude this work and recommendations for the future (ref Figure 8.1).

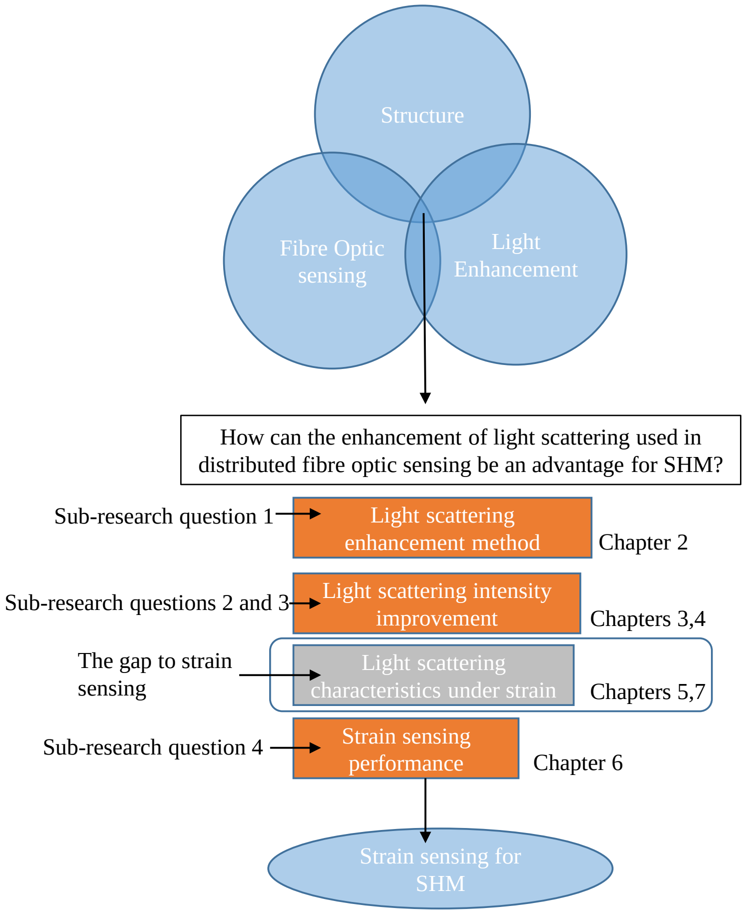

Figure 2.7: The guideline of this work. The research is interdisciplinary research between structure, fibre optic sensing and light enhancement. The main research question was proposed and based on this main research question, the chapters and the relevant questions are labelled in this figure. The purpose of this work is to achieve strain sensing for SHM with the developed method.

2.6. SUMMARY

Structural health monitoring is designed to achieve the goal of automated real-time monitoring of the structures, and recording, analysing, localising, predicting the damage in the structures to assess the prognosis of the residual life and take actions on the maintenance. Sensors play an important role in the SHM system. As one of the sensing methods, distributed fibre optic sensing based on Rayleigh scattering has been widely used for SHM but the limitation of low intensity of backscattered light needs to be overcome. UV exposure and IR radiation on optical fibres are the methods proposed in recent years and can be used for backscattered light enhancement. One potential method is to dope nanoparticles into the core of the optical fibres to increase the backscattered light dramatically and in this research the characteristics of gold nanoparticle-doped optical fibres will be investigated for SHM.

BIBLIOGRAPHY

[1] M. G. Sause and E. Jasiūnienė, *Structural Health Monitoring Damage Detection Systems for Aerospace*. Springer Nature, 2021.

[2] P. Ochôa, I. F. Villegas, R. M. Groves, and R. Benedictus, "Diagnostic of manufacturing defects in ultrasonically welded thermoplastic composite joints using ultrasonic guided waves", *NDT & E International*, vol. 107, p. 102 126, 2019.

[3] D. Francis, R. Tatam, and R. M. Groves, "Shearography technology and applications: A review", *Measurement Science and Technology*, vol. 21, no. 10, p. 102 001, 2010.

[4] P. Shrestha and R. M. Groves, "Image analysis for classification of damaged and undamaged areas on composite structures", in *Nondestructive Characterization and Monitoring of Advanced Materials, Aerospace, Civil Infrastructure, and Transportation XIII*, SPIE, vol. 10971, 2019, pp. 370–377.

[5] A. Güemes, "SHM technologies and applications in aircraft structures", in *Proceedings of the 5th International Symposium on NDT in Aerospace, Singapore*, vol. 1315, 2013.

[6] C. Boller, "Structural health monitoring—an introduction and definitions", *Encyclopedia of structural health monitoring*, 2009.

[7] F. G. Yuan, *Structural health monitoring (SHM) in aerospace structures*. Woodhead Publishing, 2016.

[8] P. Ochôa, R. M. Groves, and R. Benedictus, "Systematic multiparameter design methodology for an ultrasonic health monitoring system for full-scale composite aircraft primary structures", *Structural Control and Health Monitoring*, vol. 26, no. 5, e2340, 2019.

[9] D. Balageas, C. P. Fritzen, and A. Güemes, *Structural health monitoring*. John Wiley & Sons, 2010, vol. 90.

[10] K. Worden and J. M. Dulieu-Barton, "An overview of intelligent fault detection in systems and structures", *Structural Health Monitoring*, vol. 3, no. 1, pp. 85–98, 2004.

[11] A. Rytter, "Vibrational based inspection of civil engineering structures", Fracture and Dynamics, no. 44, 1993, Ph.D. Thesis.

[12] S. Mustapha, Y. Lu, C.-T. Ng, and P. Malinowski, "Sensor networks for structures health monitoring: Placement, implementations, and challenges—a review", *Vibration*, vol. 4, no. 3, pp. 551–585, 2021.

[13] S. Lee, S. Jeong, and J. Park, "Damage identification using flexural vibration actuated and sensed by piezoelectric transducers", *Proceedings of the Institution of Mechanical Engineers, Part C: Journal of Mechanical Engineering Science*, vol. 228, no. 12, pp. 2132–2140, 2014.

[14] Q. Yang, J. Liu, B. Sun, and C. Liang, "Damage localization for beam structure by moving load", *Advances in Mechanical Engineering*, vol. 9, no. 3, pp. 1–6, 2017.

[15] V. Ewald, R. M. Groves, and R. Benedictus, "Transducer placement option of Lamb wave SHM system for hotspot damage monitoring", *Aerospace*, vol. 5, no. 2, p. 39, 2018.

[16] A. A. Broer, R. Benedictus, and D. Zarouchas, "The need for multi-sensor data fusion in structural health monitoring of composite aircraft structures", *Aerospace*, vol. 9, no. 4, p. 183, 2022.

[17] P. M. Ferreira, M. A. Machado, M. S. Carvalho, and C. Vidal, "Embedded sensors for structural health monitoring: Methodologies and applications review", *Sensors*, vol. 22, no. 21, p. 8320, 2022.

[18] R. D. Sante, "Fibre optic sensors for Structural Health Monitoring of aircraft composite structures: Recent advances and applications", *Sensors*, vol. 15, no. 8, pp. 18 666–18 713, 2015.

[19] P. Lu, N. Lalam, M. Badar, B. Liu, B. T. Chorpening, M. P. Buric, and P. R. Ohodnicki, "Distributed optical fiber sensing: Review and perspective", *Applied Physics Reviews*, vol. 6, no. 4, p. 041 302, 2019.

[20] Z. Ding, D. Yang, Y. Du, Y. Zhou, Z. Xu, K. Liu, J. Jiang, and T. Liu, "Note: Improving distributed strain sensing sensitivity in OFDR by reduced-cladding single mode fiber", *Review of Scientific Instruments*, vol. 87, no. 12, p. 126 106, 2016.

[21] N. Takeda, Y. Okabe, J. Kuwahara, S. Kojima, and T. Ogisu, "Development of smart composite structures with small-diameter fiber Bragg grating sensors for damage detection: Quantitative evaluation of delamination length in CFRP laminates using Lamb wave sensing", *Composites Science and Technology*, vol. 65, no. 15-16, pp. 2575–2587, 2005.

[22] S. T. Kreger, A. K. Sang, N. Garg, and J. Michel, "High resolution, high sensitivity, dynamic distributed structural monitoring using optical frequency domain reflectometry", in *Fiber Optic Sensors and Applications X*, SPIE, vol. 8722, 2013, pp. 65–72.

[23] M. J. Nicolas, R. W. Sullivan, and W. L. Richards, "Large scale applications using FBG sensors: Determination of in-flight loads and shape of a composite aircraft wing", *Aerospace*, vol. 3, no. 3, p. 18, 2016.

[24] S. Rapp, L. H. Kang, J. H. Han, U. C. Mueller, and H. Baier, "Displacement field estimation for a two-dimensional structure using fiber Bragg grating sensors", *Smart Materials and Structures*, vol. 18, no. 2, p. 025 006, 2009.

[25] X. Bao and L. Chen, “Recent progress in distributed fiber optic sensors”, *Sensors*, vol. 12, no. 7, pp. 8601–8639, 2012.

[26] R. G. Duncan, B. A. Childers, and V. Rajendran, “High-spatial-resolution temperature monitoring of an industrial motor using a distributed fiber optic sensing technique”, in *Smart Structures and Materials 2004: Smart Sensor Technology and Measurement Systems*, SPIE, vol. 5384, 2004, pp. 258–266.

[27] A. Masoudi and T. P. Newson, “Contributed review: Distributed optical fibre dynamic strain sensing”, *Review of scientific instruments*, vol. 87, no. 1, p. 011 501, 2016.

[28] G. C. Kahandawa, J. Epaarachchi, H. Wang, and K. Lau, “Use of FBG sensors for SHM in aerospace structures”, *Photonic Sensors*, vol. 2, no. 3, pp. 203–214, 2012.

[29] D. Tosi, E. Schena, C. Molardi, and S. Korganbayev, “Fiber optic sensors for sub-centimeter spatially resolved measurements: Review and biomedical applications”, *Optical Fiber Technology*, vol. 43, pp. 6–19, 2018.

[30] M. Froggatt and J. Moore, “High-spatial-resolution distributed strain measurement in optical fiber with Rayleigh scatter”, *Applied Optics*, vol. 37, no. 10, pp. 1735–1740, 1998.

[31] S. T. Kreger, A. K. Sang, D. K. Gifford, and M. E. Froggatt, “Distributed strain and temperature sensing in plastic optical fiber using Rayleigh scatter”, in *Fiber Optic Sensors and Applications VI*, International Society for Optics and Photonics, vol. 7316, 2009, 73160A.

[32] S. T. Kreger, D. K. Gifford, M. E. Froggatt, B. J. Soller, and M. S. Wolfe, “High resolution distributed strain or temperature measurements in single-and multimode fiber using swept-wavelength interferometry”, in *Optical Fiber Sensors*, Optica Publishing Group, 2006, ThE42.

[33] S. T. Kreger, N. A. A. Rahim, N. Garg, S. M. Klute, D. R. Metrey, N. Beaty, J. W. Jeans, and R. Gamber, “Optical frequency domain reflectometry: Principles and applications in fiber optic sensing”, in *Fiber Optic Sensors and Applications XIII*, International Society for Optics and Photonics, vol. 9852, 2016, 98520T.

[34] P. Lu, S. J. Mihailov, D. Coulas, H. Ding, and X. Bao, “Low-loss random fiber gratings made with an fs-IR laser for distributed fiber sensing”, *Journal of Lightwave Technology*, vol. 37, no. 18, pp. 4697–4702, 2019.

[35] T. Horiguchi, T. Kurashima, and M. Tateda, “Tensile strain dependence of Brillouin frequency shift in silica optical fibers”, *IEEE Photonics Technology Letters*, vol. 1, no. 5, pp. 107–108, 1989.

[36] J. Dakin, D. Pratt, G. Bibby, and J. Ross, “Distributed optical fibre Raman temperature sensor using a semiconductor light source and detector”, *Electronics letters*, vol. 13, no. 21, pp. 569–570, 1985.

[37] W. L. Ko, W. L. Richards, and V. T. Tran, “Displacement theories for in-flight deformed shape predictions of aerospace structures”, *NASA/Tp-2007-214612*, 2007.

[38] A. Beisenova, A. Issatayeva, I. Iordachita, W. Blanc, C. Molardi, and D. Tosi, "Distributed fiber optics 3D shape sensing by means of high scattering NP-doped fibers simultaneous spatial multiplexing", *Optics Express*, vol. 27, no. 16, pp. 22 074–22 087, 2019.

[39] S. Minakuchi, T. Nakamura, T. Nadabe, M. Nishikawa, N. Takeda, M. Kishi, and K. Hotate, "Damage detection of CFRP bolted joints using embedded optical fibers with BOCDA system", *Japan Society of Aeronautical Space Sciences*, vol. 59, no. 690, pp. 176–182, 2011.

[40] A. Güemes, A. Fernandez-Lopez, and P. Fernandez, "Damage detection in composite structures from fibre optic distributed strain measurements", in *EWSHM-7th European Workshop on Structural Health Monitoring*, 2014.

[41] H. Murayama, D. Wada, and H. Igawa, "Structural health monitoring by using fiber-optic distributed strain sensors with high spatial resolution", *Photonic Sensors*, vol. 3, no. 4, pp. 355–376, 2013.

[42] F. Parent, S. Loranger, K. K. Mandal, V. L. Iezzi, J. Lapointe, J. S. Boisvert, M. D. Baiad, S. Kadoury, and R. Kashyap, "Enhancement of accuracy in shape sensing of surgical needles using optical frequency domain reflectometry in optical fibers", *Biomedical Optics Express*, vol. 8, no. 4, pp. 2210–2221, 2017.

[43] S. Loranger, M. Gagné, V. Lambin-Iezzi, and R. Kashyap, "Rayleigh scatter based order of magnitude increase in distributed temperature and strain sensing by simple UV exposure of optical fibre", *Scientific Reports*, vol. 5, no. 1, pp. 1–7, 2015.

[44] A. Yan, S. Huang, S. Li, R. Chen, P. Ohodnicki, M. Buric, S. Lee, M. Li, and K. P. Chen, "Distributed optical fiber sensors with ultrafast laser enhanced Rayleigh backscattering profiles for real-time monitoring of solid oxide fuel cell operations", *Scientific Reports*, vol. 7, no. 1, pp. 1–9, 2017.

[45] P. Lu, S. J. Mihailov, D. Coulas, H. Ding, and X. Bao, "Random fiber gratings fabricated using Fs-IR laser for distributed temperature sensor application", in *26th International Conference on Optical Fiber Sensors*, OSA, 2018, FA2.

[46] P. Bulot, O. Cristini, M. Bouet, A. Demol, L. Bigot, G. Bouwmans, S. Plus, R. Habert, G. Laffont, and M. Douay, "OFDR distributed temperature sensing at 800 °C on a fiber with enhanced Rayleigh scattering profile by doping", in *Bragg Gratings, Photosensitivity and Poling in Glass Waveguides and Materials*, Optical Society of America, 2018, BM3A–2.

[47] P. Bulot, R. Bernard, M. Cieslikiewicz-Bouet, G. Laffont, and M. Douay, "Performance study of a Zirconia-doped fiber for distributed temperature sensing by OFDR at 800° C", *Sensors*, vol. 21, no. 11, p. 3788, 2021.

[48] C. Molardi, S. Korganbayev, W. Blanc, and D. Tosi, "Characterization of a nanoparticles-doped optical fiber by the use of optical backscatter reflectometry", in *Advanced Sensor Systems and Applications VIII*, International Society for Optics and Photonics, vol. 10821, 2018, p. 1 082 121.

[49] V. Fuertes, N. Grégoire, P. Labranche, S. Gagnon, R. Wang, Y. Ledemi, S. LaRochelle, and Y. Messaddeq, “Engineering nanoparticle features to tune Rayleigh scattering in nanoparticles-doped optical fibers”, *Scientific Reports*, vol. 11, no. 1, pp. 1–12, 2021.

3

MODELLING OF LIGHT SCATTERING BY GOLD NPS AT OPTICAL FIBRE INTERFACES

Doping gold nanoparticles was expected to achieve the goal of increasing the backscattered signal in the optical fibre dramatically, to increase the signal to noise ratio to achieve higher precision strain sensing in structural health monitoring. In some cases, this backscattered light enhancement can be minimal but in some cases, this enhancement can be huge. By manufacturing various types of nanoparticle(NP)-doped optical fibre, the relationship between the doping and the backscattering enhancement can be obtained. However, manufacturing NP-doped optical fibre is expensive and is not easy to implement. Especially, it is a great challenge in an optical laboratory. In order to preliminarily explore the characteristic of the backscattered light by the nanoparticles in the laboratory to find the cases of light enhancement by nanoparticles, a method of dropping liquid containing nanoparticles to the optical fibre end tips was proposed to evaluate the backscattered light level and to detect large backscattered light cases. In this chapter, an experimental setup used for detecting the backscattered light from the nanoparticles in liquid was built and a corresponding model was built to analyse the light scattering by gold nanoparticles at optical fibre interfaces.

Parts of this chapter have been published in Journal of Optics **23**, 3 (2021): 035602.

Optical fibre backscatter reflectometry is an important technique for Structural Health Monitoring (SHM). In recent years, increasing the intensity of backscattered light in backscatter reflectometry has shown the advantage of improving the signal detection in shape sensing and temperature detection due to the increase of signal to noise ratio and this approach can be used to improve the performance for SHM. Doping nanoparticles (NPs) is a method to increase the intensity of backscattered light in distributed fibre optic sensing. The increased intensity of light backscattered by the NPs needs to be investigated to design suitable optical sensing fibres with NPs for backscatter reflectometry. In this work NPs were added to refractive index matching liquid and tested with commercial NP suspensions experimentally between the tips of two optical fibres. An estimate of the intensity of backscattered light from NPs in this structure was performed by simulation to give a better understanding of the expected levels of intensities of scattered light from NPs in this distributed fibre optic sensing configuration. Analytical models based on Mie theory and the Monte Carlo Method are presented. Simulated results are presented, for a broad bandwidth Gaussian spectra shape incident light with a central wavelength around 1550 nm , to match the experimental conditions in this work. The novelty is in developing this model for scattered light by NPs at optical fibre interfaces and the evaluation of the possibility of detection by the calculated scattered intensity levels. This chapter is related to sub-research question 2: if nanometre to micrometre size particles are introduced into an optical fibre, what is the intensity characteristic of the scattered light in optical fibre with these particles?

3.1. INTRODUCTION

Backscatter reflectometry based on optical frequency domain reflectometry (OFDR) for strain or temperature sensing emerged two decades ago [1] and has developed into a technique with millimetre spatial resolution [2]–[4]. Due to its distributed sensing capability for strain, it has been widely used for Structural Health Monitoring (SHM) in aerospace [5]–[7] and civil engineering [8].

In recent years, some methods have been proposed to increase the sensing performance of backscatter reflectometry and these have been applied in many research fields. One approach is to introduce damage into the core of the optical fibre with a laser. Loranger et al. [9] proposed a simple way to increase the intensity of scattered light (by about 20 dB) in an optical fibre with Ultraviolet (UV) exposure (213 nm, 5th harmonic of a 1064 nm Nd:YAG Laser). The strain resolution and measurement quality improved after UV exposure. For a high NA photosensitive fibre under UV exposure showed low noise level (5 mK or 40 nϵ). Parent et al. [10] also used this method and realized a 47 % accuracy improvement in shape sensing in surgical needles. Yan et al. [11] used an ultrafast infrared(IR) laser (800 nm, Ti:Sapphire Laser) to make nanogratings to increase the intensity of scattered light in an optical fibre (by about 40-45 dB). The defects (nanogratings) are stable and can be used at a temperature of up to 800 °C. Lu et al. [12] improved the accuracy of temperature detection by fabricating random fibre gratings with a femtosecond IR laser (800 nm) in an optical fibre.

Doping NPs into the core of optical fibre is an another very important approach to increase the backscattered light and generally the backscattered light enhancement is higher than the method of introducing damage with a laser. For strain sensing, Blanc and Dussardier [13] described different methods of making NPs in silica optical fibre and analysed the obtained losses with Rayleigh scattering. Molardi et al. [14] investigated the characteristics of MgO doped optical fibre and obtained a 50 dB scatterred light increase experimentally. They pointed out that this doped fibre could be used for spatial multiplexing in optical backscatter reflectometry. Beisenova et al. [15] presented the experimental results of 3D shape sensing with a MgO doped optical fibre in a spatial multiplexing structure for an epidural needle. These results show the sensing improvement caused by doping NPs. As mentioned above, strain sensing is also important for SHM. Therefore, the phenomenon of light scattered by NPs in optical fibre drew my attention. I think that the improvement of signal to noise ratio in strain sensing by NPs may also show potential for Structural Health Monitoring based on strain detection and I paid attention to investigate on the behaviors of light scattered by NPs.

In practice, manufacturing optical fibres with NPs is not easy in an optical laboratory and a careful design is needed. In order to investigate the behaviours of NPs in fibre optic sensors, A simple setup was built to investigate the characteristics of NPs for further development in SHM [16]. It is to drop refractive index matching liquid between two optical fibre tips and to study the scattering characteristics for different NPs under different experimental parameters. By eliminating the influence of the reflections from the optical system, the detected backward signals caused by the scattering from NPs in refractive index matching liquid can be obtained. Then by constituting the relationship between scattered light signals from NPs and scattered light by NPs in the optical fibre, the goal of evaluating the scattered light by NPs in the optical fibre can be achieved. However, with this approach, the levels of scattered light need to be treated carefully because the intensity of scattered light from low concentration NPs are generally low and could likely be lower than the sensitivity of a conventional optical detection system. Therefore, a model of light scattering by gold NPs at optical fibre interfaces needs to be built and a simulation of the intensity of scattered light from NPs needs to be performed in advance to give a good understanding of these intensity levels of scattered light. The models for backscattered light will be shown in this chapter for three different sizes of NPs to determine suitable experimental conditions.

This chapter is organized in five sections. The first section is the Introduction. The model for the simulation is given in Section 3.2. The intensities of scattered light with the coupling model are simulated from 10 nm to 400 nm size gold NPs with the Monte Carlo method and experiment with commercial 10 nm, 100 nm and 400 nm for different concentrations are compared with the calculated results in Section 3.3. This is followed by a discussion in Section 3.4. Section 3.5 is the Conclusions.

3.2. EXPERIMENT SETUP AND MODEL

In this section, the experimental setup used for modelling is introduced first in Section 3.2.1. The model of light propagation at optical fibre end tips is then described in Section 3.2.2. The model of scattered light by NPs and the light recoupled into the upper optical fibre will be described in Section 3.2.3.

3.2.1. EXPERIMENTAL SETUP

The experimental setup used is shown below in Figure 3.1 to collect back-scattered light from NPs suspended in liquid between the two optical fibre tips to show the intensity improvement by NPs. Figure 3.1 (a) shows a diagram of the experimental setup. It includes a 1550 nm central wavelength superluminescentdiode (FESL-1550-20-BTF, Frankfurt Laser Company), an optical circulator (6015-3-APC Fibre Optic Circulator, Thorlabs), a 3-axis translation stage (MAX373D/M, Thorlabs), two photo-detectors (Photodetector 1: PM20C (Thorlabs), Photodetector 2: PDB420C Monitor+, Thorlabs), an analog-to-digital (A/D) converter (PicoScope 6402A, Pico Technology), a computer and a USB microscope.

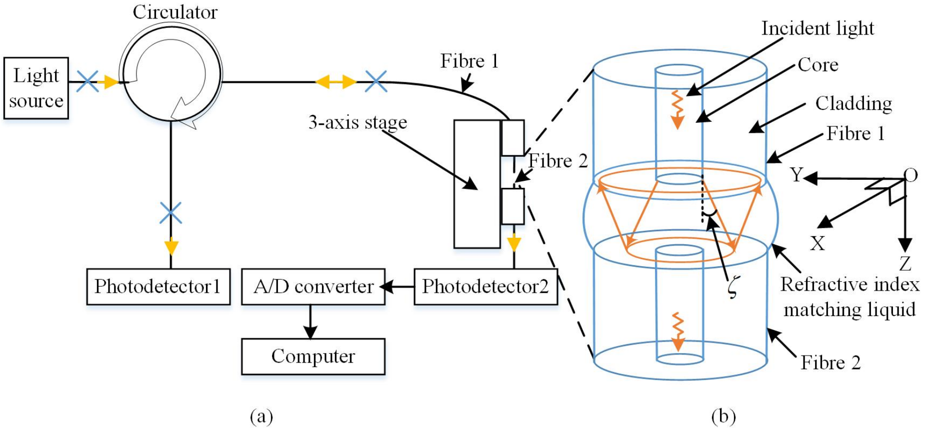

Figure 3.1: Experimental setup. (a) Diagram of the experimental setup. The yellow arrows represent the directions of light propagation. The blue crosses are the optical fibre connectors. (b) Enlarged figure of the region of the two optical fibre end tips. The optical fibre is shown in blue. Light is in yellow with its propagating directions. ζ is the divergence angle in liquid. A coordinate system is defined with the origin(O) at the centre of the end surface of the upper fibre.

Light emitted from the light source goes via the circulator to the upper optical fibre (Fibre 1: single mode fibre 1550BHP, Thorlabs) on the 3-axis stage. The end tip of Fibre 1 is fixed and Fibre 2 is clamped onto this 3-axis stage. Liquid containing NPs is dropped into the gap between the end tips of the lower optical fibre (Fibre 2: single mode fibre 1550BHP, Thorlabs) by a volumetric dispenser (PreciFluid). For the modelling, refractive index matching liquid (refractive index 1.4520) containing an homogeneous suspension of gold NPs is used to dropped between two optical fibre end tips. With the use of refractive index matiching liquid, the influence from the reflection from optical fibre end tips are reduced in order to foucs on the signal scattered by NPs. For the experiment, commercial gold NPs suspensions in citrate buffer (Sigma-Aldrich) are used for test. The end tips shown in Figure 3.1 (b) are cleaved at 90° in modelling (Note: angle polished connectors are used as end tips for the experiment to further reduce the reflection from optical fibre end tips). Figure

3.1 (b) shows more details of this fibre end tips gap for modelling. Some of light is coupled into the lower optical fibre through the refractive index matching liquid containing gold NPs and detected by photo-detector 2. Optical fibres are shown in blue in Figure 3.1 (b). Light collected by photo-detector 2 is used for detecting the extinction from the gold NPs, but in this chapter only backscattered light from NPs was analysed. Some of the light is scattered or reflected back to the upper optical fibre and the light is collected by photo-detector 1 via the circulator. If the refractive index of the refractive matching liquid matches the refractive index (RI) of the optical fibres, the reflected light from the end tips of the gap will be eliminated and the percentage of scattered light from NPs to the total obtained light at photo-detector 1 will improve. Note: even though refractive index liquid is used, there remain reflections from the surfaces of the optical fibre end tips and the collected light by photo-detector1 is a combination of both the light scattered by NPs and the reflection of the end tips.

3.2.2. LIGHT PROPAGATION BETWEEN TWO OPTICAL FIBRE END TIPS

In order to model the experimental setup more accurately, the spectrum of the light source is modelled with a Gaussian spectrum. There is a good similarity of the spectrum from the superluminescent diode (FESL-1550-20-BTF, Frankfurt Laser Company) and the Gaussian spectrum ($R^2 = 0.97$). Therefore, the spectrum of the incident light is modelled as a Gaussian spectra shape light according to the shape of the superluminescentdiode and the total power is normalized to I_0 as

$$I(\lambda) = I_0 \times \left(\frac{2\sqrt{\ln 2}}{\Delta\lambda_{FWHM}\sqrt{\pi}} \times \exp\left(-4\ln 2 \left(\frac{\lambda - \lambda_c}{\Delta\lambda_{FWHM}} \right)^2 \right) \right), \tag{3.1}$$

where, I_0 is the power of the incident light. λ is the wavelength of the light; $\Delta\lambda_{FWHM}$ is the full width at half maximum (FWHM) of the spectra. $\Delta\lambda_c$ is the central wavelength. λ, $\Delta\lambda_{FWHM}$ and $\Delta\lambda_c$ are in nm.

For the light power density distribution at the end of the upper optical fibre, a Gaussian distribution of light is used for this single-mode optical fibre and the power density distribution is expressed as

$$I_{in optical fibre}(r, \lambda) = \frac{I(\lambda)}{(2\sigma_0)^2\pi/2} \times \exp\left(-2 \left(\frac{r}{2\sigma_0} \right)^2 \right), \tag{3.2}$$

where, r is the radial distance to the centre of the cylindrical optical fibre and $r = \sqrt{x^2 + y^2}$. (x, y) is the position. $2\sigma_0$ represents the mode field radius of the incident light in the upper optical fibre.

In the liquid, the transmitted light will disperse in the refractive index matching liquid. The divergence angle ζ for a single mode fibre is small and can be calculated from its numerical aperture (NA) and the RI of the refractive index matching liquid. The side reflection caused by the external boundary of the RI liquid is negligible. The shape of the light propagating in the liquid can be estimated by the geometric divergence

$$\begin{aligned} I_{wavelength}(x,y,z,\lambda) = {} & T_1 \times \exp(-\alpha z) \times I(\lambda) \\ & \times \frac{1}{(2\sigma_0/k(z))^2 \pi/2} \times \exp\left(-2\left(\frac{r}{2\sigma_0/k(z)}\right)^2\right), \end{aligned}$$

$$k(z) = \frac{r_{core}/\tan\zeta}{z + r_{core}/\tan\zeta}, \tag{3.3}$$

where, T_1 is the transmittance between the optical fibre to liquid surface and can be calculated using the Fresnel Equation, α is the light loss coefficient in the liquid and can be expressed by the sum of the loss by absorption by the liquid and the extinction by NPs in the liquid; and $k(z)$ is the distribution amplification ratio at this position. The propagating wave is to be a plane wave in Equation 3.3 because of the small divergence angle (about 5°), so the the distribution amplification ratio is only related to the Z direction. Using the RI at a central wavelength of 1550 nm for the calculation, the divergence angle ζ can be regarded as a constant for different wavelengths for calculation. ζ can be deduced by the relation $NA = n_{liquid}\sin\zeta$.

The light propagating between the two optical fibre end tips will be reflected by the two end surface, but the reflected light is negligible as analysed below. As shown in Figure 3.1 (b), part of the light will be reflected at the surface of the lower optical fibre and then propagate until reaching the surface of the upper optical fibre. The reflected light can also be expressed by Equation 3.3 because the lower optical fibre has the same geometry as the upper optical fibre.

The expression of the reflected light can be expressed as

$$I_{wavelength,backward}(r,z',\lambda) = \frac{T_1 R_2 I(\lambda)}{(2\sigma_0/k(z'))^2 \pi/2} \exp\left(-2\left(\frac{r}{2\sigma_0/k(z')}\right)^2 - \alpha z'\right), \tag{3.4}$$

where, R_2 is the reflectance at the lower optical fibre interface and can be calculated according to the Fresnel Equation; α is the attenuation caused by the absorption of liquid and extinction from NPs; $z' = 2h - z$.

Reflected light will propagate until the interface of the upper fibre. Considering that only light incident on the core of optical fibre can be re-coupled, the intensity of reflected light coupled into the upper optical fibre can be expressed as the integral

$$I_{reflect} = \int_{S_{core}} \int_{\lambda} T_1 I_{wavelength,backward}(x,y,2h,\lambda)\,\mathrm{d}\lambda\,\mathrm{d}S_{core}, \tag{3.5}$$

where, S_{core} is the region of the core of optical fibre.

The back-propagating light will also be reflected at the surface of the upper optical fibre. It is not shown in Figure 3.1 (b) and has not been taken into consideration in analyses. The reason for this is that when the refractive index matching liquid is used the reflectance is very low at the interfaces (e.g. only about 4.750×10^{-7} with the RI of the optical fibre of 1.450 and the RI of the liquid at 1.452) and when the light reflects twice the intensity of the light will be lower than the square of this reflectance. Light reflected multiple times also is neglected. Now it is known that transmitted light is the main factor affecting scattering by NPs as compared to reflected light. In the next part, the scattered light by NPs and the scattered light re-coupling into the upper optical fibre will be discussed.

3.2.3. SCATTERED LIGHT COUPLING MODEL

The concentrations of the NPs in the liquid are low and meet the requirement for single scattering [17] (Hartel's theory: optical depth $\tau = NC_{ext}z < 1$) in this model. N is concentration, C_{ext} is the extinction cross-section and z is the path depth. In this case, only the light scattered once by the NPs is taken into account. The intensity of scattered light by single particles can be added because the random positions of the NPs in liquid and the movement of the NPs cause decoherence. The concentration of NPs in a unit volumetric liquid is assumed to be a constant. Due to the low conentration of the NPs, it is assumed that the wave front will not be disturbed by the NPs but it will attenuate from the absorption of the medium and the extinction by NPs. Figure 3.2 shows the modelled configuration with NPs. The blue dots in Figure 3.2 represent NPs in random position in the RI liquid volume. The sizes of all the NPs is assumed to be the same and they are assumed to be spheres.

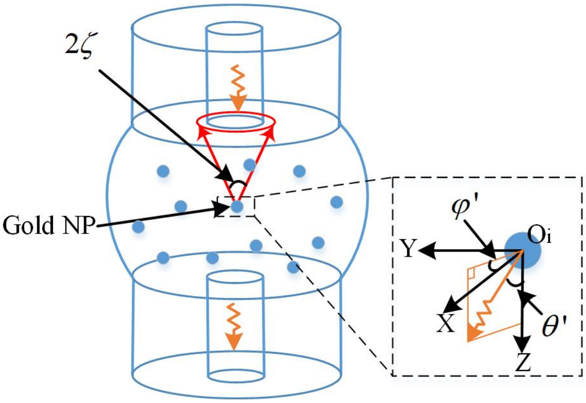

Figure 3.2: Model of re-coupled scattered light from NPs (a) The enlarged picture of the region of the upper optical fibre surface shows the overlap area by the edge of scattered light on the upper fibre end tip (red) the core of optical fibre (blue); (b) the enlarged picture of a NP with its spherical coordinates whose Origin is at the centre of this NP.

Considering the size of the NPs, the incident light can be considered as the plane wave incident on each NP. Therefore its scattered light by the NPs can be calculated by Mie theory [18]. According to Mie theory, the intensity of light scattered by a spherical particle verses angle θ' can be expressed as

$$I_s(\theta', \varphi', r', \lambda) = \frac{(\lambda/n_{liquid})^2}{4\pi^2 r'^2}\left(\frac{i_1(\theta') + i_2(\theta')}{2}\right). \tag{3.6}$$

It is described in a spherical coordinate system as shown in the enlarged picture of Figure 3.2. The Origins are set at the centres of NPs (O_i). θ' is the scattering angle,

r' is the distance between the center of the spherical gold NP to the detection point, $i_1(\theta')$ and $i_2(\theta')$ are called the scattering intensity functions, the unit of λ is µm and the unit of r' is µm. The parameters $i_1(\theta')$ and $i_2(\theta')$ can be obtained by Mie theory [18].

The scattered wave is regarded as a spherical wave whose centre is at the centre of the NP. A red cone shows the numerical aperture (NA) of the optical fibre in Figure 3.2. It is the part of the spherical wave scattered by the NP which is within in the acceptance angle of the optical fibre. The intersection of the red cone with the surface of the upper optical fibre is a red circle as shown in Figure 3.2. The blue circle in Figure 3.2 is the core of optical fibre. There is an overlap area between the two circles. The overlap area is regarded as the area in which the light can be re-coupled into optical fibre. When integrating the light propagating into this overlap area, the intensity of re-coupled light scattered by one NP can be obtained.

However, the integral of all the light within the angles in the overlap area is complicated when the NPs are not at the centre of the propagating light. To simplify the calculation, the mean value of the intensity density of the scattered light in the backward direction (π) is used and in the edge of the red cone ($\pi - \zeta$) as the mean value for intensity density in this overlap area. The mean value for intensity in this overlap area can be expressed as

$$I_{mean} \approx \frac{I_s(\pi, \varphi', r', \lambda) + I_s(\pi - \zeta, \varphi', r', \lambda)}{2}. \tag{3.7}$$

Therefore, the intensity of the scattered light in the cone is estimated as I_{mean}. The mean value for intensity density in this overlap area times the area of the spherical cap is regarded as the intensity of the scattered light within the cone.

Considering the divergence angle is small, the area of the cross-section of the spherical cap on the surface of the upper optical fibre is estimated to be the area of the spherical cap. Therefore, the intensity of scattered light within the cone can be estimated by the mean-value for intensity density in this overlap area times the area of the projection of the spherical cap on the surface of the upper optical fibre.

Because the mean value of scattering is used, the calculation speed can be accelerated by considering the ratio of the scattered light incidents on the core of the upper optical fibre end tip. The overlap ratio is defined as the percentage of the overlap area of the core of optical fibre to the area of the spheres whose centres are at the centre of the NPs cut by the end tip of the optical fibre. It is the coupling efficiency of light scattered by NPs coupled to upper side optical fibre end tip in this paper. The overlap ratio γ can be expressed as

$$\gamma = S_{overlap}/S_{cone}, \tag{3.8}$$

where, $S_{overlap}$ is the area of the overlap area; S_{cone} is the area of the cross-section of the spherical cap on the surface of the upper optical fibre.

Therefore, the intensity of re-coupled scattered light by one NP at the wavelength λ can be estimated by

$$\begin{aligned} I_s'(\lambda) &= \gamma \int_{\pi-\zeta}^{\pi} \mathrm{d}\theta' \int_0^{2\pi} I_{mean} r'^2 \sin\theta' \,\mathrm{d}\varphi' \\ &= \frac{(\lambda/n_{liquid})^2(1-\cos\zeta)\gamma}{4\pi} \left(\frac{i_1(\pi)+i_2(\pi)}{2} + \frac{i_1(\pi-\zeta)+i_2(\pi-\zeta)}{2} \right). \end{aligned}$$

Then, the total scattered light that meets this requirement and can be recoupled into the upper optical fibre can be expressed as

$$I_{recouple} = \int_V cT_1 \left(\int_\lambda I_{wavelength}(x,y,z,\lambda) I_s'(\lambda) \exp(-\alpha z)\,\mathrm{d}\lambda \right) \mathrm{d}V, \tag{3.9}$$

where, V is the volume of integral volume, c is the concentration of NPs. Equation 3.9 mainly includes the light transmission(T_1 and $I_{wavelength}$), the scattering by the NPs and recoupling into optical fibre (c, I_s') as well as the light attenuation ($\exp(-\alpha z)$) when the light propagates back.

3.3. SIMULATED AND EXPERIMENTAL RESULTS

3.3.1. SIMULATIONS WITH THE MONTE CARLO METHOD

The Monte Carlo Method [19], [20] is used to estimate the scattered intensity from NPs. $N(1000)$ points (x,y,z,λ) were chosen for each spatial resolution for 6 times. (x,y,z) were randomly distributed in the integral cuboids and λ were randomly chosen from the range $\lambda_{min} = 1480\,\mathrm{nm}$ to $\lambda_{max} = 1620\,\mathrm{nm}$ (In this wavelength range the power of the light accounts for about 99.4 % of the I_0).

According to the Monte Carlo Method, the approximation of Equation 3.9 can be expressed as

$$I_{recouple} = \sum_{n=1}^{N} \frac{1}{N} cT_1 I_{wavelength}(x,y,z,\lambda) I_s'(\lambda) \frac{1}{1/V_c(\lambda_{max}-\lambda_{min})}. \tag{3.10}$$

10 µm was chosen as the axial resolution Δz in order to show the re-coupled scattered light distribution in the Z direction. The distance between the two optical fibre tips was set to 1 mm. In each axial resolution region all of the scattered light which can be re-coupled into the optical fibre were integrated, so that the integral Z distance is 10 µm. In the X and Y directions the integral range was restricted in cuboids, whose height was the axial resolution, length and width were $3\sigma(z)$ at the centre of each spatial intervals (z_{mean}). Only the NPs in these cuboids $V_c(V_c = (3\sigma(z_{mean}))^2\Delta z)$ were taken into account as shown in Figure 3.3.

The diameters of spherical gold NPs were chosen from 10 nm to 400 nm. The step in size change was set at 30 nm and the concentrations were set of $1\times10^8\,\mathrm{mL}^{-1}$ so that the concentrations were low for all different size of gold NPs. For the 400 nm size gold NPs, the volume ratio was only about 3.35×10^{-6}.

The refractive index of gold used is from Johnson and Christy [21]. The original data of the RI of gold is shown with error bars in Figure 3.4.

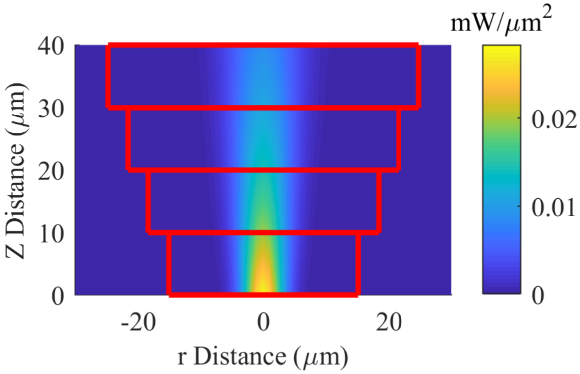

Figure 3.3: The integrated regions along the propagating of light (The red rectangles represent the integral cuboids with axial resolution 10 µm, length and width of $3\sigma(z)$ at the centre of each spatial intervals (z_{mean})).

The RI of gold is a function of the incident light wavelength. Based on the data trends, a third order polynomial fitting curve was used for the real part of the gold RI while for the imaginary part of the gold RI a linear fitting curve was used. The fitting was made by the software Origin 2019 (OriginLab Corporation) and the fitting region is from 1088 nm to 1937 nm. The obtained expressions for the real and imaginary parts of the gold RI are:

$$n_{Au} = -2.72440 + 0.00607 \times \lambda - 4.18591 \times 10^{-6} \times \lambda^2 + 1.04432 \times 10^{-9} \times \lambda^3, \tag{3.11}$$

$$k_{Au} = -1.35038 + 0.00781 \times \lambda, \tag{3.12}$$

where, the unit of wavelength of the incident light is nm. Other parameters used for calculations are listed in Table 3.1.

Because the concentration is low, the extinction from NPs was neglected. Therefore, $\alpha = 0$ in calculation. The calculation of scattering intensity functions utilize the MatLab code from Matzler's paper [25].

The simulations were processed in Matlab R2019a (The MathWorks). Figure 3.5 shows the results.

It can be seen from Figure 3.5 (a) that the accumulated power increases slowly as the Z distance increases. When the size of NPs increases at the same Z distance the power increases quickly. When the Z distance is above 500 µm and the diameters of NPs are above 250 nm, the accumulated power is above 1 nW. The scattered power decreases dramatically when the size of the NPs is below 50 nm. At a size of about 50 nm, the scattered light is only 0.1 pW. Below a size of about 40 nm, the scattered light is below 0.01 pW. Figure 3.5 (b) is the corresponding error to Figure 3.5 (a). The

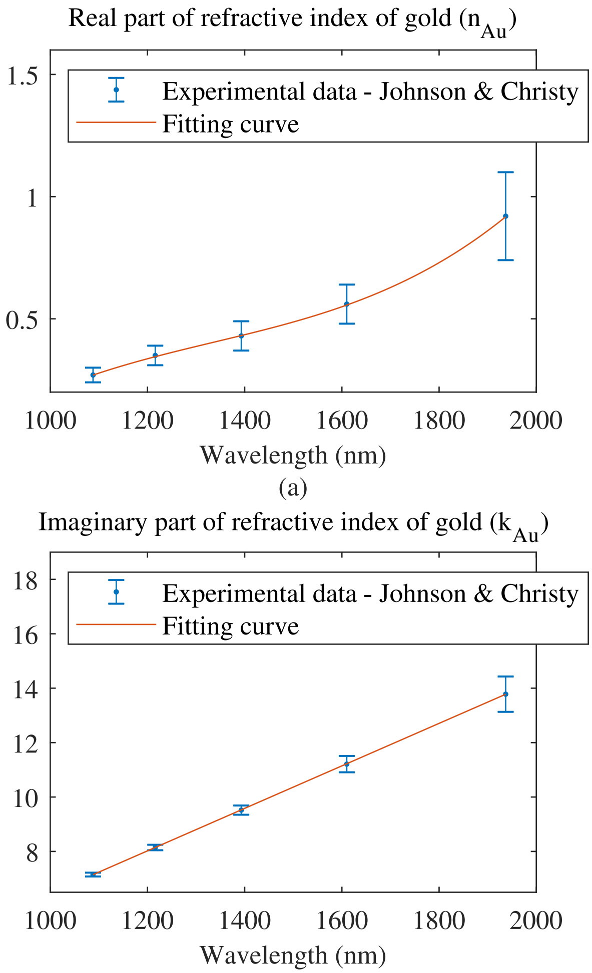

(a)

(b)

Figure 3.4: The refractive index of gold (Au) and its fitting plot. (a) The real part (*n*) of refractive index of gold verse wavelength; (b) The imaginary part (*k*) of refractive index of gold verses wavelength. [21]

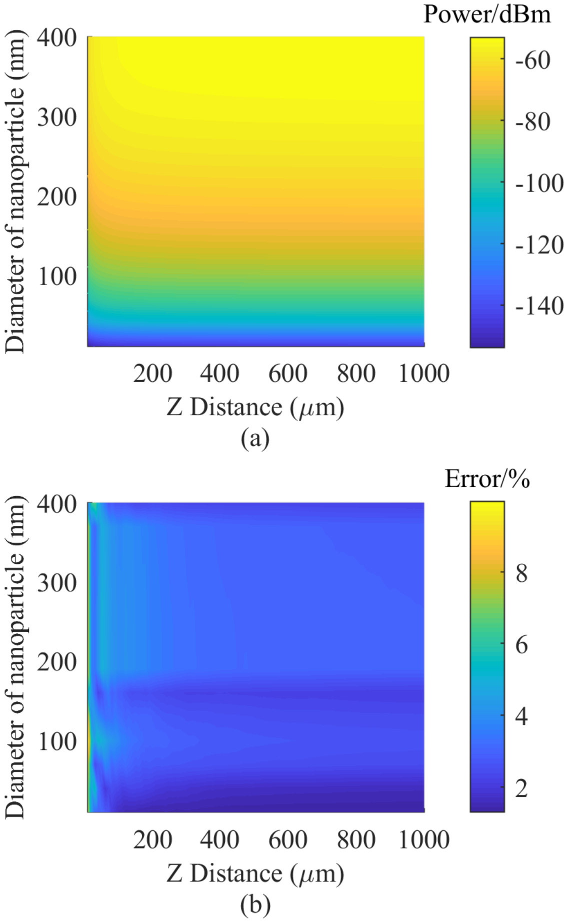

Figure 3.5: Accumulated scattered light by NPs along the Z direction (The input power is 1 mW and the concentrations of gold NPs are $1 \times 10^8\,\mathrm{mL}^{-1}$). (a) The scattered light power along the Z direction versus different size of NPs (0 dBm = 1 mW); (b) the errors of the results for the calculated accumulated scattered light power.

Table 3.1: The parameters used for the calculation in this work.

Parameter	Symbol	Value for calculation
Central wavelength	I_c	1550 nm [22]
Light source bandwidth	$\Delta\lambda_{FWHM}$	60 nm [22]
Incident light power	I_0	1 mW
Core radius of 1550BHP	r_{core}	4.5 µm [23]
RI of 1550BHP	n_{fibre}	1.4511 [23]
NA of 1550BHP	NA	0.13 [23]
Mode field radius	$2\sigma_0$	4.75 µm [23]
RI of RI matching liquid	n_{liquid}	1.4520 (near Series A, Cargille [24])
Concentration of gold NPs	c	1×10^8 mL^{-1}

Table 3.2: The parameters of experiment samples.

Sample	Concentration [26]	Gold volume ratio
Gold NP 10 nm	5.38×10^{12} - 6.58×10^{12} mL^{-1}	3.131×10^{-4} %
Gold NP 100 nm	3.45×10^{9} - 4.22×10^{9} mL^{-1}	2.008×10^{-4} %
Gold NP 400 nm	1.60×10^{8} - 2.10×10^{8} mL^{-1}	6.199×10^{-4} %

errors are below 10 %. Most of the errors are created at the region near the origin of Z direction.

3.3.2. CASE STUDY WITH EXPERIMENTS

Three different sizes of gold NPs (10 nm, 100 nm and 400 nm) were evaluated by the Monte Carlo calculation and experiment tests. The parameters of these NPs are listed in Table 3.2.

The axial resolution used in Monte Carlo calculation was set of 12 µm which is similar to the axial resolution of an optical coherence tomography (OCT) system when this light source is used [22] and N was set of 10000 (calculation time is about 1h with the processor Intel Xeon W-2123 CPU) in each axial resolution region. It was assumed that the gold NPs had been successfully transferred to refractive index matching liquid (RI is 1.4520) and the concentrations used were the mean values of the concentrations given in Table 3.2. Figure 3.6 shows the results with relative dispersion errors. The relative dispersion error is defined as

$$E_{dispersion} = \left| \frac{s}{\bar{x}} \right| \times 100\,\% \tag{3.13}$$

to give the dispersion of the results, s is the sample standard deviation, $\bar{x}$ is the mean value of the samples. Figures 3.6 (a) to 3.6 (c)'s embedded graphs show the corresponding relative dispersion of Figure 3.6 (a) to 3.6 (c) respectively and it can be seen that the results have a low dispersion (below 8 %). The error bars in Figure 3.6 (a) to 3.6 (c) also show the relative dispersion errors.

From this calculation, the light reflection from the upper fibre interface can be calculated as 96.1 pW if the incident light is 1 mW (about −70 dB relative to incident

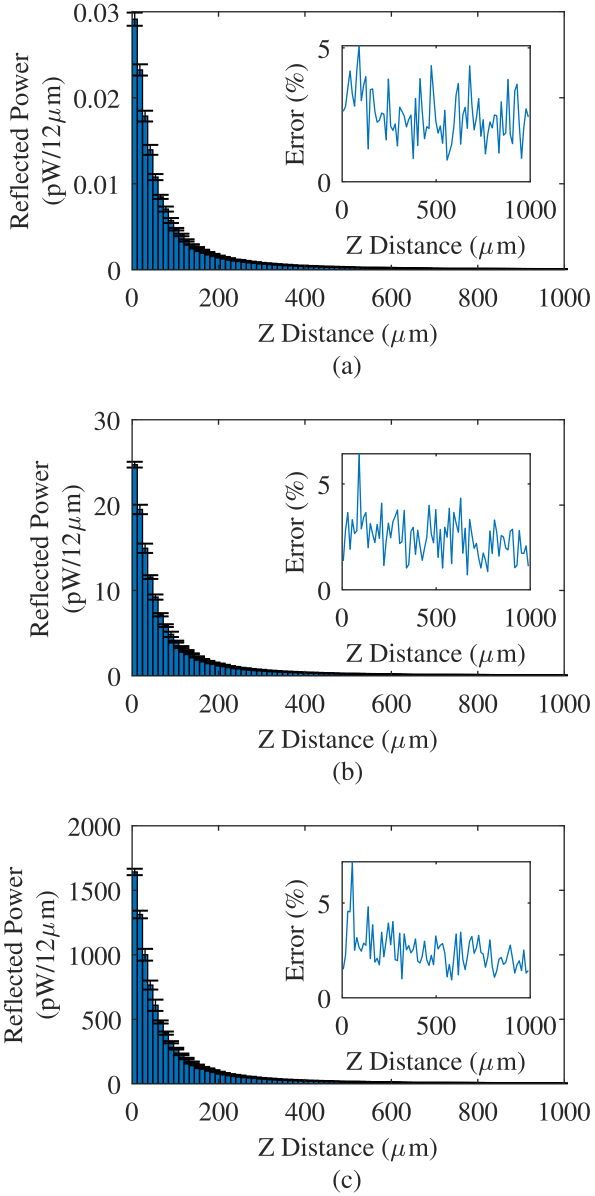

(a)

(b)

(c)

Figure 3.6: Estimated reflected power values with Monte Carlo Method with axial resolution 12 µm. (a) 10 nm diameter NPs under concentration 5.980×10^{12} mL^{-1}; (b) 100 nm diameter NPs under concentration 3.835×10^{9} mL^{-1}; (c) 400 nm diameter NPs under concentration 1.850×10^{8} mL^{-1}.

light power). Light reflected from the lower optical fibre interface and re-coupled into the upper fibre is 0.104 pW (about −100 dB). It can be seen from Figure 3.6 (a) that the scattered light from gold NPs in refractive index liquid decreases along the Z direction from about 0.03 pW. Note this is much smaller than the light reflection from the optical fibre end tip (96.1 pW). This signal is so weak that it would be a challenge to detect it with direct detection with the detection system shown in Figure 3.1. In Figure 3.6 (b), it can be seen that the scattered signal increases a lot when the NPs' size increases 10 times from 10 nm to 100 nm even if the concentration decreases by 156 times (see Table 3.2). The maximum value is also near the upper optical fibre end tip and the signal decreases from about 25 pW, which is also a week signal for direct detection. When the size of the NPs increases 4 times from 100 nm to 400 nm, even if the concentration decreases about 20 times, the scattered light increases. From Figure 3.6 (c), it can be seen that the scattered light decreases along the Z direction from about 1.4 nW. This would be an observable signal within the detection range of the PM20C photodetector and compared with the reflections from the upper optical fibre it is also a relatively high signal.

However, it is not easy to transfer gold NPs to refractive index liquid. In my former work [16], I tried to transfer commercial gold NPs suspension in citrate buffer (Sigma Aldrich) to refractive index liquid (Cargille). The experimental results showed that the transferring process is not efficient enough. Therefore, in this work I dropped the commercial gold NPs suspension directly onto the optical fibre end tips to obtain the scattered light intensity.

Due to the mismatching of refractive indices, there are relatively high reflections from the end tips of optical fibres. If the refractive index of commercial gold NPs suspensions is considered as 1.33, which is the same as the refractive index of water, the calculated reflected light from the upper optical fibre end tip is about 1.9 µW which is much higher than the scattered light by NPs. In order to increase the percentage of the scattered light and to decrease the reflection, a setup was designed to reduce the reflections from end tips with angle polished connectors as shown in Figure 3.7 (The upper optical fibre end tip is connected to the optical circulator; the lower connector has been fixed with epoxy to prevent its position changing). The two connectors are fixed with special designed aluminum clamps on the 3-axis stage. A volumetric dispenser (PreciFluid) was used to drop liquid to the optical fibre end tips' gap. A USB microscope was used to view the liquid drops.

By rotating the lower connector, a relatively low reflection was obtained. Then, 400 nm gold NP suspension, 100 nm gold NP suspension, 10 nm gold NP suspension and buffer liquid were dropped seperately. The buffer liquid was generated by collecting the liquid supernatant from the 400 nm gold NP suspension in a centrifuge (Centrifuge 5702, Eppendorf) in 5 min and 4300 rpm. Before each dropping process, the surfaces of the optical fibre tips were cleaned carefully with disposable wipes (Kimtech) using Acetone.

In order to increase the signal obtained at PM20C, the input light at the upper optical fibre end tip was increased to 3.00 mW. The experimental results are shown in Figure 3.8. The red bars in Figure 3.8 (a) show the situations when no liquid was dropped at the optical fibre end tips. The mean value is about 5.99 nW and

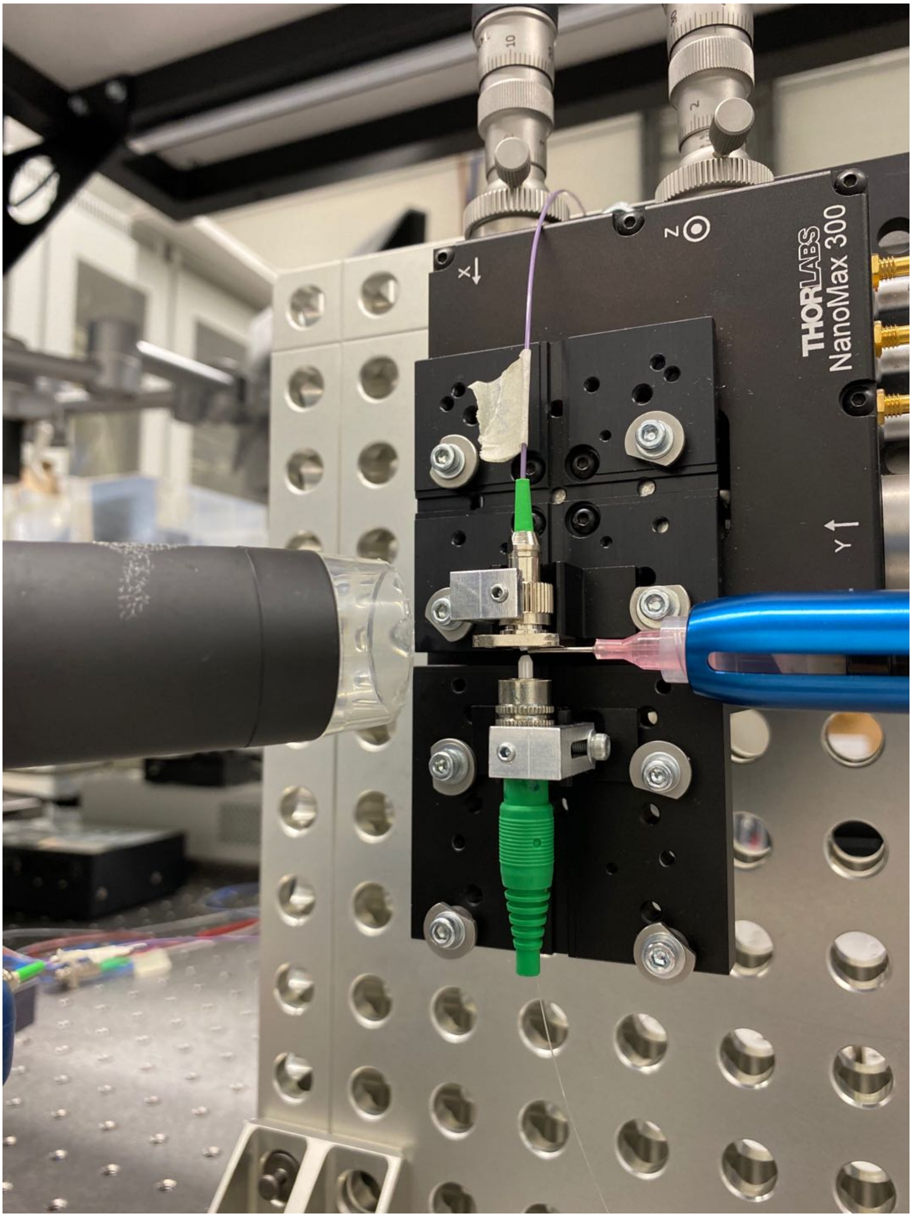

Figure 3.7: Photo of the designed setup. The upper optical fibre and the lower optical fibre are assembled in angle polished connectors(green) respectively clamped on the 3-axis stage with special designed clamps. The syringe in the volumetric dispenser used to drop liquid with a USB microscope to obtain the view for dropping liquid.

the standard deviation is about 1.40 nW. The blue bars in Figure 3.8 (a) show the results of dropping the 400 nm gold NP suspension into the gap. It shows a large distribution from about 4.38 nW to about 20.89 nW. The mean value is about 6.49 nW. The blue bars in Figure 3.8 (b) show the results of dropping the buffer liquid into the gap. The mean value is about 2.31 nW and the standard deviations is about 0.30 nW. The red bars in Figure 3.8 (b) show the results of dropping the 100 nm gold NP suspension into the gap. The mean value of it is about 2.21 nW. The yellow bars in Figure 3.8 (b) show the results of dropping the 10 nm gold NP suspension into the gap. The mean value is about 2.19 nW.

Figure 3.9 shows the calculated results compared with experimental results. The calculated results are based on the data in Table 3.2 and the RI of water used was 1.33 and RI of refractive index matching liquid used is 1.4520. The input power at the upper optical fibre is 3 mW. The axial resolution used in Monte Carlo calculation was set at 12 µm, N was set at 1000 in each axial resolution region.

Figure 3.9 (a) shows the reflected power for the three different cases in water. In order to show these results in the same figure. The results for 10 nm and 100 nm size gold NPs have been multiplied by suitable factors. The yellow line shows the results of scattered light 10 nm gold NPs and it is about 0.4 pW at Z distance 5.49 mm. The red line shows the results of scattered light 100 nm gold NPs and it is about 300 pW at Z distance 5.49 mm. The blue line shows the results of scattered light 400 nm gold NPs and it is about 34.7 nW at Z distance 5.49 mm. The black circle with error bar shows the error region of the calculated values due to the concentration distribution of 400 nm gold NP suspension. The blue circle represents the mean value of the scattered light from 400 nm gold NP which has been subtracted from the other reflections by the data of obtained reflected power with buffer liquid and has also been modified by taking the light loss due to the optical circulator. The error bars of the blue circle shows the position error range and the detected values range. The mean values of the 100 nm gold NPs and 10 nm gold NPs cases are almost 0 and are not shown in Figure 3.9 (a).

Figure 3.9 (b) shows the reflected power within each axial resolution. The solid lines show the results of scattered light by NPs in water and the dotted lines shows the cases in refractive index matching liquid (RI is 1.4520). The values in a different liquid is similar. For 10 nm gold NPs, the scattered light decreases along the Z direction from about −105 dB to about −130 dB. For 100 nm gold NPs, the scattered light decreases from about −75 dB to about −100 dB. For 400 nm gold NPs, the scattered light decreases from about −55 dB to about −85 dB.

3.4. DISCUSSION

From the simulation results in Figure 3.5, when the sizes of the gold NPs decrease from 400 nm to 10 nm the accumulated scattered power at the same Z distance decreases dramatically. It shows that the larger size gold NPs scattered much more light than the smaller particles (especially for NPs smaller than 50 nm). The accumulated scattered power increases but the increase rate becomes slow because more scattered light is accumulated when the Z distance is larger and when the Z distances increase the light divergence in space will cause lower power density in-

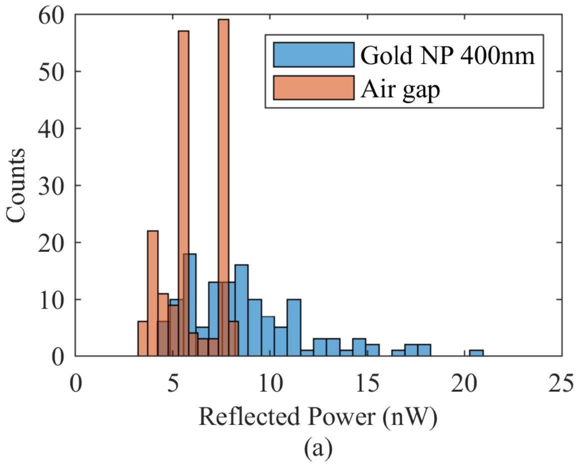

(a)

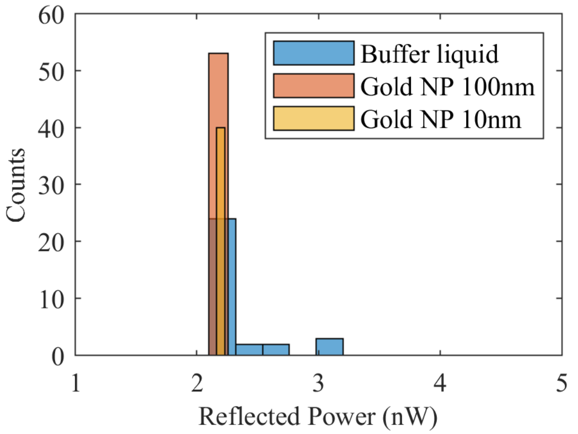

(b)

Figure 3.8: Experiment results of obtained reflected signals. (a) Comparison of air gap (without dropping liquid) and 400 nm gold NP suspension; (b) comparison of buffer liquid, 100 nm gold NP suspension and 10 nm gold NP suspension.

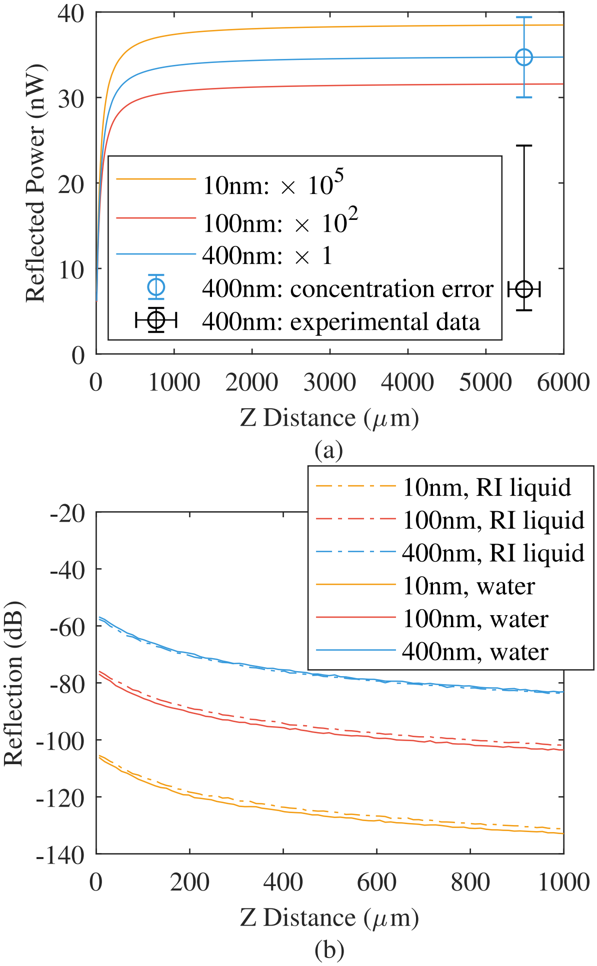

Figure 3.9: Estimated reflection values along the Z direction with resolution 12 µm compared with experimental results. The concentration of 10 nm diameter gold NPs is 5.980×10^{12} mL^{-1}; the concentration of 100 nm diameter gold NPs is 3.835×10^{9} mL^{-1}; the concentration of 400 nm diameter gold NPs is 1.850×10^{8} mL^{-1}. The incident power at the upper optical fibre is 3 mW. (a) The accumulated results along the Z direction for gold NPs in water; (b) the calculated results for gold NPs in water and refractive index matching liquid (RI=1.4520) with resolution 12 µm.

cident on the NPs so that there is less scattered light by each NP and the coupling efficiency will decrease when the Z distance increases. It is also shown in Figure 3.6 that most of the scattered light received by the upper optical fibre occurs at the region near the upper optical fibre end tip.

The experimental results in Figure 3.8 show the larger dispersion for the case of the 400 nm gold NP suspension than the case of the 100 nm gold NP suspension and the case of the 10 nm gold NP suspension. It implies a larger spatial distribution nonuniformty for larger size gold NPs.

The calculated accumulated reflected power in Figure 3.9 (a) shows that at Z distance 5.49 mm the accumulated reflected power from the case of 10 nm gold NPs is about 0.4 pW. For 100 nm gold NPs, it is about 300 pW. Both of them can not be detected by photodetector PM20C which has a detection limit of −65 dBm [27]. For the 400 nm gold NPs, it is about 34.71 nW. The blue circle with the error bar shows the predicted values from the model when the concentration error is considered. However, the experimental data in black circle with error bars is below the expected value. The maximum experimental data is about 31.6 % lower than the expected value. This loss is maybe caused by a lower concentration of gold NPs in the syringe because of the deposition of large size gold NPs and clusters of these gold NPs. In addition, it maybe also caused by the absorption by water which was reglected in the calculations. When the absorption by water is considered ($\alpha = 2.6\,\mathrm{mm}^{-1}$ [28]), the expected reflected value is 24.76 nW and it slightly above the experimental data range (from 5.11 nW to 24.37 nW).

For the cases of 10 nm gold NPs and 100 nm gold NPs as shown in Figure 3.9 (b), higher sensitivity detection methods need to be used. For example, a single photon detector or interferometers can be used. Generally, OCT has the advantage of high sensitivity of detecting low signals. The sensitivities of some OCT systems can reach above 100 dB sensitivity [29]–[31]. This high sensitivity is enough for the detection for the signals of the 100 nm gold NPs in Figure 3.9 (b), but for the case of 10 nm gold NPs it is still a challenge. Therefore, the challenge of the detection of such weak intensity scattered light remains.

3.5. CONCLUSIONS

In this chapter, a scattered light coupling model for the setup of dropping refractive index matching liquid containing NPs onto optical fibre interfaces has been proposed. By simulation, the values of reflections along the Z direction for different sizes of gold NPs from 10 nm to 400 nm were obtained. Experiments with commercial gold NP suspensions were used to evaluate the model and the results are close to the calculated results but slightly lower, which may caused by the deposition of NPs. The size parameter shows an important influence on the intensity of scattered light by NPs and the intensity of scattered light will increase dramatically when the size of NPs increase. For low concentration large size NPs (400 nm diameter gold NPs in experiments) the scattered signal can be detected while for low scattering from small particles (10 nm diameter) is still a challenge to meet. These initial findings give insights to sub-research question 2 that doping small sizes NPs (for example 10 nm diameter) may not have a large increase of backscattered light and larger sizes NPs (for example 400 nm diameter) show the potential to increase the backscattered light dramatically. However, the optimised size of gold NPs for enhancing the backscattered light in the optical fibre is still unknown. Further research on optimisation of the intensity of backscattered light by gold NPs will be investigated in the next chapter.

BIBLIOGRAPHY

[1] M. Froggatt and J. Moore, "High-spatial-resolution distributed strain measurement in optical fiber with Rayleigh scatter", *Applied Optics*, vol. 37, no. 10, pp. 1735–1740, 1998.

[2] B. Soller, D. Gifford, M. Wolfe, M. Froggatt, M. Yu, and P. Wysocki, "Measurement of localized heating in fiber optic components with millimeter spatial resolution", in *2006 Optical Fiber Communication Conference and the National Fiber Optic Engineers Conference*, IEEE, 2006.

[3] J. Song, W. Li, P. Lu, Y. Xu, L. Chen, and X. Bao, "Long-range high spatial resolution distributed temperature and strain sensing based on optical frequency-domain reflectometry", *IEEE Photonics Journal*, vol. 6, no. 3, pp. 1–8, 2014.

[4] S. Wang, K. Lasn, C. W. Elverum, D. Wan, and A. Echtermeyer, "Novel in-situ residual strain measurements in additive manufacturing specimens by using the optical backscatter reflectometry", *Additive Manufacturing*, vol. 32, p. 101 040, 2020.

[5] R. D. Sante, "Fibre optic sensors for Structural Health Monitoring of aircraft composite structures: Recent advances and applications", *Sensors*, vol. 15, no. 8, pp. 18 666–18 713, 2015.

[6] P. M. Bueno, M. Martinez, C. Rans, and R. Benedictus, "Strain monitoring using a Rayleigh backscattering system for a composite UAV wing instrumented with an embedded optical fiber", *Advanced Materials Research*, vol. 1135, pp. 1–19, 2016.

[7] A. Güemes, A. Fernandez-Lopez, and P. Fernandez, "Damage detection in composite structures from fibre optic distributed strain measurements", in *EWSHM-7th European Workshop on Structural Health Monitoring*, L. Cam, Vincent, Mevel, Laurent, Schoefs, and Franck, Eds., Curran Associates, 2018, pp. 528–535.

[8] A. Barrias, J. Casas, and S. Villalba, "A review of distributed optical fiber sensors for civil engineering applications", *Sensors*, vol. 16, no. 5, p. 748, 2016.

[9] S. Loranger, M. Gagné, V. Lambin-Iezzi, and R. Kashyap, "Rayleigh scatter based order of magnitude increase in distributed temperature and strain sensing by simple UV exposure of optical fibre", *Scientific Reports*, vol. 5, no. 1, pp. 1–7, 2015.

[10] F. Parent, S. Loranger, K. K. Mandal, V. L. Iezzi, J. Lapointe, J. S. Boisvert, M. D. Baiad, S. Kadoury, and R. Kashyap, "Enhancement of accuracy in shape sensing of surgical needles using optical frequency domain reflectometry in optical fibers", *Biomedical Optics Express*, vol. 8, no. 4, pp. 2210–2221, 2017.

[11] A. Yan, S. Huang, S. Li, R. Chen, P. Ohodnicki, M. Buric, S. Lee, M. Li, and K. P. Chen, "Distributed optical fiber sensors with ultrafast laser enhanced Rayleigh backscattering profiles for real-time monitoring of solid oxide fuel cell operations", *Scientific Reports*, vol. 7, no. 1, pp. 1–9, 2017.

[12] P. Lu, S. J. Mihailov, D. Coulas, H. Ding, and X. Bao, "Random fiber gratings fabricated using Fs-IR laser for distributed temperature sensor application", in *26th International Conference on Optical Fiber Sensors*, OSA, 2018, FA2.

[13] W. Blanc and B. Dussardier, "Formation and applications of nanoparticles in silica optical fibers", *Journal of Optics*, vol. 45, no. 3, pp. 247–254, 2015.

[14] C. Molardi, S. Korganbayev, W. Blanc, and D. Tosi, "Characterization of a nanoparticles-doped optical fiber by the use of optical backscatter reflectometry", in *Advanced Sensor Systems and Applications VIII*, International Society for Optics and Photonics, vol. 10821, 2018, p. 1 082 121.

[15] A. Beisenova, A. Issatayeva, I. Iordachita, W. Blanc, C. Molardi, and D. Tosi, "Distributed fiber optics 3D shape sensing by means of high scattering NP-doped fibers simultaneous spatial multiplexing", *Optics Express*, vol. 27, no. 16, pp. 22 074–22 087, 2019.

[16] X. Wang, R. Benedictus, and R. M. Groves, "Light scattering and rheological effects in an optical fibre coupled nanoparticle suspension", in *Optical Sensing and Detection VI*, International Society for Optics and Photonics, vol. 11354, 2020, p. 113540V.

[17] A. Quirantes, F. Arroyo, and J. Quirantes-Ros, "Multiple light scattering by spherical particle systems and its dependence on concentration: A T-matrix study", *Journal of Colloid and Interface Science*, vol. 240, no. 1, pp. 78–82, 2001.

[18] C. F. Bohren and D. R. Huffman, *Absorption and Scattering of Light by Small Particles*. Wiley, 1998.

[19] W. F. Bauer, "The Monte Carlo Method", *Journal of the Society for Industrial and Applied Mathematics*, vol. 6, no. 4, pp. 438–451, 1958.

[20] M. Á. Herrador, A. G. Asuero, and A. G. González, "Estimation of the uncertainty of indirect measurements from the propagation of distributions by using the monte-carlo method: An overview", *Chemometrics and Intelligent Laboratory Systems*, vol. 79, no. 1-2, pp. 115–122, 2005.

[21] P. B. Johnson and R. W. Christy, "Optical constants of the noble metals", *Physical Review B*, vol. 6, no. 12, pp. 4370–4379, 1972.

[22] P. Liu, "Optical Coherence Tomography for Material Characterization", PhD Thesis, TU Delft, 2014.

[23] https://www.thorlabs.com/thorproduct.cfm?partnumber=1550BHP.

[24] https://cargille.com/wp-content/uploads/2018/06/Refractive-Index-Liquid-Series-A-n-1.4620-at-589.3-nm-and-25%C2%B0C.pdf.

[25] C. Matzler, "Matlab functions for Mie scattering and absorption", *Institute of Applied Physics, University of Bern, Research Report*, vol. 8, 2002.

[26] https://www.sigmaaldrich.com.

[27] https://www.thorlabs.com/thorproduct.cfm?partnumber=PM20C#ad-image-0.

[28] J. A. Curcio and C. C. Petty, "The near infrared absorption spectrum of liquid water", *JOSA*, vol. 41, no. 5, pp. 302–304, 1951.

[29] M. Tanaka, M. Hirano, K. Murashima, H. Obi, R. Yamaguchi, and T. Hasegawa, "1.7-μm spectroscopic spectral-domain optical coherence tomography for imaging lipid distribution within blood vessel", *Optics Express*, vol. 23, no. 5, pp. 6645–6655, 2015.

[30] C. Blatter, B. Grajciar, R. Huber, and R. A. Leitgeb, "Structural and functional imaging with extended focus dark-field oct at 1300nm", in *Optical Coherence Tomography and Coherence Domain Optical Methods in Biomedicine XV*, International Society for Optics and Photonics, vol. 7889, 2011, p. 78891D.

[31] A. A. Moayed, S. Hariri, V. Choh, and K. Bizheva, "In vivo imaging of intrinsic optical signals in chicken retina with functional optical coherence tomography", *Optics Letters*, vol. 36, no. 23, pp. 4575–4577, 2011.

4

OPTIMISATION OF LIGHT SCATTERING ENHANCEMENT BY GOLD NANOPARTICLES IN FUSED SILICA OPTICAL FIBRE

In chapter 3, it was seen that small nanoparticles usually introduce weak backscattering signals, while large nanoparticles contribute to the enhancement of light scattering. For spherical gold nanoparticles, what is the optimised intensity of light scattering enhancement? In this chapter, the scattering of gold nanoparticles of different sizes will be discussed. Under the constraints of penetration depth defined in this work, the maximum possible light scattering enhancement was obtained by simulation. In the previous chapter 3, the nanoparticle scattering experiments were implemented at the optical fibre interfaces. In order to establish a connection between the light scattering at the interfaces and the light scattering in the optical fibres, an equivalent model of measurement at optical fibre interfaces and backscattered light signal in the optical fibre was built in this chapter, which was used to obtain the intensity of backscattered light of nanoparticle-doped optical fibre with the same concentrations.

Parts of this chapter have been published in Optics Express **29**, 13 (2021): 19450-19464.

A conventional distributed fibre optic sensing system offers close to linear sensitivity along the fibre length. However gold nanoparticles (NP) have been shown to be able to enhance the contrast ratio to improve the quality of signal detection. The challenge in improving the contrast of reflected signals is to optimise the nanoparticle doping concentration over the sensing length to make best use of the distributed fibre sensing hardware. In this chapter, light enhancement by spherical gold NPs in the optical fibres was analysed by considering the size-induced NP refractive index changes. This was achieved by building a new model to relate backscattered light from a gold NP suspension between the optical fibre end tips and backscattered light from gold NPs in the core of the optical fibre. The work provides a model to determine the optimised sizes and concentrations of NPs for sensing at different desired penetration depths in the optical fibre.

This chapter is to further answer sub-research question 2 (If nanometre to micrometre size particles are introduced into an optical fibre, what is the intensity characteristic of the scattered light in optical fibre with these particles?) and to answer sub-research question 3 (The increased scattered light is also likely to reduce the transmission of light along the optical sensing fibre. What is the optimised scattering increase at some key areas?).

4.1. INTRODUCTION

Backscatter reflectometry uses the refractive index (RI) variation of the optical distribution features along the sensing fibre to sense parameters such as strain and temperature [1]. It has been widely used for Structural Health Monitoring (SHM) in aerospace engineering [2]–[4] and civil engineering [5]. As the sensor used to sense these parameters depends on the backscattered light intensity, a low intensity scattering signal from the intrinsic RI fluctuation of the optical fibre is one of the limitations of this technique.

One approach to solve this problem is to dope nanoparticles (NP) into the core of the optical fibre to increase the scattered light signals in the backscatter reflectometry. Blanc and Dussardier [6] described the methods of manufacturing NP-doped in silica optical fibre and analysed the optical intensity loss with Rayleigh scattering. Later Molardi et al. [7] investigated the characteristics of MgO-doped optical fibre and obtained a 50 dB scatterred light increase experimentally. They pointed out the potential use of this approach for spatial multiplexing in optical backscatter reflectometry. Beisenova et al. [8] presented experimental results of 3D shape sensing with a MgO doped optical fibre in a spatial multiplexing structure for an epidural needle. Bulot et al. [9] improved the stability of temperature sensing at a high temperature with zirconia-coated gold NP doped optical fibre in Optical Frequency Domain Reflectometry (OFDR) distributed sensing. These works show the feasibility and the advantages of doping NPs into the core of the optical fibres for distributed sensing, but do not address the optimisation of the NP concentration.

Gold NPs were chosen to be doped into the optical fibre to increase the scattered signals. As a commonly used NP, gold NP has previously been investigated to increase the image contrast for optical coherence tomography (OCT) detection, for example as a bio-compatible contrast agent in tissue [10]–[13]. The reason for choosing gold NPs is that gold NPs have a relatively high reflection coefficient compared to other materials with the same diameter. This is also shown in Figure 4.1, where it can be seen that gold NPs in particular have relatively high scattering efficiencies compared to other metals in fused silica. Another reason is that gold is relatively stable and hard to oxidise. Figure 4.1 also shows that metal oxides in general have lower scattering efficiencies than metals. Therefore, optical fibre doped with gold might have the potential to be used as highly scattering fibre optic sensors.

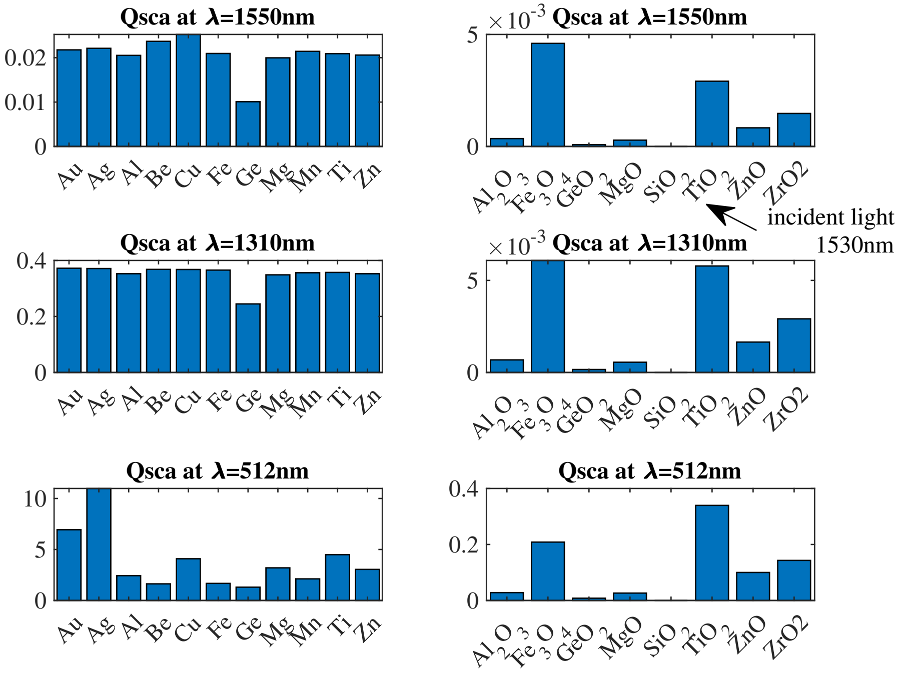

Figure 4.1: The scattering efficiencies for small particles (100 nm diameter) of a variety of materials. The scattering efficiencies were calculated by Mie theory for small particles compared with the wavelengths.

The specific scattering characteristics of gold NPs in optical fibre have not been previously investigated, so the optimised sizes and concentrations of NPs to be doped in the optical fibre to increase the scattered light is unclear.

In chapter 3, a method of dropping liquid containing gold NPs at optical fibre end tips to obtain the backscattered light from the gold NPs at the interfaces was investigated. the levels of light scattering by gold spherical NPs by modelling a broadband light source whose central wavelength was around 1550 nm were evaluated. The experimental results from chapter 3 showed that it is a challenge to detect the scattered light from NPs by means of direct light intensity detection, although the highly sensitive detection method, OCT [14] is a suitable choice. Some OCT systems have the ability to achieve a high sensitivity of over 100 dB [15].

In this work, a novel model connecting size and concentration of gold NP in the core of the optical fibre with the backscattered light signals by a gold NP suspension between the optical fibre end tips to the backscattered light signals will be built. By obtaining the relationship between backscattered light signals at optical fibre end tips, the equivalent backscattered light by NPs in the optical fibre can be obtained. Then the optimised intensity of scattered light from NPs within the desired penetration depths in the optical fibre is able to be determined. An OCT system [16] will be used to detect the scattered light signals from the gold NP suspension between the optical fibre end tips.

This chapter is organized in four sections. The first section is the introduction. The model for analyzing the optimised scattered light with OCT is described in Section 4.2. The results and discussion for different size NPs (1 nm to 400 nm) under a wide wavelength range (400 nm to 1600 nm) are presented in Section 4.3. Section 4.4 is the conclusion.

4.2. MODEL

An optical fibre containing gold NPs in the core is shown schematically in Figure 4.2 (a). The gold NPs are assumed to be homogeneous spherical NPs, which are well dispersed in the core of the optical fibre with a constant concentration. The incident light propagates along the core of the optical fibre from the left to the right side and the light is scattered by the NPs. The scattered light in the backward direction within the total internal reflection angle in the core of the optical fibre is considered reflected. In this work, I am interested in increasing the backscattered light by NPs within a desired NP-doped optical fibre sensor's length to maximize the intensity of backscattered light distributed along an optical fibre for Structural Health Monitoring applications.

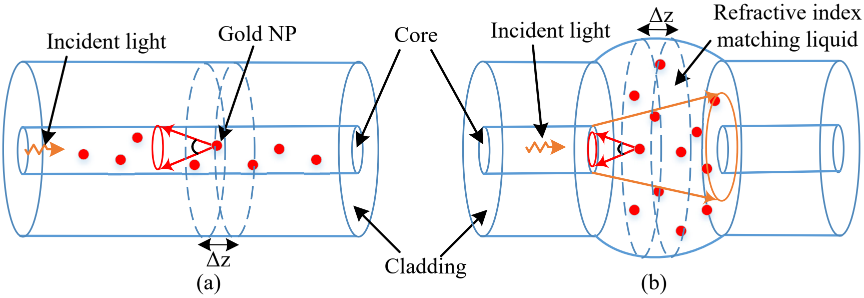

Figure 4.2: Models of scattered light from NPs. (a) Light scattered by the gold NPs in the core of optical fibre; the red dots represent the gold NPs with a constant concentration; propagating light is in orange and the backscattered light is in red with directions; Δz is the spatial resolution for the regions containing gold NPs. (b) Light scattered by the gold NPs at optical fibre interfaces.

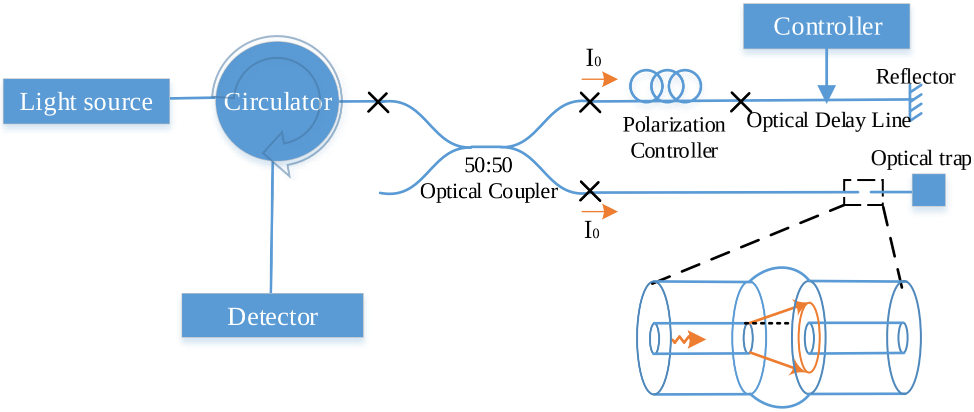

Figure 4.3: The basic structure of the optical detection system combined with OCT to realize the detection of the scattered light from the NPs between the optical fibre interfaces. The optical fibre interface part has been enlarged for clarity. The mounting system for the optical fibre end tips is not shown.

Figure 4.2 (b) shows the structure of the optical fibre end tips. Refractive index (RI) matching liquid containing gold NPs has been dropped at the interfaces. The optical fibre interfaces model is more flexible for laboratory experimental work [17] and will be used here to determine the optimised concentrations of NPs. To obtain the high sensitivity of the backscattered light detection, an OCT system is used, which is shown in Figure 4.3. As shown in Figure 4.3, incident light is emitted from a broadband light source and then propagates into an optical coupler via an optical circulator. The light is split into two beams with a split ratio of 50:50. One of the beams (light power I_0) propagates in the reference arm and is then reflected by a reflector. The other beam (light power I_0) propagates in the sample arm and is scattered by the NPs at the optical fibre end tips. By changing the length of the reference arm with the optical fibre delay line and tuning the polarization of the light by the polarization controller, the reflected light in the reference arm will interfere with the scattered light by the NPs in the sample arm. The interference signals will be measured by the detector.

By constituting the relationship between the backward scattered light in the liquid and the equivalent light scattered by NPs in the core of optical fibre, the latter can be determined.

In the following sections, the model of light scattering by NPs at optical fibre interfaces will be recalled and then compare it with the model of light scattering by NPs in the core of optical fibre to build the relationship between these two models. Once the relationship is obtained, the case of scattered light by the NPs in the optical fibres can be derived by making use of the NP optical fibre end tip interface model.

4.2.1. LIGHT SCATTERING AT OPTICAL FIBRE INTERFACES

In chapter 3 the scattered light at optical fibre interfaces as shown in Figure 4.2 (b) was analysed. The expression for the recoupled scattered light, $I_{recouple}$, by the gold NPs is

$$I_{recouple} = \int_V cT_1 \left(\int_\lambda I_{wavelength}(x,y,z,\lambda) I_s'(\lambda) \exp(-\alpha z)\, \mathrm{d}\lambda \right) \mathrm{d}V, \tag{4.1}$$

where, V is the liquid volume within a certain spatial interval Δz; c is the concentration of gold NPs in RI matching liquid; T_1 is the transmittance between the optical fibre end tip and the liquid; λ is the wavelength of the incident light; $I_{wavelength}$ is the spatial intensity distribution of the light incident on the NPs; x, y and z are the spatial positions of the centre of the NPs; I_s' is the scattering response by NPs which can be recoupled into the left optical fibre and α is the attenuation caused by the absorption from RI matching liquid and the extinction by NPs.

In Equation 4.1, the single scattering model is used due to the concentration of NPs (optical depth $\tau = cC_{ext}z < 1$ [18]), where C_{ext} is the extinction cross section of the NP. The light backscattered by the NPs propagates backwards and attenuates by absorption in the RI matching liquid and extinction by the NPs. Then, the backscattered light is recoupled into the optical fibre.

Due to the relatively small sizes of NPs (1 nm to 400 nm) in the RI matching liquid, the propagating light incident on the NPs is regarded as a plane wave which can be treated with Mie theory [19].

The spatial intensity distribution of the light in the liquid was modelled as Gaussian-profile planes with a z-distance-related profile amplification ratio. The spectra of the incident light was modelled as a Gaussian distribution spectra (see [17] for further details).

If the scattering intensity $|\chi|^2$ of the NP in the backward direction is used as the mean scattering intensity, I_s', can be approximated as

$$I_s'(\lambda) \approx \frac{(\lambda/n_{liquid})^2}{\pi} |\chi(\pi)|^2 \gamma(x,y,z) \frac{\Omega}{4\pi}. \tag{4.2}$$

$$\Omega = 2\pi(1-\cos\zeta), \tag{4.3}$$

where, n_{liquid} is the RI of the RI matching liquid; $\gamma(x,y,z)$ is the coupling efficiency of the light scattered by NPs at positions (x,y,z); and ζ is the numerical aperture angle in the liquid. Note: the values of $\chi(\pi)$ are related to the incident light wavelengths. For a broadband light source, if $\chi(\pi)$ and the RI of the medium can be regarded as constants for a certain size spherical gold NPs and the spatial interval is small, then Equation 4.1 can be approximated as

$$I_{recouple} = BI_0C(z)\Delta z \mu_b \Omega \exp(-2\alpha z_0), \tag{4.4}$$

where,

$$B = \frac{T_1^2}{8\pi^2}, \tag{4.5}$$

$$C(z) = \frac{2\pi}{(2\sigma_0/k(z_0))^2\pi/2}\int_0^\infty \exp\left(-2\left(\frac{r}{2\sigma_0/k(z_0)}\right)^2\right)\gamma r\,\mathrm{d}r, \tag{4.6}$$

where, $\Delta\lambda$ is the full width at half maximum (FMHW) of the light source, λ_c is the central wavelength of the light source, z_0 is the centre of the spatial interval, k is the profile amplification ratio, $r = \sqrt{x^2+y^2+z^2}$ and $2\sigma_0$ represents the mode field radius of the incident light in the optical fibre.

The form of Equation 4.4 is similar to the case of a OCT system with the light focused in the sample path [20], [21], but adjusted by $B(z)$ according to the bandwidth of the light source. The aperture function [22], [23] of the interferometer from a focusing lens has been substituted by $C(z)$ for the case of interfaces.

4.2.2. LIGHT SCATTERING IN THE CORE OF AN OPTICAL FIBRE

Under the same assumptions, the light backscattered by the NPs in the optical fibre can be expressed as

$$I'_{recouple} = \int_V c\left(\int_\lambda I'_{wavelength}(x,y,z,\lambda) I''_s(\lambda)\exp(-\alpha' z)\,\mathrm{d}\lambda\right)\mathrm{d}V, \tag{4.7}$$

where, $I'_{wavelength}$ is the light propagating in the optical fibre; and I''_s is the scattered light by the NPs which propagates backwards in the optical fibre. As the light is confined in the optical fibre, the expression for the light propagating in the optical fibre can be expressed as

$$I'_{wavelength}(x,y,z,\lambda) = \exp(-\alpha' z)\times I(\lambda)\times\frac{1}{(2\sigma_0))^2\pi/2}\times\exp\left(-2\left(\frac{r}{2\sigma_0}\right)^2\right). \tag{4.8}$$

$I''_s(\lambda)$ has the same form as Equation 4.2.

$$I''_s(\theta',\varphi',r',\lambda) \approx \frac{(\lambda/n_{liquid})^2}{\pi}|\chi(\pi)|^2\Gamma\frac{\Omega'}{4\pi}. \tag{4.9}$$

$$\Omega' = 2\pi(1-\cos\zeta') \tag{4.10}$$

where, Γ is the coupling efficiency in the optical fibre, and ζ' is the numerical aperture angle in the core of the optical fibre.

In this case, the light scattered by the NPs at the z_0 position with spatial resolution Δz propagates backwards along the fibre and can be expressed as

$$I'_{recouple} = B' I_0 C'(z)\Delta z\mu_b\Omega'\exp(-2\alpha' z_0). \tag{4.11}$$

where,

$$B' = \frac{1}{8\pi^2}, \tag{4.12}$$

$$C'(z) = \Gamma \tag{4.13}$$

α' is the attenuation coefficient caused by the absorption by the optical fibre and the extinction by the NPs.

Comparing Equation 4.4 and Equation 4.11, the relationship between the two models can be obtained

$$I'_{recouple} = I_{recouple} \times \frac{1}{T_1^2} \times \frac{\Gamma}{C(z)} \times \frac{\Omega'}{\Omega} \times \exp(-2(\alpha' - \alpha)z_0). \tag{4.14}$$

According to Equation 4.14, when the light is recoupled into the liquid ($I_{recouple}$), the transmittance of the interfaces between liquid and fibre (T_1), the spatial coupling efficiency in the liquid ($C(z)$), the coupling efficiency in the core of optical fibre (Γ), and Ω', Ω, α' and α are given or can be obtained from experiments or simulations. Therefore the equivalent backscattered light in the optical fibre can be calculated.

4.2.3. SIGNAL DETECTION BY OCT AND THE LIGHT ENHANCEMENT EVALUATION

For an OCT system, if the optical coupler split ratio is 50:50, the signal detected by the photodetector can be expressed as [20], [24]

$$i(z) = KI_0\sqrt{BC(z)L_c}\sqrt{\mu_b\Omega}\exp(-\alpha z), \tag{4.15}$$

where, K is the gain of the photodetector and I_0 is the light power in the sample arm incident on the gold NPs (Note: in this case the total light power from the light source is $2I_0$). For light that is in the core of optical fibre, as shown in Figure 4.2 (a), the signal detected by the photodetector can be expressed as

$$i'(z) = KI_0\sqrt{B'C'(z)L_c}\sqrt{\mu_b\Omega'}\exp(-\alpha' z). \tag{4.16}$$

Therefore, the relationship between the signal detected by the core of optical fibre $i'(z)$ and that detected in liquid $i(z)$ can be expressed as

$$i'(z) = i(z) \times \sqrt{\frac{1}{T_1^2} \times \frac{\Gamma}{C(z)} \times \frac{\Omega'}{\Omega}} \times \exp(-(\alpha' - \alpha)z_0). \tag{4.17}$$

According to the form of Equation 4.15 and Equation 4.16, the light enhancement coefficient $R_{enhancement}$ from the NPs for both cases is defined as

$$R_{enhancement}(z) = \sqrt{\mu_b}\exp(-\mu_t z). \tag{4.18}$$

Equation 4.18 will be used to show the system response to scattered light by the NPs at z positions, $\mu_t = \alpha'$ for the case in the RI matching liquid and $\mu_t = \alpha$ for the case in the core of optical fibre.

As shown in Equation 4.18, the enhancement is caused by the backscattering from NPs (μ_b), but the light loss is adjusted by μ_t. $\mu_t = \mu_{extNP} + \mu_{aMedium}$ where, μ_{extNP} is the light extinction caused by NPs and $\mu_{aMedium}$ is the absorption by the media.

The depth of the detected signal is defined with 3dB loss as the penetration depth, which also means that the light enhancement coefficient $R_{enhancement}$ loses half of its value at depth $z = l_{depth}$. This part of the loss is the light extinction by introducing the NPs (Note: the total loss is the combination of both the loss caused by the NPs and the loss caused by the medium). Then, the penetration depth seen by the detector can be expressed as

$$l_{depth} = \frac{\ln 2}{\mu_{extNP}}. \tag{4.19}$$

A high enhancement within an expected penetration depth is expected. More details about the relevant parameters of the light enhancement coefficient in Equation 4.18 (μ_b and μ_t) will be described in the next part.

4.2.4. THE PARAMETERS USED FOR LIGHT ENHANCEMENT BY GOLD NPS

When the concentration of the NPs is low only single scattering from the NPs is considered. In this case, $\mu_{extNP} = cC_{ext}$ [19], where c is the concentration, namely the number of particles in a unit volume and C_{ext} is the extinction cross section of the NP. In this chapter, I consider monotonous spherical particles, so $\mu_{extNP} = cC_{ext} = c\pi(D/2)^2 Q_{ext}$, where D is the diameter of the NP, $\mu_b = c\pi(D/2)^2 Q_b$, Q_{ext} is the extinction coefficient and Q_b is the backscattering coefficient of a NP. If the volume ratio (ρ) of the NPs to the liquid is assumed to be

$$\rho = \frac{V_{NPs}}{V_{liquid}} = c\frac{4\pi}{3}\left(\frac{D}{2}\right)^3, \tag{4.20}$$

then, $\sqrt{\mu_b}$ and μ_{extNP} can be expressed as

$$\sqrt{\mu_b} = \sqrt{\rho\frac{3}{2D}Q_b}, \tag{4.21}$$

$$\mu_{extNP} = \rho\frac{3}{2D}Q_{ext}. \tag{4.22}$$

Q_b is the scattering intensity enhancement from the NPs and Q_{extNP} is the signal attenuation through the depth, caused by the NPs. Therefore, the penetration depth can be expressed as

$$l_{depth} = \frac{2D\ln 2}{\rho 3 Q_{ext}}. \tag{4.23}$$

Therefore, if the scattering parameters (for example, Q_{ext}, Q_b) are obtained the enhancement of the scattered light is determined.

Mie theory [19] was used to illustrate the influence of different sizes of gold NPs at different incident wavelengths. Scattering efficiency and extinction efficiency were taken into comparison for these cases to show the ratio of light scattered by the gold NPs to the extinction ratio.

The definition of scattering efficiency is [19]

$$Q_{sca} = \frac{2}{x^2}\sum_{n=1}^{\infty}(2n+1)\left(|a_n|^2 + |b_n|^2\right). \tag{4.24}$$

The definition of extinction efficiency is

$$Q_{ext} = \frac{2}{x^2} \sum_{n=1}^{\infty} (2n+1)\, Re\,(a_n + b_n)\,. \tag{4.25}$$

The absorption efficiency can then be calculated as

$$Q_{abs} = Q_{ext} - Q_{sca}, \tag{4.26}$$

where, x is the size parameter, a_n and b_n are the scattering coefficients in the Mie calculation [19] and Q_b is the backscattering efficiency, which is defined as [19]

$$Q_b = \frac{1}{x^2} \left| \sum_{n=1}^{\infty} (2n+1)\,(-1)^n\,(a_n - b_n) \right|^2 . \tag{4.27}$$

The size parameter x is related to the ratio of the RI of the particle to the medium. Generally, the RI of bulk gold can be used in the calculation when the size of the particle is large. However, for small size gold particles especially the nanometer size gold particles investigated in this chapter, the refractive indices at smaller sizes will have an influence on the scattering and extinction efficiencies. Therefore, the size-induced RI change of gold NPs needs to be considered.

The specific size-dependent complex dielectric function of gold NPs can be expressed as [25]

$$\epsilon(\omega) = 1 - \frac{\omega_p^2}{\omega^2 + i(\gamma_{bulk+H\frac{v_F}{R}})\omega} + Q_{bulk}[1 - \exp(-\frac{R}{R_0})]G(\omega), \tag{4.28}$$

$$G(\omega) = \int_{\omega_g}^{\infty} \frac{\sqrt{\omega' - \omega_g}}{\omega'} [1 - F(\omega', T)] \frac{\omega'^2 - \omega_g^2 + \gamma_b^2 + i2\omega\gamma_b}{(\omega'^2 - \omega_g^2 + \gamma_b^2)^2 + 4\omega^2\gamma_b^2} \mathrm{d}\omega', \tag{4.29}$$

where, ω and ω' are the angular frequency, ω_p is the bulk plasma frequency of gold, γ_{bulk} is the damping constant for free electrons, H is a scattering constant, v_F is the electron velocity at the Fermi surface, R is the radius of the gold particle, Q_{bulk} is the coefficient for bound electron contribution, R_0 is the fit value, ω_g is the frequency corresponding to the gap energy of gold, $F(\omega, T) = 1/(\exp\frac{\hbar\omega - E_f}{k_b T} + 1)$ is the Fermi energy distribution, k_b is the Boltzmann constant, E_f is the Fermi energy and γ_b is the damping constant for bound electrons. The specific values of these parameters used are shown in Table 4.1.

The calculated results of RI within the 400 nm to 1600 nm incident light range match the experimental data[27] when $R = \infty$ in Equation (4.28) . Therefore, the RI calculation matches the experimental data well between 400 nm to 1600 nm for bulk gold. When the sizes of the gold NPs are small, the values of RI will deviate from the experimental data from bulk gold. This deviation (error) is defined, to evaluate the influence of size-induced scattering parameters changes, with the expression

$$ErrorQ_i = \frac{Q_{i-nano} - Q_{i-bulk}}{Q_{i-nano}} \times 100\%, \quad i = b, sca, abs, ext. \tag{4.30}$$

Table 4.1: The relevant parameters for calculating the complex dielectric of gold

Parameter	Value
ω_p	13×10^{15} Hz [26]
γ_{bulk}	1.1×10^{14} Hz [27]
H	0.8 [25]
v_F	14.1×10^{14} nm s^{-1} [26]
Q_{bulk}	2.3×10^{24} [25]
R_0	0.35 nm [25]
ω_g	3.19×10^{15} Hz [25]
E_f	2.5 eV [25]
T	301.5 K
γ_b	2.4×10^{14} Hz [28]

where, b, sca, abs and ext represent backward scattering, scattering, absorption and extinction respectively.

When the RI of bulk gold is used in the calculation for the gold NPs in fused silica, errors will arise. To evaluate these errors, Equation 4.30 is used. Figure 4.4 (a) shows the errors between backscattering efficiencies calculated using the RI of gold NPs and the RI of bulk gold. The RI of the medium (fused silica) used is from Malitson's work [29]. Very high errors occur when the diameters of the NPs are less than 10 nm and when the wavelength is around 500 nm. If the backscattering efficiency needed is in this range, the size-induced refractive index change should be treated carefully. When the size of the NPs and the wavelengths deviate from this region, the errors are relative small (below 10 %). The errors in the extinction efficiencies are shown in Figure 4.4 (b). Figure 4.4 (c) shows the errors for the absorption efficiencies. The similarity of Figure 4.4 (b) and Figure 4.4 (c) shows that the errors in absorption efficiencies are the main influence on the errors in extinction efficiencies and scattering and the errors in backscattering have a relatively low influence on the extinction parameter errors.

From the analyses above, it can be seen that in most of the region the size-induced efficiency changes are small, but for a more precise calculation, in this chapter the size-dependent RI for gold NPs will be used.

The attenuation of the medium (fused silica) can be expressed as [30], [31].

$$\mu_{aMedium} \approx \alpha_{Rayleigh} + \alpha_{IR} \tag{4.31}$$

where, $\alpha_{Rayleigh}$ is the loss caused by the density density fluctuations of the material and α_{IR} is the loss caused by the vibration absorption in fused silica.

$$\alpha_{Rayleigh} = 5 \times 10^{-5} n_0^2 p^2 K_T(T_g) T_g / \lambda^4 \tag{4.32}$$

where, $n_0 = 1.46$; $p = 0.22$; $K_T \approx 6 \times 10^{-11}$ Pa in Equation 4.32, $T_g = 1450K$, λ in unit µm. [30]

$$\alpha_{IR} = A_i \exp(-a_i/\lambda) \tag{4.33}$$

where, $A_i \approx 6 \times 10^{11}$ dB/km and $a_i \approx 48$ µm. [30]

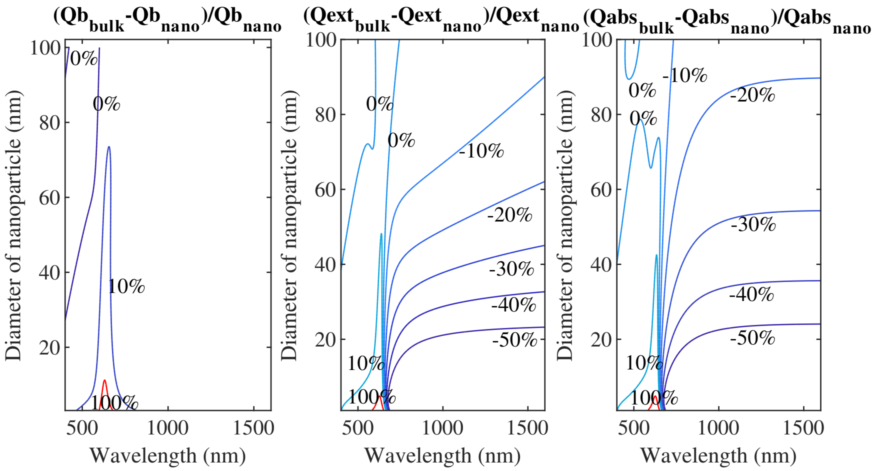

(a) (b) (c)

Figure 4.4: Calculated scattering parameters errors between size-dependent refractive index and bulk refractive index, the wavelength range is from 400 nm to 1600 nm, the diameter range of NPs is from 1 nm to 100 nm. (a) The backscattering efficiency errors. (b) The extinction efficiency errors. (c) The absorption efficiency errors in fused silica.

4.3. RESULTS AND DISCUSSION

4.3.1. SCATTERING CHARACTERISTICS FOR SAME VOLUME RATIOS GOLD NPS IN FUSED SILICA

Figure 4.5 shows the scattering character from homogeneous NPs with a certain concentration in the same volume ratio. The values of $\sqrt{\mu_b}/\sqrt{\rho}$ are shown in Figure 4.5 (a). $\sqrt{\mu_b}$ equals the light enhancement coefficient at $z = 0$ ($R_{enhancement}(0)$).

It is well-known that the intensities and the angles of the scattering lobes depend on the ratio of the size of the NPs, the wavelength of the incident light and the refractive index. A larger size of NP supports more modes [32]. As shown in Figure 4.5 (a), when the sizes of the NPs increase, multipolar modes are generated. The peak becomes broader and the central wavelength of the peak shows a red shift. Figure 4.5 (b) is the contour map of Figure 4.5 (a) to show some boundaries, namely 1 mm$^{-1/2}$, 10 mm$^{-1/2}$ and 100 mm$^{-1/2}$. If the penetration depth does not need to be considered, for the same volume ratio of NP suspensions the optimised region appears when in the incident wavelength ranges from about 500 nm to about 1000 nm for a diameter region from about 50 nm to about 200 nm.

If the penetration depth is taken into consideration, the penetration depth multiplied by the volume ratio shown in Figure 4.5 (c) can be used to restrict the optimised region. If the values shown in Figure 4.5 (c) are divided by ρ, the penetration depth can be obtained. Figure 4.5 (d), the contour map of Figure 4.5 (c), shows some boundaries which will be used to evaluate the penetration depth levels. Some specific values are chosen in Figure 4.5 (d) namely 2×10^{-3} mm, 2×10^{-4} mm and 2×10^{-5} mm. For example, for the same volume ratio 1×10^{-6}, the corresponding

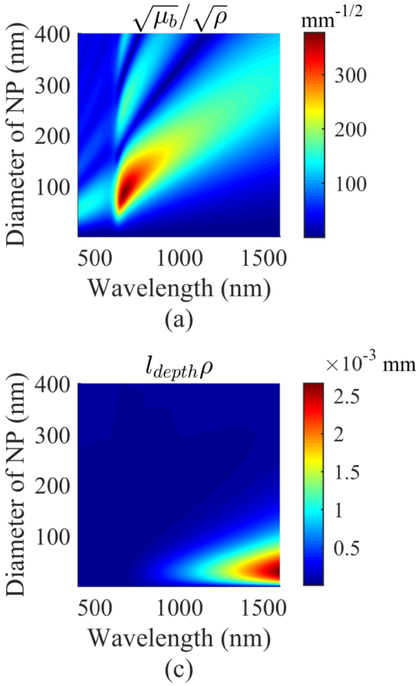

Figure 4.5: Backscattering by NPs and penetration depth relative parameter with specific gold NP volume ratio. (a) The backscattering by NPs with volume ratio. (b) Contour map of backscattering by NPs with volume ratio. (c) The penetration depth with volume ratio. (d) Contour map of the penetration depth with volume ratio.

penetration depths are 2000 mm, 200 mm and 20 mm respectively. It can be seen from Figure 4.5 (d) that for NPs' sizes smaller than 200 nm, the penetration depths for the infrared incident light are longer than those in the visible incident light range. For larger size NPs and in the whole wavelength range, the penetration depths are between about 20 mm and about 200 mm if the volume ratio is 1×10^{-6}.

The light wavelength at 1550 nm is what I am mostly concerned with because the light source of the optical system for strain detection (LUNA ODiSI-B) is around this wavelength as well as the light source of the OCT which I will use for the optical fibre interfaces test. In the next part, the optimised light enhancement for gold NPs in fused silica at 1550 nm will be investigated.

4.3.2. OPTIMISED LIGHT ENHANCEMENT FOR GOLD NPS IN FUSED SILICA AT 1550 nm WAVELENGTH

According to Equation (4.21), $\sqrt{\mu_b}$ is proportion to $\sqrt{\rho}$. Therefore, in order to determine the maximum value of light enhancement coefficient for a certain diameter of NP, ρ needs to be increased to its maximum within the limitation of the penetration depth. If the maximum of ρ is derived, then the corresponding maximum light enhancement coefficients can be derived. The maximum of ρ and the corresponding maximum light enhancement coefficients for $z = 0$ are shown in Figure 4.6.

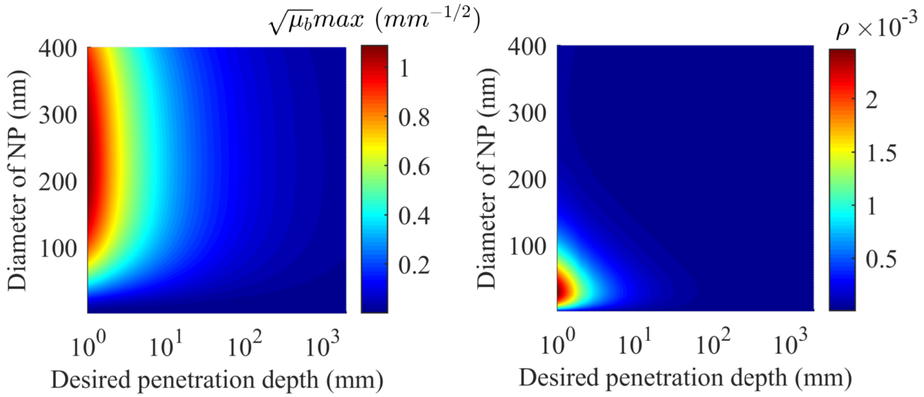

(a) (b)

Figure 4.6: The maximum $\sqrt{\mu_b}$ with the corresponding volume ratio ρ; the desired penetration depth in the figure is set to be from 1 mm to 2 m; the diameter of the NP is from 1 nm to 400 nm. (a) The maximum $\sqrt{\mu_b}$. (b) The corresponding volume ratio ρ.

For the whole desired penetration depth shown in Figure 4.6, from 1 mm to 2 m, the maximum of $\sqrt{\mu_b}$ occurs at the diameter of NPs of about 224 nm as shown in Figure 4.6 (a). The corresponding volume ratios ρ to achieve the maximums of $\sqrt{\mu_b}$ are shown in Figure 4.6 (b). It can be seen from Figure 4.6 (b) that smaller size gold NPs have a lower scattering, for example a NP size below 50nm even if the volumn ratio is much higher than larger size gold NPs as shown in Figure 4.6 (a). Another thing to be noted is that the optimised size of gold NPs to achieve the

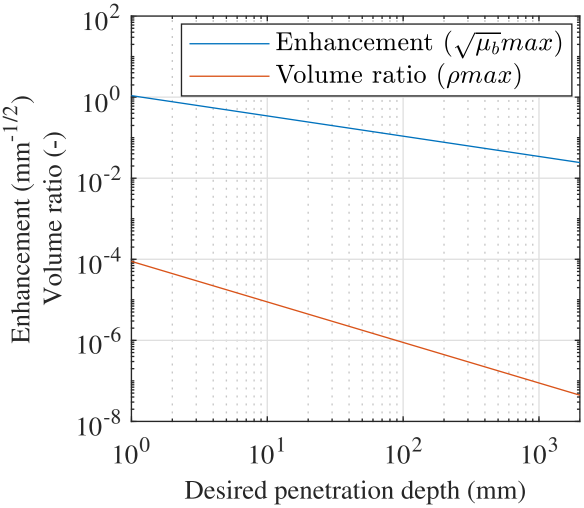

Figure 4.7: The maximum $\sqrt{\mu_b}$ with the corresponding volume ratio ρ at the optimised NP diameter (224 nm).

highest scattering is at 224 nm, which is different from the result from Figure 4.5 (a). In Figure 4.5 (a), the maximum value is obtained for NPs of about 315 nm at the incident wavelength 1550 nm. It is strange at first glance. One reason for this is that the penetration depth which was defined in order to determine the scattered light in a desired depth does not decrease dramatically and limits the volume ratio. $\sqrt{\mu_b}$ is related to the volume ratio. If the attenuation caused by the NPs is not concerned about and only look to the higher scattering at the start of the doping fibre, the optimised size of gold NPs is 315 nm.

Figure 4.7 shows the maximum $\sqrt{\mu_b}$ (maxium $R_{enhancement}$ at $z = 0$) with the corresponding volume ratio ρ at the optimised NP diameter (224 nm). In the next part, three cases of light enhancement by NPs at the optimised size of NPs (224 nm) with a broadband Gaussian spectra light source with central wavelength 1550 nm will be shown.

4.3.3. CASE OF 224 nm DIAMETER GOLD NPS IN FUSED SILICA AT 1550 nm WAVELENGTH

An OCT system whose central wavelength is at 1550 nm and has a FMHW of 60 nm was used to detect the scattered light between the optical fibre end tips. The gold NPs with the optimised size (224 nm diameter) are introduced into the RI matching liquid. The signals detected by the OCT are used to recover the reflected light signals in the optical fibre with the same size and concentration of gold NPs. Three cases are simulated. The penetration depths are set at 10 mm, 100 mm and 1000 mm, respectively.

The attenuation of the RI matching liquid is assumed as 0.02 mm^{-1}, Γ=1. Other parameters used in the calculations are listed in Table 4.2 and Table 4.3.

Table 4.2: Three cases for calculation

l_{depth}	ρ_{max}	c	μ_b	μ_{extNP}
10 mm	8.87×10^{-6}	1.51×10^{9} mL^{-1}	1.15×10^{-1} mm^{-1}	6.93×10^{-2} mm^{-1}
100 mm	8.87×10^{-7}	1.51×10^{8} mL^{-1}	1.15×10^{-2} mm^{-1}	6.93×10^{-3} mm^{-1}
1000 mm	8.87×10^{-8}	1.51×10^{7} mL^{-1}	1.15×10^{-3} mm^{-1}	6.93×10^{-4} mm^{-1}

Table 4.3: Other parameters used for calculation

Parameter	Value
I_0	1 mW
K	1.0 A/W
T_1	1
$2\sigma_0$	4.75 µm
$\Omega \approx \Omega'$	0.0252
$\mu_{Opticalfibre}$	2.99×10^{-8} mm (0.13 dB/km)
$n_{Opticalfibre} = n_{liquid}$	1.452

The Monte Carlo Method is used in the calculation to generate the scattered signals detected by the OCT system according to Equation 4.6 and Equation 4.15 as shown in Figure 4.8 (a). For each spatial resolution (12 µm), 1000 random points are used for the Monte Carlo calculation. Then, the detected signals by the OCT system are adjusted to the equivalent signals in the optical fibre based on Equation 4.16 and then the light intensity signals can be recovered based on Equation 4.11.

The recovered signals are shown in Figure 4.8 (b). The total calculating time is about 13 h on a computer with the 1.80 GHz central processing unit (Intel i7-10610U).

Figure 4.8 (a) shows the results detected by the photodetector in the structure of the optical fibre end tips with the RI matching liquid containing 224 nm size gold NPs. The total depth shown in Figure 4.8 (a) presents the distance between the two optical fibre end tips in the simulation, but for a real setup the total depth depends on the liquid bubble's size. Figure 4.8 (b) is the corresponding reflected light in the liquid recoupled into optical fibre which is calculated from the generated data from Figure 4.8 (a). It can be seen that there are highly reflected signals from the gold NPs (about −55 dBm) near one end tip of the optical fibre. The corresponding reflected light signal to the incident light is about −36 dB/mm, which is much higher than the reflected to incident light ratio in the optical fibre (about −100 dB/mm [33]). Figure 4.8 (c) shows the recovered reflected light signals in the optical fibre according to the relationship between the detected signals between optical fibre interfaces and in the optical fibre. In Figure 4.8 (c), the reflected signal at the penetration depths is about 6 dBm lower than at the beginning of the NP-doped optical fibre sensors (the penetration depths are 10 mm, 100 mm and 1000 mm respectively).

For the 1550 nm wavelength light source, the attenuation from the optical fibre is low, but for other wavelength regions the attenuation can be high. Therefore,

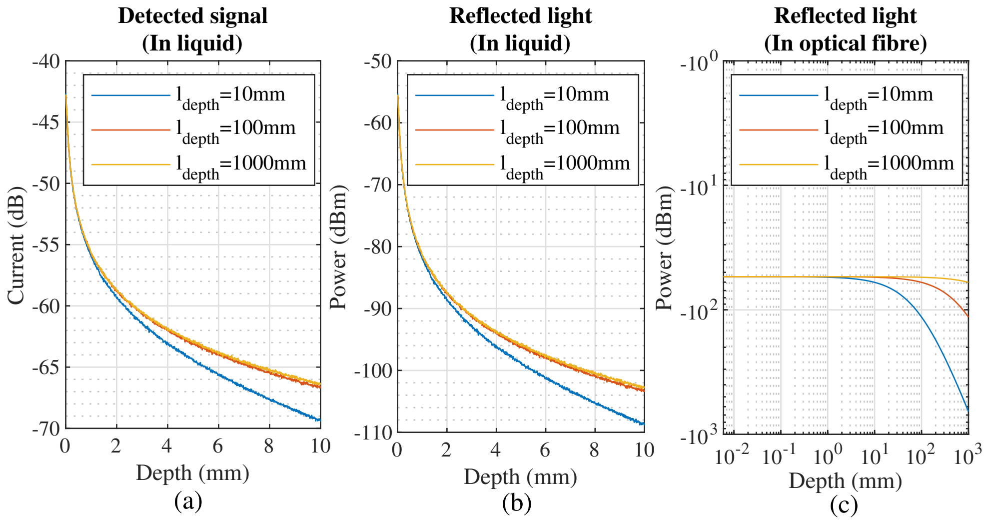

(a)

(b)

(c)

Figure 4.8: Detected signal by the OCT system and the recovered signals in the optical fibre. (a) The current from the photodetector of the OCT system simulated between the optical fibre interfaces with RI matching liquid containing gold NPs. (b) The corresponding reflected light in the liquid recoupled into optical fibre. (c) The recovered reflected light power in the optical fibre.

the loss may be much higher than 3 dBm for other regions of wavelengths of the light source. It also needs to be noted that for the case that the wavelengths of the light source are near the resonance peaks of gold NPs with a broad bandwidth, the approximation may have a large error and the recoupled light should be calculated by Equation 4.1.

The optical fibre in this work is a solid optical fibre. To dope gold NPs in an optical fibre, different sizes of homogeneous gold NPs can be synthesized [34], [35] and the shape of the gold NPs can be well controlled [36], [37]. The solution doping method [38], [39] can then be used to dope gold NPs with porous silica soot by conventional Modified Chemical Vapor Deposition (MCVD) process [6], [40].

4.4. CONCLUSION

The intensity characteristic of the scattered light in optical fibre by gold NPs with sizes from 1 nm to 400 nm was obtained in this work, which answered sub-research question 2: If nanometre to micrometre size particles are introduced into an optical fibre, what is the intensity characteristic of the scattered light in optical fibre with these particles? The optimised sizes for light scattering enhancement have been obtained by consideration of the penetration depth or without considering the penetration depth. For 1550 nm incident light, the best size of gold NPs for light enhancement is around 315 nm if the penetration depth is not taken into consideration. If the penetration depth is taken into consideration the optimised size of gold NPs is about 224 nm. These findings give answers to sub-research question 3 (The increased scattered light is also likely to reduce the transmission of light along the optical sensing fibre. What is the optimised scattering increase at some key areas?) by restricting penetration depth for the optical fibre sensors used for critical areas. In addition, the relationship between the two models, the light scattering model at optical fibre interfaces and light scattering model in the optical fibre, has been obtained. Three cases at the optimised sizes and concentrations are shown with their desired penetration depths to show the distributed reflected signals in the three NP-doped optical fibres. These results can be used for developing highly scattering gold NP-doped optical fibre sensors which rely on high intensity of backscattered light for the future.

4.5. DATA AVAILABILITY

The dataset for the results in the chapter is available in the 4TU.ResearchData, Ref. [41] (https://doi.org/10.4121/14540823).

BIBLIOGRAPHY

[1] X. Bao and L. Chen, "Recent progress in distributed fiber optic sensors", *Sensors*, vol. 12, no. 7, pp. 8601–8639, 2012.

[2] R. D. Sante, "Fibre optic sensors for Structural Health Monitoring of aircraft composite structures: Recent advances and applications", *Sensors*, vol. 15, no. 8, pp. 18 666–18 713, 2015.

[3] P. M. Bueno, M. Martinez, C. Rans, and R. Benedictus, "Strain monitoring using a Rayleigh backscattering system for a composite UAV wing instrumented with an embedded optical fiber", *Advanced Materials Research*, vol. 1135, pp. 1–19, 2016.

[4] A. Güemes, A. Fernandez-Lopez, and P. Fernandez, "Damage detection in composite structures from fibre optic distributed strain measurements", in *EWSHM-7th European Workshop on Structural Health Monitoring*, L. Cam, Vincent, Mevel, Laurent, Schoefs, and Franck, Eds., Curran Associates, 2018, pp. 528–535.

[5] A. Barrias, J. Casas, and S. Villalba, "A review of distributed optical fiber sensors for civil engineering applications", *Sensors*, vol. 16, no. 5, p. 748, 2016.

[6] W. Blanc and B. Dussardier, "Formation and applications of nanoparticles in silica optical fibers", *Journal of Optics*, vol. 45, no. 3, pp. 247–254, 2015.

[7] C. Molardi, S. Korganbayev, W. Blanc, and D. Tosi, "Characterization of a nanoparticles-doped optical fiber by the use of optical backscatter reflectometry", in *Advanced Sensor Systems and Applications VIII*, International Society for Optics and Photonics, vol. 10821, 2018, p. 1 082 121.

[8] A. Beisenova, A. Issatayeva, I. Iordachita, W. Blanc, C. Molardi, and D. Tosi, "Distributed fiber optics 3D shape sensing by means of high scattering NP-doped fibers simultaneous spatial multiplexing", *Optics Express*, vol. 27, no. 16, pp. 22 074–22 087, 2019.

[9] P. Bulot, O. Cristini, M. Bouet, A. Demol, L. Bigot, G. Bouwmans, S. Plus, R. Habert, G. Laffont, and M. Douay, "OFDR distributed temperature sensing at 800 °C on a fiber with enhanced Rayleigh scattering profile by doping", in *Bragg Gratings, Photosensitivity and Poling in Glass Waveguides and Materials*, Optical Society of America, 2018, BM3A–2.

[10] C. S. Kim, P. Wilder-Smith, Y. Ahn, L. L. Liaw, Z. Chen, and Y. J. Kwon, "Enhanced detection of early-stage oral cancer in vivo by optical coherence tomography using multimodal delivery of gold nanoparticles", *Journal of Biomedical Optics*, vol. 14, no. 3, p. 034 008, 2009.

[11] Y. Huang, M. Li, D. Huang, Q. Qiu, W. Lin, J. Liu, W. Yang, Y. Yao, G. Yan, N. Qu, V. V. Tuchin, S. Fan, G. Liu, Q. Zhao, and X. Chen, "Depth-resolved enhanced spectral-domain OCT imaging of live mammalian embryos using gold nanoparticles as contrast agent", *Small*, vol. 15, no. 35, p. 1 902 346, 2019.

[12] E. İ. Altınoğlu and J. H. Adair, "Near infrared imaging with nanoparticles", *Wiley Interdisciplinary Reviews: Nanomedicine and Nanobiotechnology*, vol. 2, no. 5, pp. 461–477, 2010.

[13] Y. Ponce de León, J. Pichardo-Molina, N. Alcalá Ochoa, and D. Luna-Moreno, "Contrast enhancement of optical coherence tomography images using branched gold nanoparticles", *Journal of Nanomaterials*, vol. 2012, pp. 1–9, 2012.

[14] D. Huang, E. Swanson, C. Lin, J. Schuman, W. Stinson, W. Chang, M. Hee, T. Flotte, K. Gregory, C. Puliafito, and J. G. Fujimoto, "Optical coherence tomography", *Science*, vol. 254, no. 5035, pp. 1178–1181, 1991.

[15] M. Tanaka, M. Hirano, K. Murashima, H. Obi, R. Yamaguchi, and T. Hasegawa, "1.7-μm spectroscopic spectral-domain optical coherence tomography for imaging lipid distribution within blood vessel", *Optics Express*, vol. 23, no. 5, pp. 6645–6655, 2015.

[16] P. Liu, R. M. Groves, and R. Benedictus, "3D monitoring of delamination growth in a wind turbine blade composite using optical coherence tomography", *NDT & E International*, vol. 64, pp. 52–58, 2014.

[17] X. Wang, R. Benedictus, and R. M. Groves, "Modelling of light scattering by gold nanoparticles at optical fibre interfaces", *Journal of Optics*, vol. 23, no. 3, p. 035 602, 2021.

[18] A. Quirantes, F. Arroyo, and J. Quirantes-Ros, "Multiple light scattering by spherical particle systems and its dependence on concentration: A T-matrix study", *Journal of Colloid and Interface Science*, vol. 240, no. 1, pp. 78–82, 2001.

[19] C. F. Bohren and D. R. Huffman, *Absorption and Scattering of Light by Small Particles*. Wiley, 1998.

[20] J. M. Schmitt, A. R. Knuettel, A. H. Gandjbakhche, and R. F. Bonner, "Optical characterization of dense tissues using low-coherence interferometry", in *Holography, Interferometry, and Optical Pattern Recognition in Biomedicine III*, International Society for Optics and Photonics, vol. 1889, 1993, pp. 197–211.

[21] J. M. Schmitt, A. Knuttel, M. Yadlowsky, and M. A. Eckhaus, "Optical-coherence tomography of a dense tissue: Statistics of attenuation and backscattering", *Physics in Medicine and Biology*, vol. 39, no. 10, pp. 1705–1720, 1994.

[22] J. A. Izatt, E. A. Swanson, J. G. Fujimoto, M. R. Hee, and G. M. Owen, "Optical coherence microscopy in scattering media", *Optics Letters*, vol. 19, no. 8, pp. 590–592, Apr. 1994.

[23] T. van Leeuwen, D. Faber, and M. Aalders, "Measurement of the axial point spread function in scattering media using single-mode fiber-based optical coherence tomography", *IEEE Journal of Selected Topics in Quantum Electronics*, vol. 9, no. 2, pp. 227–233, Mar. 2003.

[24] J. Xi, Y. Chen, and X. Li, “Characterizing optical properties of nano contrast agents by using cross-referencing OCT imaging”, *Biomedical Optics Express*, vol. 4, no. 6, pp. 842–851, 2013.

[25] L. B. Scaffardi and J. O. Tocho, “Size dependence of refractive index of gold nanoparticles”, *Nanotechnology*, vol. 17, no. 5, pp. 1309–1315, Feb. 2006.

[26] C. G. Granqvist and O. Hunderi, “Optical properties of ultrafine gold particles”, *Physical Review B*, vol. 16, no. 8, pp. 3513–3534, 1977.

[27] P. B. Johnson and R. W. Christy, “Optical constants of the noble metals”, *Physical Review B*, vol. 6, no. 12, pp. 4370–4379, 1972.

[28] H. Inouye, K. Tanaka, I. Tanahashi, and K. Hirao, “Ultrafast dynamics of nonequilibrium electrons in a gold nanoparticle system”, *Physical Review B*, vol. 57, no. 18, pp. 11 334–11 340, 1998.

[29] I. H. Malitson, “Interspecimen comparison of the refractive index of fused silica”, *Journal of the Optical Society of America*, vol. 55, no. 10, pp. 1205–1209, 1965.

[30] M. Lines, “Can the minimum attenuation of fused silica be significantly reduced by small compositional variations? I. Alkali metal dopants”, *Journal of Non-Crystalline Solids*, vol. 171, no. 3, pp. 209–218, 1994.

[31] M. Wandel, “Attenuation in silica-based optical fibers”, Ph.D. dissertation, Tech. Univ. Denmark, 2005.

[32] T. Liu, R. Xu, P. Yu, Z. Wang, and J. Takahara, “Multipole and multimode engineering in Mie resonance-based metastructures”, *Nanophotonics*, vol. 9, no. 5, pp. 1115–1137, 2020.

[33] P. Lu, S. J. Mihailov, D. Coulas, H. Ding, and X. Bao, “Low-loss random fiber gratings made with an fs-IR laser for distributed fiber sensing”, *Journal of Lightwave Technology*, vol. 37, no. 18, pp. 4697–4702, 2019.

[34] C. Daruich De Souza, B. Ribeiro Nogueira, and M. E. C. Rostelato, “Review of the methodologies used in the synthesis gold nanoparticles by chemical reduction”, *Journal of Alloys and Compounds*, vol. 798, pp. 714–740, 2019.

[35] S. Kumar, B. K. Kaushik, R. Singh, N. Chen, Q. S. Yang, X. Zhang, W. Wang, and B. Zhang, “LSPR-based cholesterol biosensor using a tapered optical fiber structure”, *Biomedical Optics Express*, vol. 10, no. 5, pp. 2150–2160, 2019.

[36] G. Frens, “Controlled nucleation for the regulation of the particle size in monodisperse gold suspensions”, *Nature physical science*, vol. 241, no. 105, pp. 20–22, 1973.

[37] H. Xia, S. Bai, J. Hartmann, and D. Wang, “Synthesis of monodisperse quasi-spherical gold nanoparticles in water via silver (I)-assisted citrate reduction”, *Langmuir*, vol. 26, no. 5, pp. 3585–3589, 2010.

[38] T. Lindstrom, E. Garber, D. Edmonson, T. Hawkins, Y. Chen, G. Turri, M. Bass, and J. Ballato, “Spectral engineering of optical fiber preforms through active nanoparticle doping”, *Optical Materials Express*, vol. 2, no. 11, pp. 1520–1528, 2012.

[39] C. Kucera, B. Kokuoz, D. Edmondson, D. Griese, M. Miller, A. James, W. Baker, and J. Ballato, "Designer emission spectra through tailored energy transfer in nanoparticle-doped silica preforms", *Optics Letters*, vol. 34, no. 15, pp. 2339–2341, 2009.

[40] D. Tosi, C. Molardi, and W. Blanc, "Rayleigh scattering characterization of a low-loss MgO-based nanoparticle-doped optical fiber for distributed sensing", *Optics & Laser Technology*, vol. 133, p. 106 523, 2021.

[41] X. Wang, *Matlab code and dataset for light scattering by gold NPs in fused silica*, 4TU.ResearchData. https://doi.org/10.4121/14540823.

5

SPECTRAL CHARACTERISTICS OF GOLD NANOPARTICLE DOPED OPTICAL FIBRE UNDER AXIAL STRAIN

From the results of chapter 3 and chapter 4, it can be seen that doping nanoparticles into the optical fibre could indeed greatly increase the backscattered light signal in the optical fibre, which may be beneficial to the improvement of the signal to noise ratio. But does it still respond to strain change when the nanoparticles are introduced? How does the backscattered light spectrum change under strain? In this chapter, the spectral characteristics of gold nanoparticles doped optical fibre under axial strain are analysed.

Parts of this chapter have been published in Scientific Reports **12**, (2022): 16593.

NANOPARTICLE (NP) doping of optical fibres can be used to increase the intensity of the backscattered light used for distributed strain sensing and has shown the advantages of high precision strain detection and multiplex sensing experimentally. However, the backscatter spectral characteristics of NP-doped optical fibres have not been described even though they are quite different from the spectra from fibre Bragg gratings (FBGs) or commercial single mode fibres. Will the doped NPs change the backscattered light spectral characteristics under axial strain? What are the responsivities of spectral shift under axial strain by NP-doped fibre optic sensors? Before dealing with sub-research question 4 (What is the effect of the sensitivity change and their effect for SHM for material?) which was proposed based on the assumption that NP-doping will only increase the intensity of the backscattered light and the method to analyse the spectral shift can also be implemented to NP-doped fibre optic sensors, the following questions should be answered first. Will the doped NPs change the backscattered light spectral characteristics under axial strain? What are the responsivities of spectral shift under axial strain by NP-doped fibre optic sensors? These questions are related to the main research question: how can the enhancement of light scattering used in distributed fibre optic sensing be an advantage for SHM? Therefore, in this chapter, gold NPs, used as the contrast agent in the optical fibre to increase the intensity of the backscattered light, were investigated from the aspect of their spectra. A single scattering model with Mie theory and an effective refractive index (RI) model were used to evaluate the backscattered light spectra and the Monte Carlo Method was used for seeding NPs.

5.1. INTRODUCTION

The behaviour of the spectra shift under strain for optical fibre and that it is similar to that from fibre Bragg gratings (FBGs) has been demonstrated and has been used for strain sensing since the 1990s [1]. A refractive index (RI) fluctuation in the optical fibre causes this scattered light in the optical fibres [2], [3]. Backscatter reflectometry uses the backscattered light and by using cross-correlation of the spectra before and after strain changes and auto-correlation with spectra before strain change, the wavelength shift can be obtained [4]. This wavelength shift can then be used to obtain strain or temperature information based on the responsivity of the sensors. For a commercial optical fibre, Rayleigh scattering is the major component for light scattering. This Rayleigh scattering based distributed fibre optic sensing has the advantages of long distance sensing, low weight, immunity to electromagnetic interference etc. and has been widely used in a variety of fields, such as aerospace engineering [5] and civil engineering [6] for structural health monitoring (SHM).

Rayleigh scattering based distributed fibre optic sensing usually uses commercial communication optical fibres as the sensing components. The optical fibres used for communication are generally low loss and low dispersion fibres in the communication wavelength bands. One reason for using communication optical fibres as the sensing fibres is that they can achieve long distance sensing, for example several kilometres, due to their low attenuation (about 0.2 dB/km @1550 nm). Meanwhile, they are also relatively cheap due to mass production for the communication industry. Therefore, they are often used as the sensors for distributed fibre optic sensing.

However, the backscattered light signal in the communication optical fibre is generally very low ($-100\,\mathrm{dB/mm}$ for single mode fibre (SMF) [7]), which has become a limitation of the Rayleigh scattering based technique [8] for some applications. For SHM of aircraft structures, only key parts for example the areas close to the rivet holes usually need to be monitored and the required distance is not necessarily very long but high spatial precision is required. In this case long distance sensing may not be an advantage. To address this, it is necessary to enhance the local scattered light signal near the key parts of the aircraft structures to improve the signal-to-noise ratio to get a better monitoring of the key parts.

In order to increase the intensity of the backscattered light signal in the optical fibres, several methods have been proposed. The ultraviolet (UV) light irradiation method can greatly increase the intensity of the scattered signal by about 20 dB, which may be due to the numerical aperture increase after exposure [8]. This method has also been used in surgery applications [9]. Femtosecond lasers can generate microstructures in the core of the optical fibres [10], [11]. The random microstructures improve the backscattered signal dramatically which also improves the signal to noise ratio for distributed fibre optic sensing. Both of these methods are based on laser damage of the optical fibres.

NPs have been widely used to pump the light signal in optical fibres [12], [13]. The RI difference of the NPs to the core of the optical fibre will also cause the backscattered light in the optical fibre. Therefore, doping NPs into the core of the fibres is an approach for achieving backscattered light enhancement. In addition, as the size of the NPs increases, the Rayleigh scattering in the optical fibre will tend to Mie scattering when the size of the NP is comparable with the incident light [14] and this causes a dramatic light intensity increase. For this reason, in recent years, NP-doped optical fibres have been investigated to overcome the low scattering limitation of the optical fibre and it has become an active research field.

Several oxide or metallic materials have been chosen as the scattering agents to increase the scattered light. As an oxide material, magnesium oxide (MgO) has been studied extensively by researchers because MgO has low attenuation and also has the ability to increase the backscattered light in the optical fibres, which is required for long distance enhanced sensing [15]. By changing the temperature during manufacturing of optical fibre containing MgO, high scattering MgO-doped optical fibre has been achieved [16]. The relationship between the temperature and the backscattered light spectra wavelength shift has been studied experimentally. There are also some applications with the MgO-doped optical fibres, for example multiplexed sensing [17].

Gold is one of the metallic materials that attracts interest in recent years especially for bio-imaging enhancement because of its highly scattering characteristics [18], [19]. Gold NP doped optical fibres have the potential to increase the scattered light dramatically within a short distance (several centimetres to metres), so they may be suitable for short distance strain sensing for key areas which need to be monitored [20], [21]. In experiment, zirconia-coated gold doped optical fibre has been investigated and showed an increase of stability for high temperature sensing (800°C) [22].

However, there are few theoretical studies on the characteristics of the scattering spectra of NP doped optical fibres. A theoretical investigation is important to guide the engineering design of NP doped fibre sensors. In this work, the characteristics of NP doped optical fibres will be investigated from the characteristics of their backscattering spectra. First, the characteristic of the spectra shift under strain will be analysed theoretically and then compared with the FBGs and commercial fibres cases. The nonlinearity between strain and wavelength shift caused by the introduction of NPs is analysed. Taking gold NP optical fibre as an example, the random interference characteristics of the scattering spectra of gold NPs of different sizes and volume ratios are studied in the wavenumber domain.

5.2. METHOD

Figure 5.1 shows a simplified structure of the experimental setup of a typical distributed fibre optic sensing based on optical frequency domain reflectometry. Light

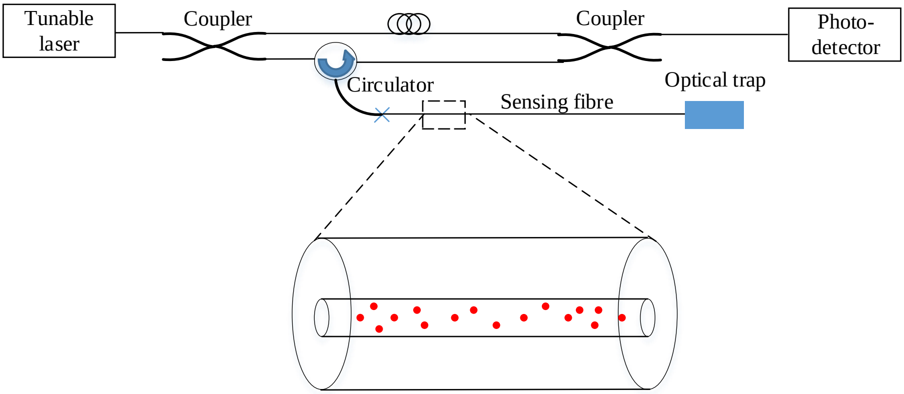

Figure 5.1: Experimental setup. The dashed rectangular zone shows a gauge length which has been enlarged. Red dots indicate randomly positioned gold NPs in the core of the optical fibre. The core of the optical fibre is surrounded by outer layers.

emitted by a tunable laser is coupled into a Mach-Zehnder interferometer. One part of the interferometer includes a sensing fibre containing NPs inside of the core of the optical fibre. The backscattered light from the NPs in the sensing fibre will interfere with the light transmitted in the reference arm, which will then be detected by a photodetector. The light backscattered at different positions along the optical fibre will generate a beat signal with the reference signal which can be used for local strain detection with millimetre resolution. By demodulating the time-series signal detected by the photodetector with Fourier transform to obtain spectra information and comparing the spectra obtained before and after strain change, the strain can be obtained. Generally, the optical setup includes an additional interferometer to compensate for the non-linearity of the tunable laser and there is also a polarized beam splitter before the photodetectors to compensate for the polarization changes in the optical fibre. For simplification, Figure 5.1 only shows the basic components for the strain detection.

In the simulation procedure, 100 nm, 200 nm, 300 nm and 400 nm size spherical gold NPs were chosen as the typical large size gold NPs used for simulations. The volume ratios chosen were from about 10^{-10} to about 10^{-2} with different gauge lengths (0.1069 cm, 0.5345 cm, 1.0690 cm, and 2.1379 cm which corresponds to 2000 times, 10000 times, 20000 times and 40000 times Λ for a period length of a FBGs at effective RI of 1.45). The simulation procedure can be described as: 1. Choosing a specific size of gold NP which is used for simulation; 2. Choosing a specific gauge length; 3. Seeding an integer number of NPs in the given gauge length. The seeding process is a Monte Carlo seeding and the spatial distribution of the NPs follows a uniform distribution within the gauge length; 4. The corresponding volume ratio of gold NPs to the optical fibre and the concentration of the gold NPs can be calculated. Applying the single scattering assumption in the gauge lengths ($l < 1/cC_{ext}$) where c is the concentration of the NPs in the core of the fibre and C_{ext} is the extinction cross section for the NP, the maximum volume ratios can be obtained; 5. The backscattered light signal can be obtained in the wavelength domain by calculating the square of Equation 5.15. K is approximated as 1 in the simulation; 6. By Fourier transform, the signal was transferred to the wavenumber domain to compare the spectral density characteristics with a threshold of $1/e$ of the maximum. The wavenumber at the threshold was recorded as the parameter to characterise the fluctuation of the spectra. The period number can be obtained by the wavelength range multiplying the wavenumber at the threshold.

5.3. THEORY

A schematic of the theoretical model is shown in Figure 5.2. The incident light from the tunable laser propagates along the sensing fibre. The incident light will be scattered and absorbed by the gold NPs in the core of the optical fibre. The transmitted light and forward and backward scattered light that can meet the requirements for transmitting in the optical fibre will propagate in the forward and backward directions. The backscattered light and the forward scattered light can be scattered many times. The total collected backscattered light is a combination of the single backscattering and multiple backscattering. For the sensing fibre, it has been divided into n gauges. For simplification, the first, the second, the third, and the nth gauges are shown in the figure. Each gauge is used as a strain gauge for strain detection. When the axial strain changes, the relative positions of the NPs will change and the RI of the optical fibre will also change. Then, the backscattered light spectrum will shift. By demodulating the spectral shift, the strain values can be obtained.

To determine the backscattered spectra in the sensing path and to avoid time-consuming calculations, some assumptions are made. The NPs inside of the core of the optical fibres are assumed to be homogeneous spherical NPs with low volume ratios which meet the single scattering approximation as will be shown later, there-

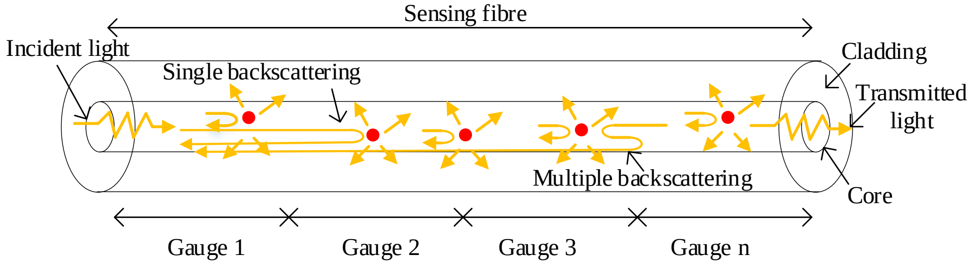

Figure 5.2: A schematic of the theoretical model. The red dots show the gold nanoparticles in the core of the sensing fibre in random positions.

fore the light scattered by the NPs can be calculated by Mie theory and only single backscattered light needs to be considered. A random distribution of the NPs in the optical fibre is assumed and the positions of the NPs were obtained by the Monte Carlo Method for seeding the NPs. In this case, the core of the optical fibre consists of two materials, fused silica fibre and gold NPs, so the RI of the core of the optical fibre needs to use the effective RI. In additon, for the backscattered light, only the light which is within the aperture angle can transmit backwards in the optical fibre. Therefore, the backscattered light in the fibre in a sensing gauge length can be expressed as:

$$E_s = \sum_{i=1}^{N} \bar{\bar{r}}(l_i) E_i(l_i) \exp j(kn_{eff} l_i), \tag{5.1}$$

where, E_s is the electrical field of the scattered light at the beginning of the gauge length, E_i is the electrical field of the transmitted light at position l_i, N is the total number of the NPs in the gauge length. $\bar{\bar{r}}(l_i)$ is the complex reflectively of each NP at the i^{th} NP's position l_i, j is the imaginary unit and n_{eff} is the effective RI of the core of the fibre. $k = 2\pi/\lambda$ is the angular wavenumber in vaccum and λ is the wavelength in vaccum. The electrical field of the transmission light at position l_i can be expressed as:

$$E_i = E_0 \exp(jkn_{eff} l_i), \tag{5.2}$$

where, E_0 is the electrical field of the incident light. The complex reflectively of each NP can be expressed as:

$$\bar{\bar{r}}(l_i) = r_i \exp j\phi_i \approx \frac{E_s(l_i)\sqrt{\Omega r^2}}{E_i(l_i)\sqrt{\pi R^2}} = \frac{\sqrt{\Omega} S_2(\pi)}{-jkn_{eff}\sqrt{\pi} R}, \tag{5.3}$$

where, Ω is the solid angle which corresponds to the aperture angle, r is the distance to the centre of each NP, R is the radius of the core region of the fibre, and $S_2(\pi)$ is the scattering parameter at a backward angle π. Then, the amplitude and phase of the complex reflectively can be expressed as:

$$r_i = |\overline{\overline{r}}(l_i)| \tag{5.4}$$

and

$$\phi_i = \angle\overline{\overline{r}}(l_i). \tag{5.5}$$

The relationship between the incident light and the scattered light can be expressed as:

$$\begin{bmatrix} E_{\parallel s} \\ E_{\perp s} \end{bmatrix} = \frac{\exp jkn_{eff}(r-z)}{-jkn_{eff}r} \begin{bmatrix} S_2(\mu) & 0 \\ 0 & S_1(\mu) \end{bmatrix} \begin{bmatrix} E_{\parallel i} \\ E_{\perp i} \end{bmatrix}, \tag{5.6}$$

where, $E_{\parallel i}$ and $E_{\perp i}$ are the two orthogonal components of the incident light, $E_{\parallel s}$ and $E_{\perp s}$ are the two orthogonal components of the scattered light with angle μ, $\mu = \cos\theta$ and $\mu = -1$ for backward scattering. The transmitted light in the optical fibre is assumed to be polarised light for simplification. For a more general case, the light can be decomposed to a combination of the parallel component and the perpendicular component but this was not taken into consideration in this chapter.

The van de Hulst approximation has been used for calculation of the effective RI of gold NP-doped MoO_3 film [23] when the system is considered as a dilute turbid system. When the single scattering approximation is considered, the volume ratio of gold NP in the optical fibre is low. Then, it is assumed that the effective RI of NP-doped optical fibre can be expressed according to the van de Hulst approximation for low volume ratio doping based on the equation from Gesuri Morales-Luna and Michael Morales-Luna [23] as:

$$n_{eff} = n_m\left(1 + j\frac{3fS(0)}{2x^3}\right), \tag{5.7}$$

where, n_m is the RI of the optical fibre (fused silica), f is the volume ratio of the NPs in the core of optical fibre, $S(0)$ is the forward scattering amplitude which can be calculated by Mie theory [14] and the RI of gold used for calculation is based on the size dependant RI of gold [21], [24]. x is the size parameter of the NP in the optical fibre.

Then, the electrical field for backscattered light can be expressed as:

$$E_s = \sum_{i=1}^{N} E_0 A_i \exp j\left(\frac{4\pi n_m l_i}{\lambda}\left(1 - \frac{3f\Im S(0)}{2x^3}\right) + \phi_i\right), \tag{5.8}$$

where, $A_i = r_i \exp\left(-6\pi f n_m \Re S(0) l_i / \lambda x^3\right)$.

If the NP inside the optical fibre can be assumed to be an isotropic material and the axial strain of the optical fibre changes, the volume of the NP may change from sphere to spheroid. According to the geometry, the volume ratio after strain change can be expressed as:

$$f' = \frac{(1+\varepsilon_{gold})(1+\gamma_{gold}\varepsilon_{gold})^2}{(1+\varepsilon_{fibre})(1+\gamma_{fibre}\varepsilon_{fibre})^2} f, \tag{5.9}$$

where, ε_{gold} is the axial strain of the gold NPs, ε_{fibre} is the axial strain of the optical fibre and γ_{gold} is the ratio of transverse strain to axial strain of the gold NPs, γ_{fibre} is the ratio of transverse strain to axial strain of the optical fibre, f is the volume ratio of gold NPs to the optical fibre before strain change and f' is the volume ratio of gold NPs to the optical fibre before strain change.

The relative axial strain changes between the NP and the optical fibre (α) is defined as $\alpha = \varepsilon_{gold}/\varepsilon_{fibre}$. Then, the electrical field of the scattered light in the sensing fibre can be expressed as:

$$E_s(\varepsilon_{fibre}) = \sum_{i=1}^{N} E_0 A_i \exp j\left(\frac{4\pi n'_m(\varepsilon_{fibre})\, l'_i(\varepsilon_{fibre})}{\lambda}\left(1-\frac{3f\Im S'(0)}{2x'^3}\right)+\phi_i\right), \tag{5.10}$$

where,

$$n'_m(\varepsilon_{fibre}) = n_m(1+\eta_m\varepsilon_{fibre}), \tag{5.11}$$

and

$$l'_i(\varepsilon_{fibre}) = l_i(1+\varepsilon_{fibre}). \tag{5.12}$$

The size parameter for the spherical NP is defined as $x = 2\pi r_{NP}/\lambda$, where r_{NP} is the radius of the sphere. According to the geometry change of the NP under strain, the geometric cross section will be expanded or compressed in the case that the axial strain is negative (compression) or positive (tension). Therefore, the size parameter of the NP under strain can be expressed as:

$$x' = \frac{n'_m}{n_m}x(1+\alpha\varepsilon_{fibre}). \tag{5.13}$$

If the forward scattering amplitude $S(0)$ is assumed to follow a linear relationship under strain, then the forward scattering amplitude $S'(0)$ can be expressed as:

$$\Im S'(0) = \Im S(0)(1+\gamma_S\varepsilon_{fibre}). \tag{5.14}$$

Therefore,

$$E_s(\varepsilon_{fibre}) \approx \sum_{i=1}^{N} E_0 A_i \exp j\left(\frac{4\pi n_m l_i}{\lambda}K(1+\varepsilon_{fibre})(1+\eta_m\varepsilon_{fibre})+\phi_i\right). \tag{5.15}$$

Using a first order Taylor expression at a strain value of zero,

$$K \approx 1-\frac{3f\Im S(0)}{2x^3}K', \tag{5.16}$$

where,

$$K' = 1+(\alpha-\alpha\gamma_{gold}+\gamma_S-1-2\gamma_{fibre}-3\eta_m)\varepsilon_{fibre}. \tag{5.17}$$

Therefore, the characteristic peaks also change their wavelengths according to

$$\lambda'_{NP} = \lambda_{NP}K(1+\varepsilon_{fibre})(1+\eta_m\varepsilon_{fibre}) \approx \lambda K(1+\varepsilon_{fibre}+\eta_m\varepsilon_{fibre}) \tag{5.18}$$

Equation 5.18 is similar to the expression for a FBG, which can be expressed as $\lambda_B = 2n\Lambda$, where, n is the effective RI of the FBG and Λ is the grating period. When the strain changes, Λ and n will change and the expression for the FBG under strain can be expressed as

$$\lambda_B' = \lambda_B(1+\varepsilon_{fibre})(1+\eta_m\varepsilon_{fibre}) \approx \lambda_B(1+\varepsilon_{fibre}+\eta_m\varepsilon_{fibre}), \tag{5.19}$$

where, λ_B' and λ_B are the Bragg wavelength of the FBG with and without strain change.

For Rayleigh scattering based distributed fibre optic sensing, the wavelengths under strain can be expressed as [25]

$$\lambda_R' = \lambda_R(1+\varepsilon_{fibre}+\eta_m\varepsilon_{fibre}) \tag{5.20}$$

$$\eta_m = -\frac{p_{12}-v(p_{11}+p_{12})}{2}n^2 \tag{5.21}$$

where, $p_{11} = 0.113$, $p_{12} = 0.252$, v is the Poisson's ratio of optical fibre and $v = 0.17$. If the RI is set at 1.45, then $\eta_m = -0.1997$.

Table 5.1: The expressions comparison among different types of fibres

Type	Expression
fibre Bragg grating	$\lambda_B' = \lambda_B(1+\varepsilon_{fibre}+\eta_m\varepsilon_{fibre})$
distributed sensing based on Rayleigh scattering	$\lambda_R' = \lambda_R(1+\varepsilon_{fibre}+\eta_m\varepsilon_{fibre})$
NP doped optical fibre	$\lambda_{NP}' = K\lambda_{NP}(1+\varepsilon_{fibre}+\eta_m\varepsilon_{fibre})$

In order to make a comparison between the Bragg wavelength shift of a FBG, the wavelength shift of distributed fibre optic sensing based on Rayleigh scattering and the spectral wavelength shift in the NP doped optical fibre, the expressions are summarised in Table 5.1. It can be seen from Table 5.1 that for an FBG, distributed sensing based on Rayleigh scattering and a NP doped optical fibre, the wavelength shift expressions are in similar forms so now the sensitivities can be easily compared. However, for Bragg grating there is a Bragg wavelength while for the distributed sensing based on Rayleigh scattering and NP doped optical fibre there are random peaks. In addition, for a NP doped optical fibre, the wavelength shift is also influenced by a factor of K which is a nonlinear contribution to the responsivity caused by NP doping.

5.4. RESULTS AND DISCUSSION

Light could be scattered multiple times in the optical fibre by the NPs, but the higher order scattering (scattered more than one time) shows a low light intensity. In order to show the scattered light intensity received at the incident port which is within the single scattering length ($z = 1/cC_{ext}$, where c is the concentration of the NPs and C_{ext} is the extinction cross section of the NP), the flowchart shown in Figure 5.3 is used for this calculation. The flowchart begins by checking if the order of the scattering

(i) is larger than the set highest scattering order (i_H). The results of the intensities of different scattering order are shown in Figure 5.4. The incident light power is set to 1 mW.

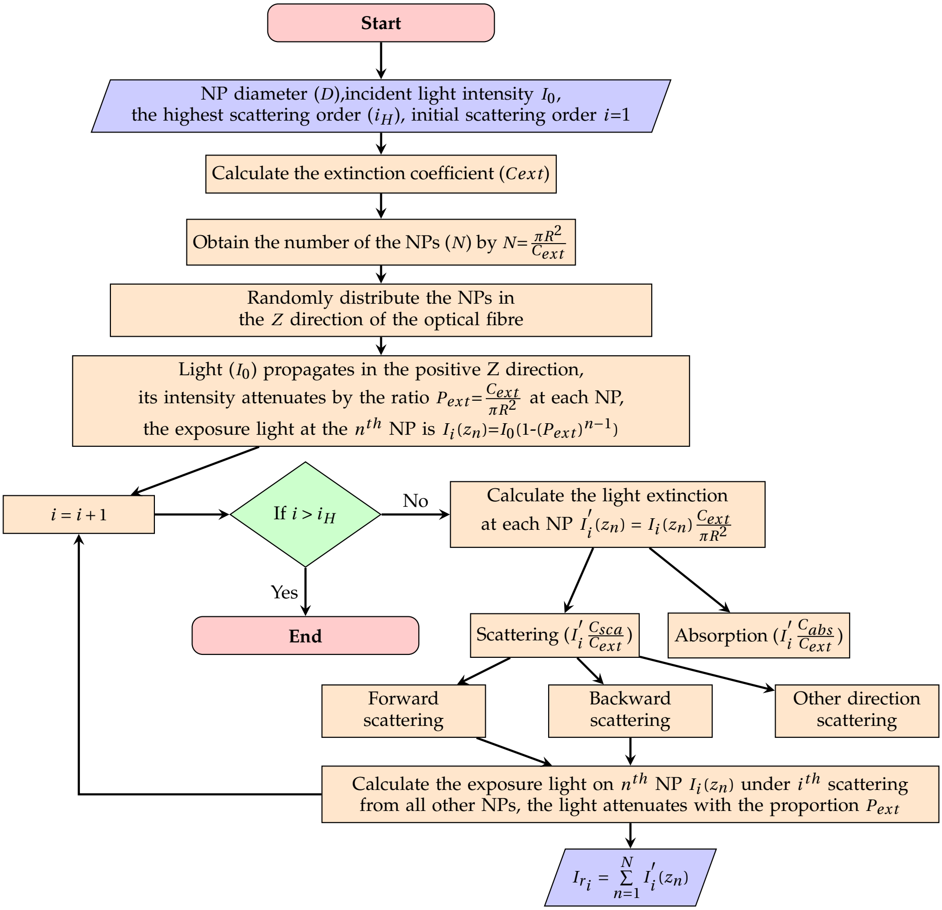

Figure 5.3: Flowchart of up to N^{th} order scattering received from an optical fibre input port

Single scattering components are much larger than the higher order scattering shown in Figure 5.4. The intensities of twice scattering (scattering order 2) are 0.0505 %, 0.3205 %, 0.1962 %, 0.2136 %, 0.1984 % and 0.1697 % compared with single scattering (scattering order 1) for 100 nm, 150 nm, 200 nm, 250 nm, 300 nm, 350 nm and 400 nm size gold NPs respectively. It can be seen that the components for multiple scattering is low. Therefore, only considering the single scattering is suitable for the calculation and can reduce the calculation time.

The difference between the expressions of the spectral shift of NP doped optical fibre and FBG or distributed fibre optic sensing based on Rayleigh scattering is that there is an additional nonlinear factor of K (see Table 5.1). It can be seen from Equations 5.16 and 5.17 that the coefficient before K' determines the deviation from

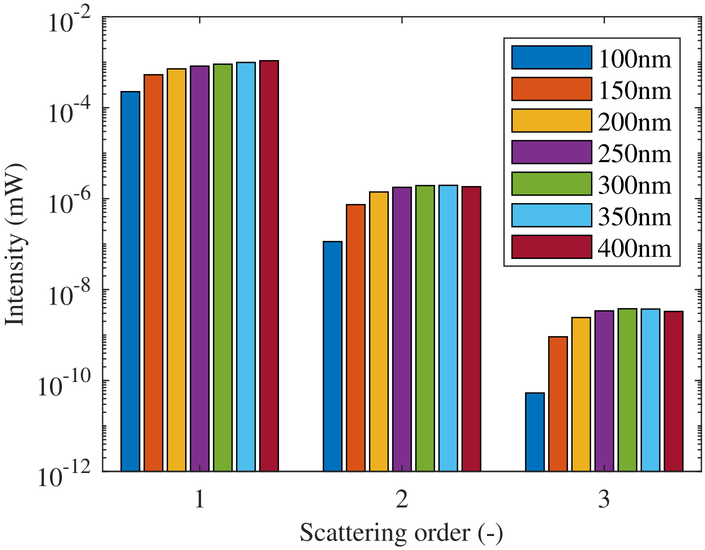

Figure 5.4: Light intensity under different scattering orders (1 mW incident light)

the other two cases and K' varies with γ_S and η_m under different wavelengths. α, γ_{gold}, γ_{fibre} are determined by the mechanical properties of the materials. For the optical fibre with 100 nm size gold NPs with $\alpha = 0.92$, $\gamma_{fibre} = -0.17$, $\gamma_{gold} = -0.40$, γ_S can be calculated and is shown in Figure 5.5 (a). If η_m is assumed to be a constant, then K' can be calculated and is shown in Figure 5.5. Although K' varies a lot in the wavelength range, the strain applied to the optical fibre is a small strain (less than several $0.001\,\epsilon$). Therefore, K' has a negligible effect on K. The coeffiecent before K' is shown in Figure 5.5 (b) and it is quite small when it multiplies a low volume ratio (f). If $f = 0.001$ is used, it is a large volume ratio so the single scattering assumption maybe not effective. Even for this case, the parameter K is almost at 1 with small variation (less than 0.2 %) within the spectra range from 400 nm to 1600 nm and the NP diameter range from 10 nm to 400 nm, so the nonlinear property of the nonlinear factor K is quite small when the volume ratio of the NPs in the optical fibre is small which is in this case $K \approx 1$. Therefore, for the following case study of different sizes and volume ratios of NPs in different gauge lengths, K is set to 1 for simplification. Then, the characteristic spectra were obtained using Equation 5.15. The wavelength range was from 1545 nm to 1555 nm and the wavelength resolution used for simulation was 1 pm. The strain was set at 100 $\mu\epsilon$. The gold NPs were seeded in the specific gauge lengths with their concentrations.

Figure 5.6 shows two cases of different size gold NPs with different volume ratio in different gauge lengths. Note: the spectra have been normalised by the maximum values. Figure 5.6 (a) shows the case of 200 nm gold NP with 100 NPs in 1.0690 cm gauge length. In this case, the single scattering length is 41.4476 cm and the concentration of gold NP is 1.3198×10^8 mL^{-1}. The gauge length is smaller than the

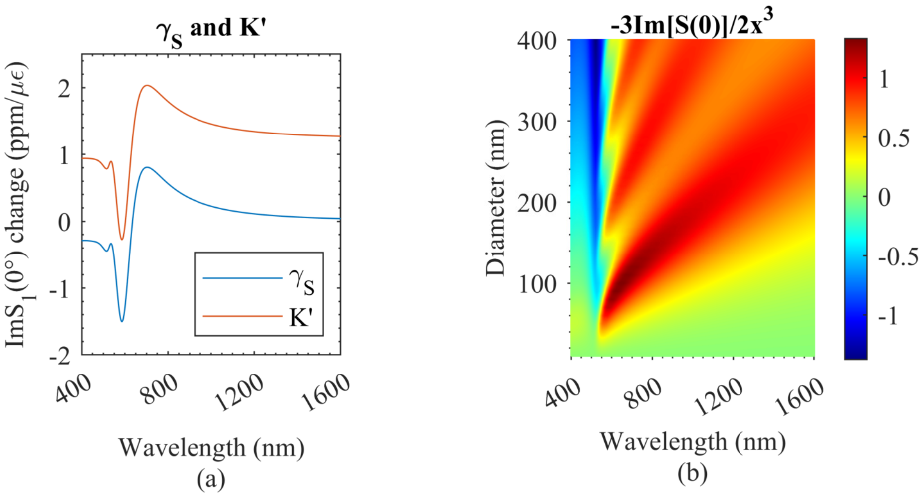

Figure 5.5: The nonlinear factors. (a) γ_S and K'; (b) The coefficient before K'.

single scattering length. Therefore, the major components of the light scattered in the gauge length is single scattered light. Figure 5.6 (b) shows the case of 400 nm gold NP with 100 NPs in 0.1069 cm gauge length, whose single scattering length is 0.2021 cm and for a concentration of gold NP is $1.3198 \times 10^9\,\mathrm{mL}^{-1}$. The red lines shown in Figure 5.6 (a) and 5.6 (b) are the spectra under strain 0. The blue lines are the spectra under 100 $\mu\epsilon$. It can be seen that there is a red shift of the spectra under 100 $\mu\epsilon$. The redshift values are about 124 pm for both cases. To compare the original spectra and the spectra under the spectral shift, the spectra with black lines show the spectra with −124 pm shift. The spectra after the translational movement match the original spectra well in Figure 5.6 (a) and 5.6 (b). The shift directions are labelled with black arrows. There are slightly more differences between the spectra of red lines and black lines. One reason for the differences is that the intensity of the backscattered light from the NPs is influenced by the RI change of the optical fibre.

Comparing Figure 5.6 (a) and 5.6 (b), it can be seen that the density of the spectra are different. There are more spectral fluctuations within the wavelength range for Figure 5.6 (a) than the spectral fluctuation in Figure 5.6 (b). The spectra fluctuation numbers are different for different sizes of NPs, volume ratios and gauge lengths.

In order to evaluate the spectral density quantitatively, the spectra were transferred to the wavenumber domain (spatial frequency) by Fourier transform and then by setting a threshold to obtain a period number for evaluating the spectral density. The period number was defined as the threshold spatial frequency multiplied the wavelength range, so it is a dimensionless value to evaluate the spectra fluctuation property.

The embedded graphs in Figure 5.6 show the results of the spectra after Fourier transform under strain 0 for evaluating the spectral density. The spectra with averaged intensity value of 0 in the wavelength domain were transferred to the wavenum-

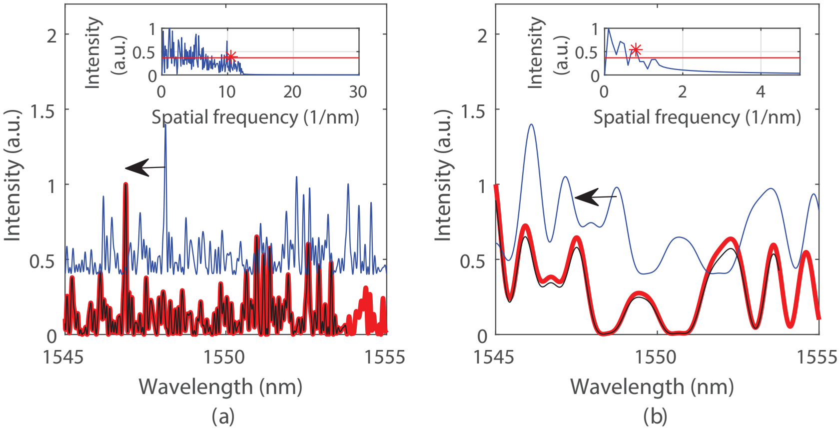

Figure 5.6: The spectra and the spatial frequency information under 100 µε. (a) A case for 200 nm gold NP; (b) A case for 400 nm gold NP.

ber domain. The threshold of $1/e$ was set to evaluate the spectra fluctuation property. The red stars are the first points that meet the requirement of being above the threshold from the high space-frequency side. The period number of the spectra in Figure 5.6 (a) is larger than the spectra in Figure 5.6 (b) which is consistent with the results seen from the wavelength domain directly.

The period numbers may be influenced by the size of the NPs, the volume ratio of the NPs in the optical fibre and the gauge lengths. The influence of the period number for these parameters was analyzed. Figure 5.7 shows the period numbers for different imaginary parts of the effective RI. The different imaginary parts of the effective RI correspond to different volume ratios of NPs. One reason for choosing imaginary parts of the effective RI is that the imaginary parts of the effective RI not only consist of the volume ratio but also consist of the property of the materials, for example absorbing NP materials and non-absorbing NP materials. Therefore, the imaginary part of the effective RI is a more universal parameter compared with volume ratio. As shown in Figure 5.7, the period number increases when the gauge length increases in the lower imaginary part of the effective RI range (less than about 2×10^{-6}). When the imaginary part of the effective RI range is above this range, the period number shrinks to low values. This indicates that the gauge length has a high influence on the spectra fluctuation and that the imaginary part of the effective RI adjusts the period number for high doping concentrations. The size of the NPs shows a low influence on the period number for these four different sizes of NPs, which may indicate the gauge length and the imaginary part of the effective RI are the major factors for period number and for the characteristic of the fluctuation density of the backscattering spectra. However, the single scattering restriction limits the doping concentration to low levels, see the maximum values of the imaginary part of effective RI shown in a black dash rectangular frame in Figure 5.7. Under the single scattering restriction, the period number shows the independence of the size of the NPs and the period number is only influenced by the gauge lengths. Longer gauge lengths show larger period values.

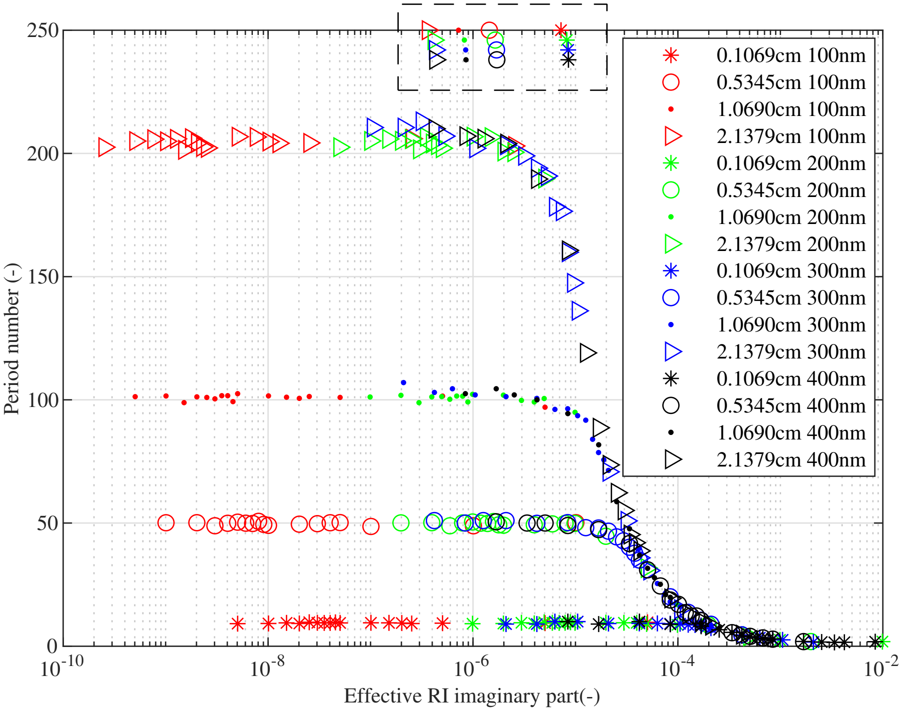

Figure 5.7: Period number with volume ratio ratios for different sizes of NPs (100 nm in red, 200 nm in green, 300 nm in blue and 400 nm in black) with different gauge lengths (0.1069 cm with star, 0.5345 cm with circle, 1.0690 cm with triangle and 2.1379 cm with point). The patterns in the dash rectangular frame are only used to show the maximum values of the imaginary part of effective RI based on the single scattering restriction.

The intensities of the spectra were normalised in the previous analysis. The intensity of the backscattered light is also a characteristic of the spectra. In order to evaluate the backscattered light intensity, Figure 5.8 was plotted for different volume ratios of gold NPs. The reason for choosing volume ratio as the variable is that the results can be compared with the results in chapter 4. Because of the random seeding of the NPs in the optical fibre, the intensity of the spectra is not a constant. Therefore, the results are plotted with error bars. The error bar shows the maximum intensities and minimum intensities by 100 times averaging by Monte Carlo seeding in a gauge length of 0.1069 cm optical fibre. The blue line, red line, yellow line and pink line show the maximum volume ratios for single scattering for 100 nm, 200 nm, 300 nm and 400 nm respectively. Although larger size NPs generally have a higher intensity for backscattering, the single scattering requirement restricts the volume ratio. Therefore, it can be seen that 200 nm size gold NPs have a similar backscatter-

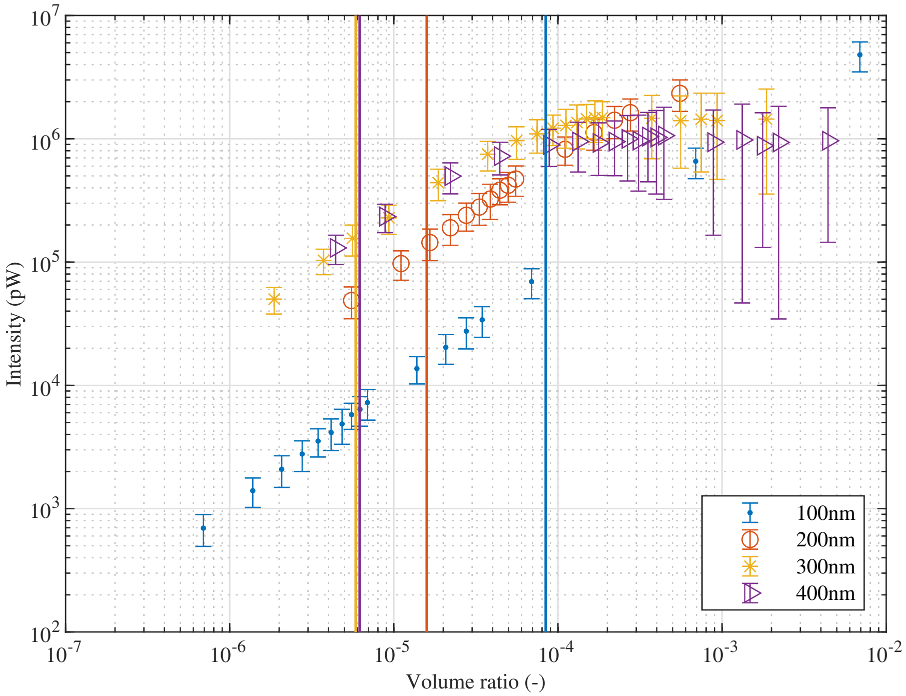

Figure 5.8: Intensity of backscattered light under different volume ratios of the NPs with 0.1069 cm gauge length. The blue, red, orange and purple lines show the maximum volume ratios in the case of single scattering for 100 nm, 200 nm, 300 nm and 400 nm respectively. (Incident light power 1 mW)

ing intensity compared with larger sizes (300 nm and 400 nm sizes gold NPs) cases, which is consistent with the previous work in chapter 4. It can also be seen that although increasing the volume ratio over the single scattering limitation may increase the backscattered light, the increase is reduced for high volume ratios. This may be caused by the absorbing property of the gold. High concentrations of gold NPs may shorten the effective gauge length and only the scattered light in the front of the gauge length would have an influence on the backscattered light spectra.

Doping gold NPs into the optical fibre has an influence on the light dispersion in the optical fibre. The RI of fused silica [26] was used as the material for optical fibre. By doping gold NPs, the dispersion was tuned. The group velocity dispersion ($D_\lambda = -\frac{\lambda}{c}\frac{\mathrm{d}^2\Re n_{eff}}{\mathrm{d}\lambda^2}$) was used to evaluate the material dispersion, where c is the velocity of light in a vacuum and $\Re n_{eff}$ is the real part of the effective RI of optical fibre. Then, the material dispersion of gold NP-doped optical fibre is shown in Figure 5.9.

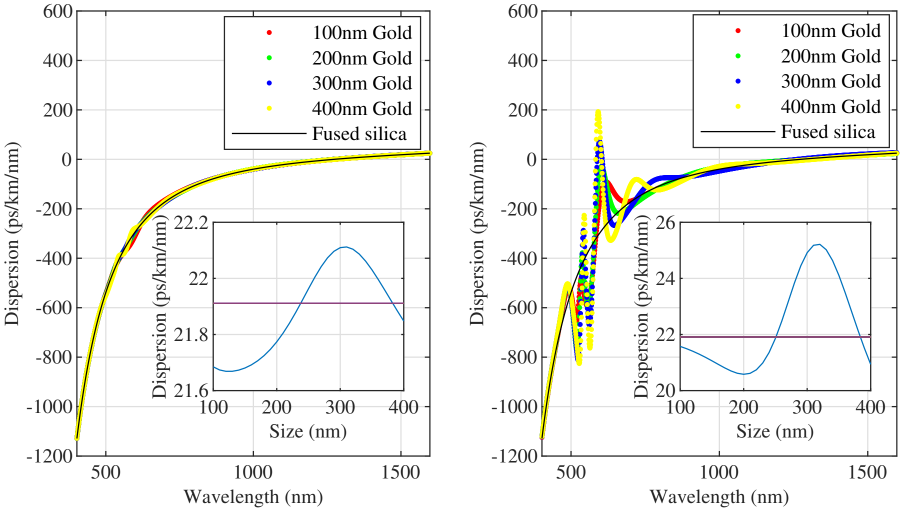

(a)

(b)

Figure 5.9: The material dispersion of gold NP-doped optical fibres. (a) The cases of material dispersion of 1 cm length gold NP-doped optical fibres with the maximum concentrations for single scattering restriction. The red dots show the case for 100 nm size gold NPs. The green dots show the case for 200 nm size gold NPs. The blue dots show the case for 300 nm size gold NPs. The yellow dots show the case for 400 nm size gold NPs. The black lines show a reference of material dispersion of fused silica. The embedded graph shows the dispersion of 1 cm length gold NP-doped optical fibres with the maximum concentrations for single scattering restriction for different sizes of gold NPs from 100 nm to 400 nm at 1550 nm incident light in blue lines. The purple lines show the dispersion of fused silica at 1550 nm. (b) The cases of material dispersion of 1 cm length gold NP-doped optical fibres with a fixed volume ratio of 1×10^{-4}. The red, green, blue, yellow dots show the case for 100 nm, 200 nm, 300 nm and 400 nm gold respectively. The black lines show the dispersion of fused silica. The embedded graph shows the dispersion of 1 cm length gold NP-doped optical fibres with volume ratio of 1×10^{-4} for different sizes of gold NPs at 1550 nm incident light in blue lines. The purple lines show the dispersion of fused silica at 1550 nm.

Figure 5.9 (a) shows the cases of material dispersion of 1 cm length gold NP-doped optical fibres with the maximum concentrations for single scattering restriction at 1550 nm. The black lines show the case of fused silica (without doping NPs) as a reference. The red, green, blue and yellow dots show the cases for 100 nm, 200 nm, 300 nm and 400 nm gold NPs respectively. It can be seen that dispersion deviations occur between the dispersion curve of fused silica and NP-doped fibres within the spectral range from 400 nm to 1600 nm in Figure 5.9 (a). An embedded graph shows the cases of the material dispersion with different sizes of gold NPs (from 100 nm to 400 nm with an interval of 10 nm) at 1550 nm incident light in blue lines. The purple line shows the dispersion of fused silica as a reference. The dispersion of the material was tuned by doping NPs.

Figure 5.9 (b) shows the cases of material dispersion of 1 cm length gold NP-doped optical fibres with a fixed higher volume ratio (1×10^{-4}). It can be seen that in the visible light range, the dispersion has been tuned dramatically and for some wavelengths the dispersion can be zero. It indicates that zero dispersion may be achieved by doping gold NPs with specific sizes and concentrations for some wavelengths. The embedded graph in Figure 5.9 (b) shows the cases of the material dispersion with different sizes of gold NPs at 1550 nm incident light in blue lines. The purple line shows the dispersion of fused silica. It can be seen the shape of the dispersion curve has been tuned intensely compared with the cases in the embedded graph in Figure 5.9 (a) due to the increasing of the concentration of NPs.

5.5. CONCLUSION

NP doped optical fibres have similar spectral shift behaviour under strain compared with FBGs or distributed strain sensing based on Rayleigh scattering under the single scattering restriction, which means that the backscattered light spectra still respond to the axial strain linearly with spectral shift with a same responsivity (about $1.24\,\mathrm{pm}/\mu\varepsilon$). This make it an advantage for SHM because these new NP-doped optical fibres sensors are compatible with some commercial interrogators (for example LUNA system). Moreover, the characteristics of the spectra (spectra fluctuation and backscattered intensity) were investigated and some interesting findings were obtained. For example, the imaginary part of the effective RI has a high influence on the period number of the spectra. Gauge length also showed a correlation to the period number. However, the size of the NPs did not show a relationship with the period number from 100 nm size to 400 nm size gold NPs range under single scattering restriction. Although increasing the volume ratio further may increase the backscattered light intensity, the absorbing property of the material restricts the tendency of the intensity to increase. These theoretical results may promote the future design in engineering of NP doped fibre sensors.

5.6. DATA AVAILABILITY

The dataset for the results in the chapter is available in the 4TU.ResearchData, Ref. [27] (https://doi.org/10.4121/20013470).

5.7. APPENDIX

Figure 5.10 shows the minimum doping cases for different strain gauges (1 mm, 5 mm, 10 mm and 20 mm in red, blue, green, black lines respectively.). There are only 2 NPs in a strain gauge. Figure 5.10 (a) shows the 3 dB light loss length versus the diameter of gold NPs. This loss was defined in chapter 4. Figure 5.10 (b) shows the corresponding volume ratios versus the diameter of gold NPs. Figure 5.10 (c) shows the corresponding concentrations versus the diameter of gold NPs.

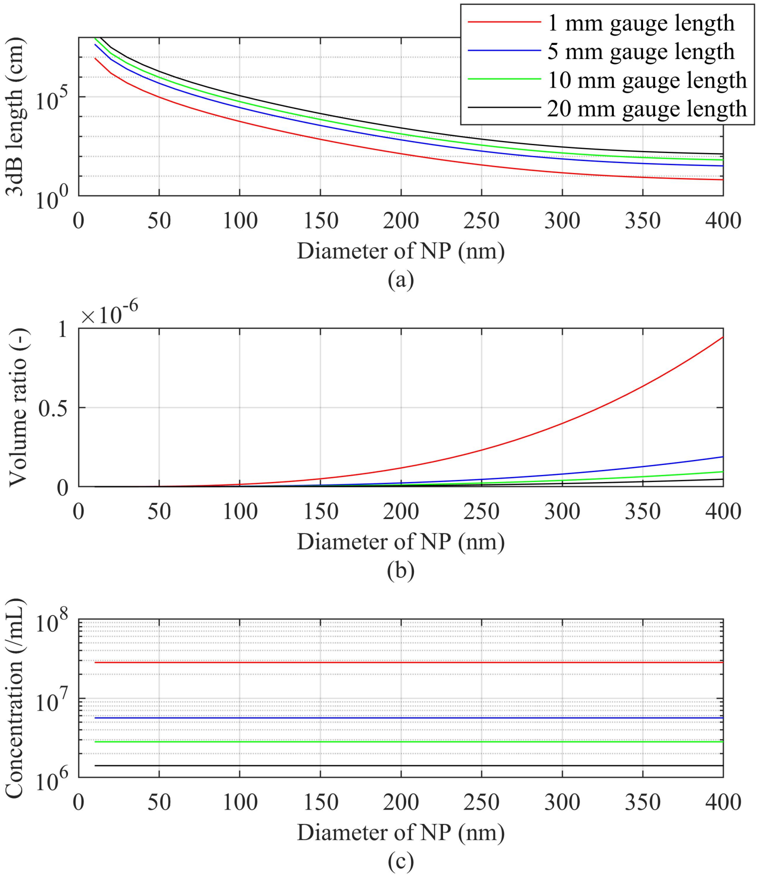

Figure 5.10: The minimum gold NP-doping cases to manufacture NP-doped optical fibre strain gauges. (a) The 3 dB light loss length versus diameter of gold NPs. (b) The corresponding volume ratios. (c) The corresponding concentrations.

BIBLIOGRAPHY

[1] M. Froggatt and J. Moore, “High-spatial-resolution distributed strain measurement in optical fiber with Rayleigh scatter”, *Applied Optics*, vol. 37, no. 10, pp. 1735–1740, 1998.

[2] A. Güemes, A. Fernández-López, and B. Soller, “Optical fiber distributed sensing-physical principles and applications”, *Structural Health Monitoring*, vol. 9, no. 3, pp. 233–245, 2010.

[3] P. Lu, N. Lalam, M. Badar, B. Liu, B. T. Chorpening, M. P. Buric, and P. R. Ohodnicki, “Distributed optical fiber sensing: Review and perspective”, *Applied Physics Reviews*, vol. 6, no. 4, p. 041 302, 2019.

[4] C. Liang, Q. Bai, M. Yan, Y. Wang, H. Zhang, and B. Jin, “A comprehensive study of optical frequency domain reflectometry”, *IEEE Access*, vol. 9, pp. 41 647–41 668, 2021.

[5] S. Minakuchi and N. Takeda, “Recent advancement in optical fiber sensing for aerospace composite structures”, *Photonic Sensors*, vol. 3, no. 4, pp. 345–354, 2013.

[6] A. Barrias, J. R. Casas, and S. Villalba, “A review of distributed optical fiber sensors for civil engineering applications”, *Sensors*, vol. 16, no. 5, p. 748, 2016.

[7] P. Lu, S. J. Mihailov, D. Coulas, H. Ding, and X. Bao, “Low-loss random fiber gratings made with an fs-IR laser for distributed fiber sensing”, *Journal of Lightwave Technology*, vol. 37, no. 18, pp. 4697–4702, 2019.

[8] S. Loranger, M. Gagné, V. Lambin-Iezzi, and R. Kashyap, “Rayleigh scatter based order of magnitude increase in distributed temperature and strain sensing by simple UV exposure of optical fibre”, *Scientific Reports*, vol. 5, no. 1, pp. 1–7, 2015.

[9] F. Parent, S. Loranger, K. K. Mandal, V. L. Iezzi, J. Lapointe, J. S. Boisvert, M. D. Baiad, S. Kadoury, and R. Kashyap, “Enhancement of accuracy in shape sensing of surgical needles using optical frequency domain reflectometry in optical fibers”, *Biomedical Optics Express*, vol. 8, no. 4, pp. 2210–2221, 2017.

[10] A. Yan, S. Huang, S. Li, R. Chen, P. Ohodnicki, M. Buric, S. Lee, M. Li, and K. P. Chen, “Distributed optical fiber sensors with ultrafast laser enhanced Rayleigh backscattering profiles for real-time monitoring of solid oxide fuel cell operations”, *Scientific Reports*, vol. 7, no. 1, pp. 1–9, 2017.

[11] Y. Xu, L. Zhang, S. Gao, P. Lu, S. Mihailov, and X. Bao, “Highly sensitive fiber random-grating-based random laser sensor for ultrasound detection”, *Optics Letters*, vol. 42, no. 7, pp. 1353–1356, 2017.

[12] J. Thomas, M. Myara, L. Troussellier, E. Burov, A. Pastouret, D. Boivin, G. Mélin, O. Gilard, M. Sotom, and P. Signoret, "Radiation-resistant erbium-doped-nanoparticles optical fiber for space applications", *Optics Express*, vol. 20, no. 3, pp. 2435–2444, 2012.

[13] E. J. Friebele, C. Baker, C. G. Askins, J. P. Fontana, M. P. Hunt, J. R. Peele, B. A. Marcheschi, E. Oh, W. Kim, J. Sanghera, *et al.*, "Erbium nanoparticle doped fibers for efficient, resonantly-pumped Er-doped fiber lasers", in *Fiber Lasers XII: Technology, Systems, and Applications*, International Society for Optics and Photonics, vol. 9344, 2015, p. 934 412.

[14] C. F. Bohren and D. R. Huffman, *Absorption and Scattering of Light by Small Particles*. Wiley, 1998.

[15] D. Tosi, C. Molardi, and W. Blanc, "Rayleigh scattering characterization of a low-loss MgO-based nanoparticle-doped optical fiber for distributed sensing", *Optics & Laser Technology*, vol. 133, p. 106 523, 2021.

[16] V. Fuertes, N. Grégoire, P. Labranche, S. Gagnon, R. Wang, Y. Ledemi, S. LaRochelle, and Y. Messaddeq, "Engineering nanoparticle features to tune Rayleigh scattering in nanoparticles-doped optical fibers", *Scientific Reports*, vol. 11, no. 1, pp. 1–12, 2021.

[17] A. Beisenova, A. Issatayeva, S. Korganbayev, C. Molardi, W. Blanc, and D. Tosi, "Simultaneous distributed sensing on multiple MgO-doped high scattering fibers by means of scattering-level multiplexing", *Journal of Lightwave Technology*, vol. 37, no. 13, pp. 3413–3421, 2019.

[18] O. Liba, E. D. SoRelle, D. Sen, and A. de La Zerda, "Contrast-enhanced optical coherence tomography with picomolar sensitivity for functional in vivo imaging", *Scientific Reports*, vol. 6, no. 1, pp. 1–12, 2016.

[19] P. Si, E. Yuan, O. Liba, Y. Winetraub, S. Yousefi, E. D. SoRelle, D. W. Yecies, R. Dutta, and A. de la Zerda, "Gold nanoprisms as optical coherence tomography contrast agents in the second near-infrared window for enhanced angiography in live animals", *ACS Nano*, vol. 12, no. 12, pp. 11 986–11 994, 2018.

[20] X. Wang, R. Benedictus, and R. M. Groves, "Modelling of light scattering by gold nanoparticles at optical fibre interfaces", *Journal of Optics*, vol. 23, no. 3, p. 035 602, 2021.

[21] X. Wang, R. Benedictus, and R. M. Groves, "Optimization of light scattering enhancement by gold nanoparticles in fused silica optical fiber", *Optics Express*, vol. 29, no. 13, pp. 19 450–19 464, 2021.

[22] P. Bulot, O. Cristini, M. Bouet, A. Demol, L. Bigot, G. Bouwmans, S. Plus, R. Habert, G. Laffont, and M. Douay, "OFDR distributed temperature sensing at 800 °C on a fiber with enhanced Rayleigh scattering profile by doping", in *Bragg Gratings, Photosensitivity and Poling in Glass Waveguides and Materials*, Optical Society of America, 2018, BM3A–2.

[23] G. Morales-Luna and M. Morales-Luna, “Effective medium theory to the description of plasmonic resonances: Role of Au and Ti nanoparticles embedded in MoO_3 thin films”, *Scientific Reports*, vol. 10, no. 1, pp. 1–12, 2020.

[24] L. B. Scaffardi and J. O. Tocho, “Size dependence of refractive index of gold nanoparticles”, *Nanotechnology*, vol. 17, no. 5, pp. 1309–1315, Feb. 2006.

[25] E. Li, “Rayleigh scattering based distributed optical fiber sensing”, in *AOPC 2017: Fiber Optic Sensing and Optical Communications*, International Society for Optics and Photonics, vol. 10464, 2017, 104641K.

[26] I. H. Malitson, “Interspecimen comparison of the refractive index of fused silica”, *Journal of the Optical Society of America*, vol. 55, no. 10, pp. 1205–1209, 1965.

[27] X. Wang, R. M. Groves, and R. Benedictus, *Matlab code and dataset for the spectral characteristics of gold nanoparticle doped optical fibre*, 4TU.ResearchData. https://doi.org/10.412

6

CASE STUDY OF STRAIN ACQUISITION OF GOLD NANOPARTICLE-DOPED DISTRIBUTED OPTICAL FIBRE SENSING BASED ON BACKSCATTERING

In the previous chapter 5, it can be seen from the analysis of the backscattering spectra of nanoparticle-doped optical fibre that the response of the spectral shift under strain is close to a linear response when the nanoparticle doping satisfies with the single backscattering restriction within sensing length. The corresponding strain values can be obtained by obtaining the spectral shift values divided by the response value. Due to the introduction of the nanoparticles, the scattering signal has the potential to be greatly enhanced. The enhancement of the scattered light signal results in a change in the signal to noise ratio. How does the precision and accuracy of strain measurement of a nanoparticle-doped optical fibre sensor change when the signal to noise ratio changes? What is its sensitivity? In this chapter, the traditional cross-correlation demodulation method was used to obtain the strain values for different gauge lengths and detected spectral ranges to evaluate the demodulation precision and accuracy. A demodulation method was proposed to improve the measurement accuracy.

Parts of this chapter have been submitted to Structural Health Monitoring.

NANOPARTICLE(NP)-DOPED optical fibres show the potential to increase the signal-to-noise ratio and thus the precision of optical fibre strain detection for structural health monitoring. In this chapter, the previous experimental/simulation study is extended to a design study for structural health monitoring (SHM) in order to answer sub-research question 4: What is the effect of the sensitivity change and their effect for SHM for material?

100 nm size spherical gold NPs were randomly seeded in the optical fibre core to increase the intensity of backscattered light. Backscattered light spectra were obtained in different wavelength ranges around the infrared C-band and for different gauge lengths. Spectral shift values were by cross-correlation of the spectra before and after strain change. The results showed that the strain accuracy has a positive correlation with the period number and that the strain precision decreases with increasing noise. Based on the simulated results, a formula for the sensitivity of the NP-doped optical fibre sensor was obtained, using an aerospace case study to provide realistic strain values. An improved method is proposed to increase the accuracy of strain detection based on increasing the period number and the results showed that the error was reduced by about 50 %, but at the expense of a reduced strain measurement range and more sensitivity to noise.

6.1. INTRODUCTION

Structural health monitoring (SHM) of aerospace structural components is intended to monitor the structural integrity status which is used for maintenance decision-making to prevent accidents caused by the failure of these components. The ultimate purpose of SHM is to give an automated and real-time assessment of the structure [1]. SHM relies on different sensing technologies. Such as strain sensing [2], crack detection [3], measurement modalities[4], etc. Also, SHM methods can use static or dynamic measurement approaches [4].

Fibre optic sensors (FOS) offer an attractive option for strain sensing which can be used for SHM decision-making. Structural damage will cause departures in the strain field after loading [5]. By analysing the strain information continuously, the presence or the position of damage can be obtained. Compared with electrical strain gauges, FOS have the advantages of resistance to corrosion [6], immunity to electromagnetic interference [7] and their small size and low weight make them suitable to embed in composite materials [6]. They can also measure temperature [8], chemical parameters (pH, relative humidity) [9], material degradation [10], vibration [11], and load [12]. The most commonly used optical fibre sensing methods for SHM include distributed fibre optic sensing [13] and fibre Bragg gratings sensing [14], [15]. Compared with fibre Bragg gratings, distributed fibre optic sensors (DFOS) have the advantage that can obtain strain information along the length of the sensing fibres. One principle of DFOS is based on Rayleigh backscattering where spectral wavelength shifts of the backscattered light in the optical fibre under strain are used to obtain the strain change values [13]. Combined with the optical frequency domain reflectometry (OFDR) method [16], this allows the distributed strain information to be demodulated. High spatial resolution distributed strain sensing based on Rayleigh scattering was developed by [13] with a strain resolution of $5\mu\epsilon$ and a spatial resolution of 30 cm. It has since been developed to have a strain resolution of up to be 1$\mu\epsilon$ with a spatial resolution of up to 1cm [17] and has been developed for long-distance (more than 300 m) detection [18]. There are plenty of applications of DFOS for SHM, for example, damage detection for a carbon fibre reinforced plastic (CFRP) beam and a composite wing [19] and the state sensing of a composite winglet structure [20].

The strain measurement performance of a DFOS directly determines the final performance of SHM and high-performance sensing is beneficial to SHM [21].

One of the limitations which restricts DFOS based on Rayleigh backscattering is that this method uses the backscattered light in the core of the optical fibres while the Rayleigh scattering in the core of commercial optical fibres is generally low [22]. For a commercial optical fibre, the backscattered light signal is as low as -100 dB/mm [23]. By increasing the backscattered light in the core of the optical fibres, the signal-to-noise ratio (SNR) may increase allowing the precision of the strain detection to increase.

Some previous research shows improvements of the strain/temperature measurement based on increasing the backscattered light signals [22], [24]. Doping nanoparticles (NPs) into the core of the optical fibre is a direct approach to increasing the backscattered light [25]–[27] and gold NPs are competitive contrast agents that can be used for increasing backscattered light [28]. If gold NP-doped optical fibre is used in strain detection for SHM, a higher SNR signal may improve the precision of the strain measurement for SHM which is beneficial for critical locations. For example, critical locations include the areas close to the rivet holes in the aluminium fuselage where small cracks may form [29]. These small cracks will induce a small localised strain change compared to a healthy structure, so need a high strain sensitivity to be detected.

With NP-doping, the intensity of the backscattered light in the optical fibre will increase to overcome the drawback of low backscattering intensity of commercial optical fibres. However, the theoretical performance of the NP-doped FOS for strain monitoring is unclear.

In this chapter, strain acquisition of gold NP-doped distributed fibre optic sensing will first be investigated with the cross-correlation method. The errors caused using the cross-correlation method for NP-doped optical fibre will be evaluated for different random-seeded optical fibre gauge lengths without noise and for the specific random-seeded optical fibre gauge lengths under different levels of noise. By linear fitting, the sensitivity of the NP-doped optical fibre strain gauges can be obtained. To improve the accuracy of strain detection with the cross-correlation method for NP-doped optical fibre sensors, a new method is proposed to increase the accuracy of strain detection.

6.2. METHODOLOGY

6.2.1. EXPERIMENTAL SETUP AND THE PRINCIPLE

Figure 6.1 shows a simplified diagram of the strain detection system based on backscattering by the NPs. It consists of a wavelength-tunable laser, optical fibre couplers, an optical fibre circulator, optical fibres, a sensing fibre containing gold NPs, a photodetector and an optical trap. The light signals detected by the photodetector are processed by the computer which is not shown in the figure.

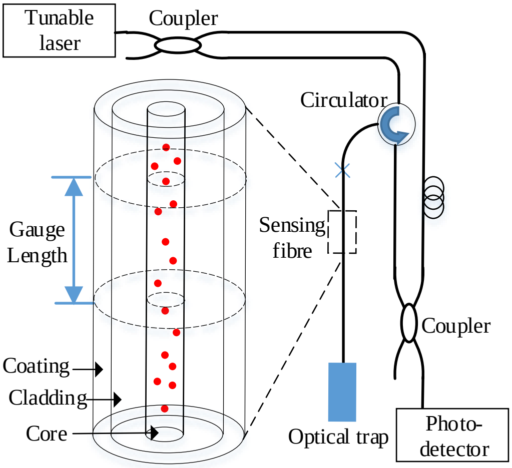

Figure 6.1: The structure of the experimental setup. Part of the sensing fibre within the rectangular region is enlarged to show the details. The red dots show gold NPs randomly distributed in the core of the optical fibre. The outer layers are the cladding and coating.

Light emitted from the tunable laser is split by an optical coupler into sensing and reference paths. The gold NPs are randomly distributed in the sensing fibre core volume. Light is backscattered by the NPs and recoupled into the optical fibre in the backward direction. There is an optical trap at the end of the sensing fibre which is used to reduce the reflection at the optical fibre end tip, which can be a refractive index (RI) matching liquid or a no-core optical fibre. The backscattered light passes through the optical circulator and then interferes with light from the reference arm at the optical fibre coupler. Optical beat signals obtained at the photodetector are demodulated by Fourier transform to recover the intensity and phase of the backscattered light in each gauge length.

The beat signals can be expressed as [30], [31]:

$$PD_2 \approx \sum_i r_i(k)\cos 2n_{eff} z_i k, \tag{6.1}$$

where, r_i is the reflection coefficient at position z_i of the sensing fibre and the squared magnitude $|r_i|^2$ is the reflectance. The spatial distances between the i^{th} and the $(i+1)^{th}$ detection points (spatial resolution) are determined by the effective RI of the optical fibre and the tuning wavelength range is $\Delta z = \lambda_s \lambda_f / 2n\Delta\lambda$, where λ_s is the starting wavelength of the tunable laser and λ_f is the final wavelength, $\Delta\lambda$ is the wavelength tuning range, n_{eff} is the effective RI of the optical fibre [32] and k is the wavenumber. For a tunable laser source with a starting wavelength at 1540 nm and a final wavelength at 1560 nm, the spatial resolution is about 41nm when the RI is 1.45. If the gauge length is set at 1mm, there are about 24 detection points in the gauge length. It can be seen from Equation 6.1 that PD_2 contains information about the position (z_i) and the wavenumber (k) and it can be transformed by Fourier transform. Because the laser is linear tuning, the beat signals are proportional to the positions of z_i [33]. By square windowing the positions within the gauge length and using an inverse Fourier transform, the intensity and phase of the scattered light spectra within the gauge length can be obtained. Then, the spectral shift can be obtained using cross-correlation between the reference spectrum and the spectrum after the strain is applied [34].

6.2.2. THE METHOD OF THE SPECTRAL SHIFT DETECTION BY CROSS-CORRELATION METHOD WITH GOLD NP-DOPED OPTICAL FIBRE

The accuracy of the cross-correlation was evaluated by comparing the theoretical spectral shift under strain and the spectral shift result from the cross-correlation method. The central wavelength of the tunable laser was set at 1550 nm. The wavelength tuning ranges were set at 10 nm, 20 nm and 40 nm, which correspond to the wavelength ranges 1545 nm - 1555 nm, 1540 nm - 1560 nm and 1530 nm - 1570 nm respectively. The simulated spectra were in the wavelength domain with a high spectral resolution of 1 pm in order to accurately reconstruct the spectra. In this case, the spectral shift (R_{xy}) was calculated by the cross-correlation method in the wavelength domain as:

$$R_{xy}(n) = \frac{1}{N}\sum_{m=0}^{N-1}[x(m)-\overline{x}][y(n+m)-\overline{y}], \tag{6.2}$$

where, $n = -(N-1), -(N-2), ..., N-2, N-1$. N is the wavelength sampling point. The sampling points were mapped to a uniform scale in the wavelength domain. The resolution was set at 1 pm. y and x correspond to the reference spectrum and the spectrum under strain, respectively.

Strain was applied to the sensing fibre. In this case, the relative positions of the gold NPs in the sensing fibre will change and the RI of the optical fibre will change also. The backscattered spectra from the NPs in the gauge length were modelled by a single scattering model which means the light will be backscattered once in the propagation direction and can be expressed as

$$\lambda'_{NP} \approx \lambda_{NP}(1+\varepsilon_{fibre}+\eta_m\varepsilon_{fibre}), \tag{6.3}$$

where, λ'_{NP} is the spectrum under strain and λ_{NP} is the reference spectrum. $\eta_m = -(p_{12}-\nu(p_{11}+p_{12}))n^2/2 = -0.1997$ is the parameter caused by the RI change under strain when $\nu = 0.17$, $p_{11} = 0.113$, $p_{12} = 0.252$ and $n = 1.45$ for the optical fibre. Therefore, the theoretical spectral shift under strain is 1.240465 $\text{pm}/\mu\epsilon$ which was set as the true value used to compare with the simulated results.

The gauge lengths were set at 0.1069 cm, 0.2138 cm, 0.3207 cm, 0.4276 cm, 0.5345 cm, 0.6414 cm, 0.7483 cm, 0.8552 cm, 0.9621 cm and 1.0690 cm. These lengths were chosen to be integer multiples (about 2000, 4000, 6000, 8000, 10000, 12000, 14000, 16000, 18000, and 20000 times respectively) of the grating period of the fibre Bragg gratings for a wavelength at 1550 nm.

From the previous work, low-concentration NP-doping shows similar spectral characteristics in the wavelength and wave number domains [35] for different sizes of NPs. To simplify the simulation, only 100 NPs (100 nm diameter) were randomly seeded in the gauge lengths for a low concentration of NP doping. Once the NPs have been seeded, the spectral intensity can be expressed by the square of the accumulation of the electric field caused by the scattering from the NPs as:

$$I_s(\lambda) \approx |\sum_{i=1}^{N} E_0 A_i \exp\left(j\frac{4\pi n_m l_i}{\lambda}(1+\varepsilon+\eta_m\varepsilon)\right)|^2. \tag{6.4}$$

where, E_0 is the electrical field of the incident light, $A_i = r(l_i)\exp\left(-6\pi f n_m \Re S(0) l_i/\lambda x^3\right)$, $r(l_i)$ is the reflection coefficient of the NP at position of l_i, f is the volume ratio of gold NP in the optical fibre, n_m is the RI of the optical fibre, $\Re$ is the real symbol, $S(0)$ is the forward scattering amplitude, λ is the wavelength of the incident light, x is the size parameter of the gold NP, j is the imaginary unit and ε represents axial strain.

The spectra can be transferred to spatial frequency ($1/\lambda$) by Fourier transform to evaluate the fluctuation within 1 nm. In order to obtain this fluctuation, a threshold was set at $1/e$ of the maximum value in the spatial frequency domain. The first spatial frequency value over the threshold from half of its maximum spatial frequency to the low spatial frequency was chosen as its fluctuation number was within 1 nm. Note: the spectra were normalised to the range 0-1 and were then subtracted from the mean values of the spectra. The period number was defined as the fluctuation number within 1 nm times the wavelength range.

6.2.3. A NEW METHOD FOR INCREASING THE ACCURACY OF SPECTRAL SHIFT DETECTION

Because the accuracy of the cross-correlation is proportional to the period number (see Results and Discussion section), a method based on increasing the period number is proposed. First the original spectra were normalised to the range 0-1 and then the direct current part of the normalised spectra were deduced by subtracting their mean values. Then, the absolute values of the spectra were used for cross-correlation to obtain the spectra shift between spectra under strain and spectra without strain. By using the absolute values of the spectra, additional high frequency information was added to the original spectra. Therefore, the period number increases and then the cross-correlation may increase.

The proposed method can be expressed as:

$$R'_{xy}(n) = \frac{1}{N}\sum_{m=0}^{N-1}(|x(m)-\overline{x}| - \overline{|x(m)-\overline{x}|})\cdot(|y(n+m)-\overline{y}| - \overline{(y(n+m)-\overline{y}|}). \tag{6.5}$$

To make the procedure which has been described above clear, Figure 6.2 shows the case for spectra generated by 100 nm size gold NPs randomly distributed in the gauge length of 0.3207 cm used for the cross-correlation method and the proposed method. The spectral range was set from 1545 nm to 1555 nm and the wavelength resolution was set at 1 pm. Figure 6.2 (a) shows the original backscattered light

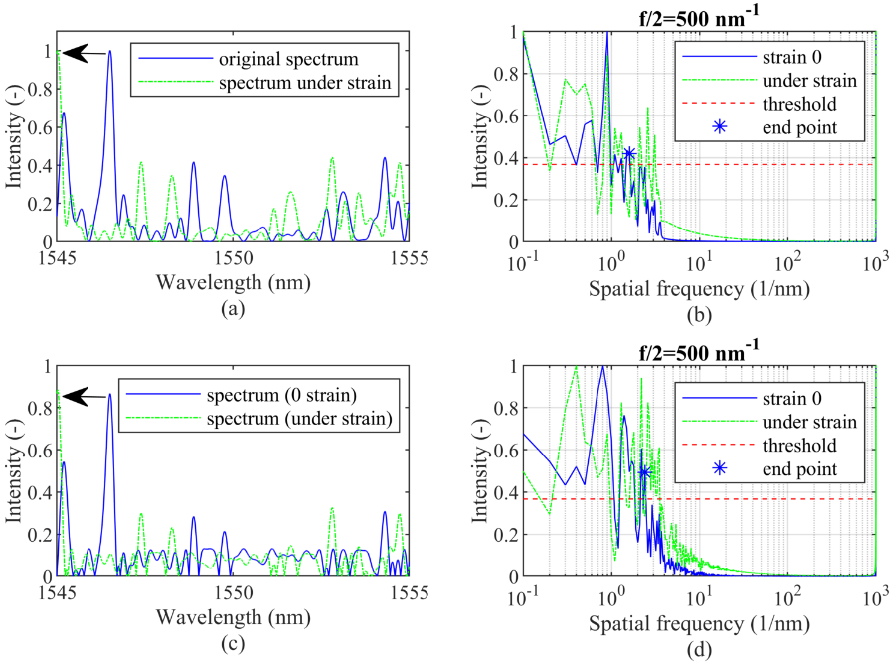

Figure 6.2: A case of the spectra of the random distribution of NPs in the optical fibre with gauge length of 0.3207 cm for strain at $-1200\,\mu\epsilon$. (a) The original spectra and spectra under strain. (b) The results of the spectra with Fourier transform. (c) The spectra modulated by proposed method. (d) The results of the modulated spectra with Fourier transform. The black arrows show the spectral shift directions under $-1200\,\mu\epsilon$.

spectra by blue lines and the spectra under strain at $-1200\,\mu\varepsilon$ by green lines. The results of the spectra shown in Figure 6.2 (a) after Fourier transform are shown in Figure 6.2 (b). Half of the sampling frequency is $500\,\mathrm{nm}^{-1}$, which is much larger than the 3 dB frequency of the spatial frequency. In this case, the sampling rate is two times larger than the Nyquist frequency. Therefore, the spectral information can be recovered with this resolution. Figure 6.2 (c) shows the spectra with the proposed method and Figure 6.2 (d) shows the intensity information after Fourier transform.

In this work, the performance of the signal enhanced distributed fibre optical sensing based on backscattering by doping gold NPs will be investigated by simulations with a single scattering model in order to improve the sensing performance. The simulation results of the nanopariticle doped optical fibre sensors will be shown in the next section.

6.3. SIMULATION RESULTS

The results of the cases of the accuracy of the spectral shift acquisition based on the cross-correlation method will be shown. The first three cases were generated by 100 times random seeding NPs without noise for different gauge lengths. The following three cases were generated with the same selected random seeding NPs distribution with different noise levels and different gauge lengths to assess the accuracy with the cross-correlation method used for NP-doped optical fibre sensors.

6.3.1. SPECTRAL ANALYSIS WITH 100 RANDOM SEEDINGS WITHOUT NOISE

Figure 6.3 shows the strain errors between the simulated results and the theoretical results. The simulated results were obtained with the cross-correlation method to calculate spectral shifts under strain for spectral detection ranges 10 nm, 20 nm and 40 nm with the central wavelength of 1550 nm in Figure 6.3 (a), (b) and (c) respectively. The true values (theoretical results) were obtained by using the theoretical response of the spectral shift (1.240465 pm/$\mu\epsilon$) multiplied by the strain values. The strain range was set from -3000 $\mu\epsilon$ to 3000 $\mu\epsilon$ and the strain interval was set at 100 $\mu\epsilon$. The gauge lengths were set at 0.1069 cm, 0.2138 cm, 0.3207 cm, 0.4276 cm, 0.5345 cm, 0.6414 cm, 0.7483 cm, 0.8552 cm, 0.9621 cm and 1.0690 cm respectively.

To show the ratios of the deviation between the calculated mean values and the true values, the relative error is defined as:

$$E_r = \left| \frac{calculated\ result - true\ value}{true\ value} \times 100\% \right|. \tag{6.6}$$

The relative errors between mean values and the true values are shown in Figure 6.3 (a-1), (b-1) and (c-1). They were obtained by averaging the 100 cases of the obtained errors. Because Equation 6.6 cannot be used for the cases for strain at 0, the results close to strain at 0 are not available.

In the small gauge length ranges, as seen from Figure 6.3 (a-1), the calculated mean spectral shifts were not sufficient to reach the true spectral shifts, especially

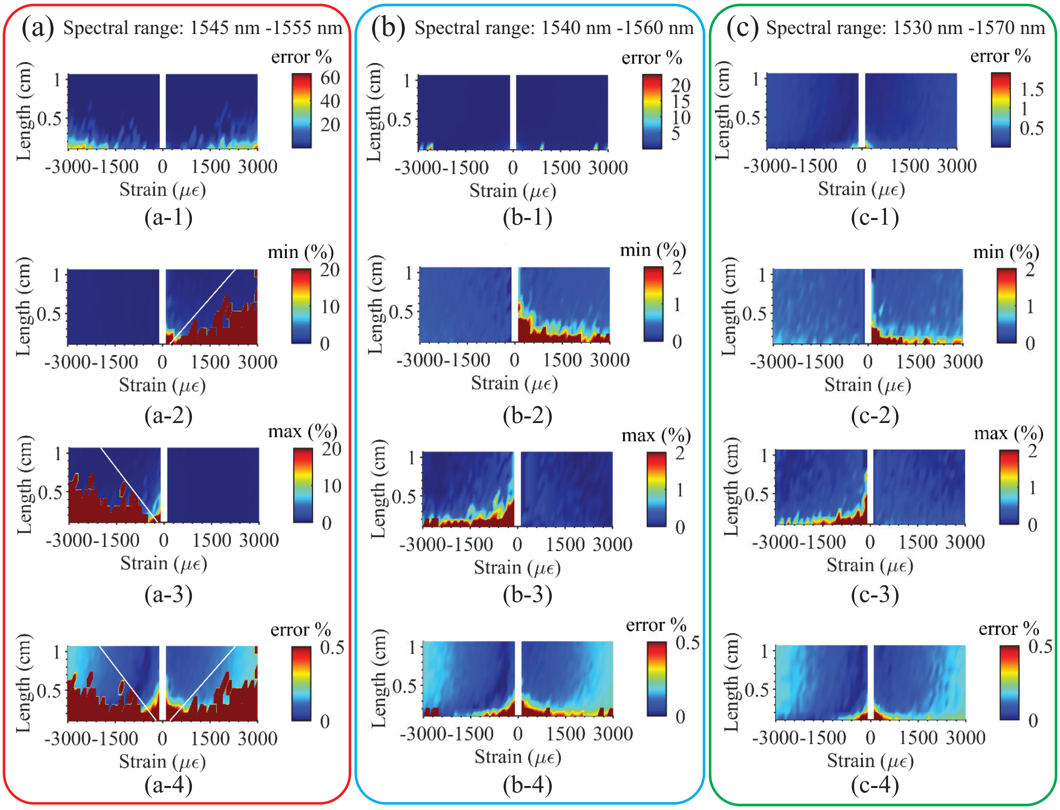

Figure 6.3: The errors of the strains. The cross-correlation results for the spectral range of (a) 10 nm. (b) 20 nm and (c) 40 nm. The numbers (-1, -2, -3 and -4) in figures (a) to (c) correspond to the relative errors between the mean values and true values, the relative errors between the minimum values and the true values, the relative errors between the maximum values and the true values, and the relative errors between the mean values and true values with a threshold error of 0.5% respectively.

for larger strain values. A reason for this may be that a large strain causes a large spectral shift and a larger spectral shift causes a higher percentage of the spectrum moving out of the spectral detection range and being replaced by new spectrum and the new spectrum has no correlation with any regions of the original spectrum. The high errors shown in Figure 6.3 (a-1) represent the failure of strain acquisition with the cross-correlation method. To show the degree of dispersion of the 100 randomly seeding cases, the errors calculated with the minimum data and the maximum data in the 100 cases for each gauge length and strain were compared with the true values shown in Figure 6.3 (a-2) and (a-3) respectively. A threshold of 20 % was set for both figures to show the regions where the errors are above 20 % and more details about the regions where the errors are below 20 %. It is interesting to see that significant errors only exist in positive strain regions in Figure 6.3 (a-2) for the calculated minimum errors and only exist in negative strain regions in Figure 6.3 (a-3) for the calculated maximum errors. This indicates that some cases failed when the cross-correlation method was used. Figure 6.3 (a-4) shows the standard deviations of strain errors. The white line shows a boundary around the threshold in Figure 6.3 (a-4) and the white line passes through (0 $\mu\epsilon$, 0 cm) and (2300 $\mu\epsilon$, 1.0690 cm). The boundary lines shown in Figure 6.3 (b-4) pass through (0 $\mu\epsilon$, 0 cm) and (-2000 $\mu\epsilon$, 1.0690 cm). The two white lines were also drawn in Figure 6.3 (a-4) and similar boundaries are shown when the threshold was set at 0.5 %. The standard deviations are quite small but the errors calculated with the maximum results and minimum results shown in Figure 6.3 (a-2) and (a-3) are large, which also indicates a failure of the spectral shift acquisitions with the cross-correlation method and indicates that the failure cases have a low proportion for the 100 randomly cases.

Figure 6.3 (b-1), (b-2) and (b-3) show errors between the mean values and the theoretical values, the errors between the minimum calculated results and the theoretical values and the errors between the maximum calculated results and the theoretical values respectively. The errors between the mean values and the theoretical values shown in Figure 6.3 (b-1) are small compared with the results in Figure 6.3 (b-1). Only the regions close to the smallest gauge lengths for some large strain values show high error values. Because the relative errors are quite small, the threshold was set at 2 % for the results shown in Figure 6.3 (b-2) and (b-3). With the 2 % error threshold, the regions of the errors above the threshold are similar to the regions of the errors above the threshold of 20 % shown in Figure 6.3 (a-2) and (a-3). Figure 6.3 (b-4) shows the standard deviations of strain errors. In Figure 6.3 (b-4), the errors are reduced to lower values compared with Figure 6.3 (a-4) especially for the regions for larger strain and small gauge length. However, errors still exist in regions with a small strain and a small gauge length. The figure is not symmetric as can be seen from the dark blue and light blue zones in Figure 6.3 (b-4). The reason for this is unclear.

The results for the 40 nm spectral detection range (1530 nm - 1570 nm) case are shown in Figure 6.3 (c). Figure 6.3 (c-1) to (c-4) show the errors between the mean values and the theoretical values, the errors between the minimum calculated results and the theoretical values, the errors between the maximum calculated results and the theoretical values and the standard deviations of strain errors respectively.

The errors between the mean values and the theoretical values in Figure 6.3 (c-1) are smaller than the results shown in Figure 6.3 (a-1) and (b-1). Only the regions close to the smallest gauge lengths show high error values. The threshold was set at 2 % for the results shown in Figure 6.3 (c-2) and (c-3) which is the same as the threshold in Figure 6.3 (b-2) and (b-3). The threshold set in Figure 3 (c-4) was 0.5 %. With the same thresholds, it can be seen that the errors decrease when the spectral ranges increase.

The above results show the randomly positioned NP cases and the corresponding statistical results for different spectral ranges without noise. In the following part, different levels of random intensity noise will be added to the spectral signals obtained from a random spatial distribution in the same gauge lengths, strain ranges and spectral ranges. The failure caused by the cross-correlation was avoided in this selected NP relative spatial distribution.

6.3.2. SPECTRAL ANALYSIS WITH A SPECIFIC RANDOM SEEDING WITH NOISE

Figure 6.4 (a) shows the direct errors between the mean values of the spectral shifts calculated with the cross-correlation method with different noise levels. The strain values can be obtained by using the theoretical response of the spectral shift. The direct error was defined as:

$$E_d = calculated\ result - true\ value. \tag{6.7}$$

The mean values were the averaged results of 100 spectra superposed with randomly generated noise. It is assumed that the noise follows a Gaussian distribution with a mean value of 0 and a standard deviation of σ_n. The noise level in the simulation was defined as:

$$N = \frac{\sigma_n}{max\{I_s\}}, \tag{6.8}$$

where, $max\{I_s\}$ represents the maximum value of the original backscattered light spectrum without noise in the gauge lengths. It is assumed that σ_n is independent of the intensity of the signal. Figure 6.4 (a-1) to (a-3) show the errors between the mean values of the spectral shifts calculated with the cross-correlation method under noise levels of 0 % for spectral ranges of 10 nm, 20 nm and 40 nm respectively. (The results for noise levels of 10%, 20%, 30%, 40% and 50% are not shown because noise shows no influence on the mean values.)

The original spectrum without noise was normalised to 0-1 and then noise with noise level N was added to the original spectrum. By setting the noise level, spectra with different noise levels can be simulated. In this case, the approximated SNR ratio can be expressed as:

$$SNR_L = \frac{max\{I_s\}^2}{\sigma_n^2}, \tag{6.9}$$

or as SNR_L ratio in dB as:

$$SNR_{L_{dB}} = 10\log\frac{max\{I_s\}^2}{\sigma_n^2}, \tag{6.10}$$

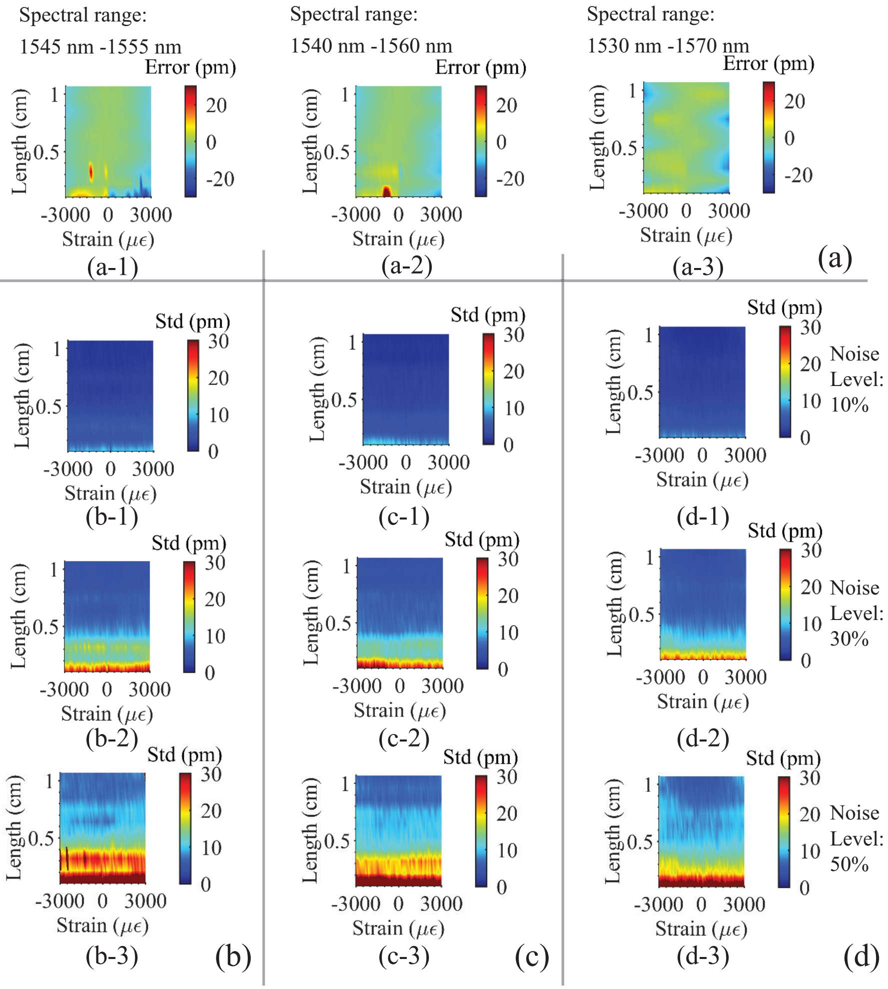

Figure 6.4: The simulated results of strain acquisition. (a-1) to (a-3) The errors between the spectral shift obtained and the theoretical results for spectral ranges of 10 nm, 20 nm and 40 nm respectively. (b)-(c) The standard deviations of the spectral shift for spectral ranges of 10 nm, 20 nm and 40 nm respectively. The numbers (-1, -2 and -3) for figures (b) to (d) correspond to results under noise levels of 10%, 30% and 50% respectively.

Figure 6.4 (a) shows the errors between the calculated values and the true values for 10 nm, 20 nm, 40 nm spectral ranges respectively. In Figure 6.4 (a-1), the errors between the calculated values and the true values become notable when the gauge lengths are small. There is a noticeable error around the point (-1200 $\mu\epsilon$, 0.3207 cm). The reason for this noticeable error can be illustrated with the spectra shown in Figure 6.2 (a). Figure 6.2 (a) shows the corresponding spectrum for the strain at -1200 $\mu\epsilon$ and for the gauge length set at 0.3207 cm. Under the strain value of -1200 $\mu\epsilon$, the original spectrum in blue has a blue shift. The arrow shows the spectral shift under this strain value and the spectrum under this strain values was in green. As shown in Figure 6.2 (a), there is a distinguishable peak near the arrow and the intensity of the peak is much larger than the other peaks values shown in the spectral range. Therefore, the shift of this peak has a high influence on calculating the spectral shift under strain with the cross-correlation method. For the strain value at -1200 $\mu\epsilon$, the peak shifts out of the spectral range which is a reason for the high error near this point shown in Figure 6.2 (a). This result indicates that the accuracy of obtaining the spectral shift not only depends on the gauge lengths and the strain ranges but the accuracy also depends on the characteristics of the original spectrum. Figure 6.4 (a-2) and (a-3) show smaller errors than errors in Figure 6.4 (a-1), but the characteristics of the original spectrum depend on the distribution of the NPs. For example, in Figure 5 (a-2) a remarkable error occurs at negative strain and the shortest gauge length for calculation. The positions of the high error points depend on the characteristics of the original spectrum. By adjusting the spectral range, the high error points can be moved.

Figure 6.4 (b), 5 (c) and 5 (d) show the standard deviations of the spectral shift obtained with the cross-correlation method with the same random NP seeding distribution in the gauge lengths with the 10 nm, 20 nm and 40 nm spectral range under different noise levels (10 %, 30 % and 50 %) respectively. As the noise level increases, the standard deviations increase especially for the short gauge lengths. For a specific noise level, the standard deviations of the results caused by the noise are similar for different strain values. The standard deviation shows a positive relevant relationship with the noise level.

6.4. ANALYSIS AND DISCUSSION

In the previous subsections for different spectral ranges with random seedings, the results for the accuracy of spectral shifts demodulation with cross-correlation method were shown. The value of spectral shift times the theoretical responsivity of strain (about 1.24 pm/$\mu\epsilon$) is the obtained strain results. By increasing the detected spectral range, the accuracy of the strain acquisition increases with the cross-correlation method. Although these results show the tendency of some relationships, the mathematical relationship between parameters (for example spectral range, gauge length, etc.) is unclear. The failure of the strain acquisition shown in the results of subsections of spectral range 1545 nm to 1555 nm with random seedings, spectral range 1540 nm to 1560 nm with random seedings and spectral range 1530 nm to 1570 nm with random seedings causes a difficulty to obtain a formula to show the relationships, so the results from the subsections of spectral ranges 1545 nm to 1555 nm, 1540 nm to 1560 nm and 1530 nm to 1570 nm with the specific random seedings are used for further analysis since these results show the strain acquisition without failure.

In this section, further analysis from the parameters (spectral range, gauge length, signal to noise ratio) will be investigated in order to obtain a formula for evaluating the sensitivity of the NP-doped optical fibre sensors. This is followed by an aerospace case study of real strain data obtained by LUNA system (ODiSI-B) with commercial optical fibres is used as a comparison with the simulated results from NP-doped optical fibre sensors. Finally, the results of the proposed new spectral shift demodulation method are shown and discussed.

6.4.1. SENSITIVITY OF THE NP-DOPED OPTICAL FIBRE SENSORS

By some mathematical transforms, the spectral characteristics and the standard deviations of the obtained strain values are plotted in Figure 6.5 and they show an approximate linear relationship.

The results shown in Figure 6.5 are processed from the standard deviation data obtained from the cases in Figure 6.4 and the corresponding period numbers. The horizontal axis is the reciprocal of spatial frequency (R) and the vertical axis is the modified standard deviation (M). The reason for this operation is that the results show a near linear relationship between the two axis after this processing which will be easier for linear or polynomial fitting.

There are 15 groups of data shown in Figure 6.5. The datasets with the spectral ranges 10 nm, 20 nm and 40 nm are shown by red, blue and green lines respectively. The dataset with the noise levels of 10 %, 20 %, 30 %, 40 % and 50 % are shown with a pentagram, asterisk, plus sign, circle and a triangle respectively. The reason that there is no data shown in Figure 6.5 with a noise level of 0 is that the signal to noise ratio is finite when the noise is 0 and the modified standard deviation was defined as $M = D/N$. D represents the standard deviation of the obtained spectral shift and N is the noise level. In this case, the standard deviation is always 0 for the noise level of 0. The reason for using modified standard deviation rather than standard deviation is that for standard deviation cannot be distinguished when the noise level is small. By dividing the noise level, the modified standard deviation can be shown in an approximated linear function although the deviation may be large for small noise levels.

By a linear fitting, a relationship between the modified standard deviation and the reciprocal of spatial frequency can be found (R^2=0.8993):

$$M = 59.2457R + 14.3808, \tag{6.11}$$

The reciprocal of spatial frequency (R) is defined as $R = 1/F$. F is the spatial frequency of the spectrum after Fourier transform which meets the threshold of $1/e$ is defined as the first spatial frequency point that is over the threshold of $1/e$ and this first point was chosen from the high frequency, beginning with half of the total spatial frequency after the Fourier transform to lower frequencies. $F = P/W$, where P is the period number in the spectral range and W is the wavelength range with the unit of nm. Along with the definition of SNR as $SNR_L = 1/N^2$, the relationship

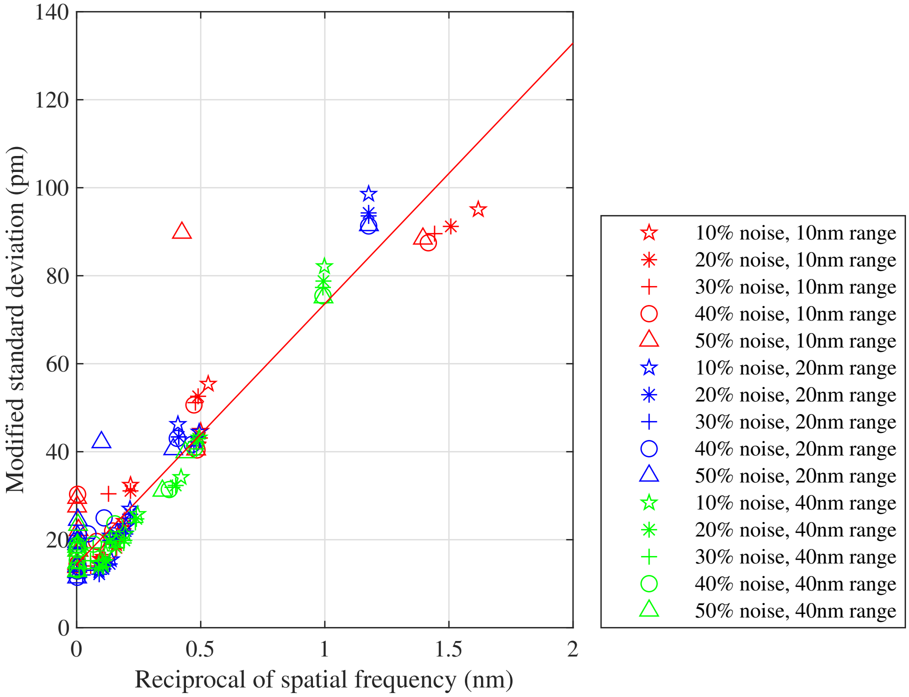

Figure 6.5: The relationship between the reciprocal of spatial frequency and the modified standard deviation of the cross-correlation method. The noise levels are 0 %, 10 %, 20 %, 30 %, 40 % and 50 %. The spectral wavelength ranges are 10 nm, 20 nm and 40 nm. The Red line shows the linear fitting results.

between the noise level, the spectral range, the gauge length, the standard deviation of the calculated spectral shift with the cross-correlation method can be expressed as:

$$D = \frac{1}{\sqrt{SNR_L}}\left[59.2457\frac{W}{P} + 14.3808\right], \tag{6.12}$$

Equation 6.12 may be used for fast evaluation of the influence of the noise level, from the spectral range for the detection, and the intended gauge lengths.

It has been shown that there is an approximately linear relationship between the period number and the gauge length. The mean spatial frequency of the cases shown in Figure 6.4 for the noise level of 0 % is shown in Figure 6.6. The response of the spatial frequency to the gauge length is about 10 nm/cm. The red line shown in Figure 6.6 shows a linear function with a slope of 10 nm/cm and passing through the origin.

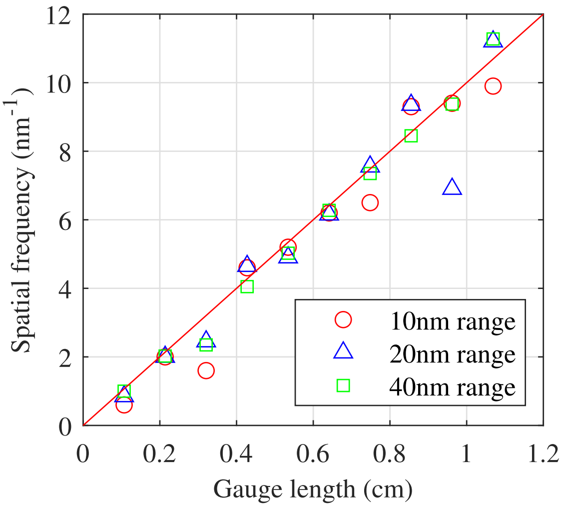

Figure 6.6: The relationship between the gauge length and the spatial frequency. The spectral wavelength ranges are 10 nm, 20 nm and 40 nm. The red line shows the tendency.

Then, with this approximated slope value, Equation 6.12 can be adjusted as (R^2=0.8602):

$$D = \frac{1}{\sqrt{SNR_L}}\left[\frac{5.9246}{L} + 14.3808\right], \tag{6.13}$$

where L is the gauge length in centimetres. It can be seen from Equation 6.13 that the standard deviation is proportional to the reciprocal of the square root of SNR. By increasing the SNR, the precision of strain detection will be improved.

If the sensitivity is defined as the value of the minimum input strain when the signal to noise ratio of strain (SNR_ε) equals 1, then a sensitivity (S) is equal to the deviation D in noise signals as

$$S = \frac{1}{\sqrt{SNR_L}}\left[\frac{5.9246}{L} + 14.3808\right]/1.24\ [\mu\varepsilon], \tag{6.14}$$

when the responsivity is set at 1.24 pm/$\mu\epsilon$.

6.4.2. STRAIN MEASUREMENT APPLICATION (AN AEROSPACE CASE)

SHM integrates sensors within structures to record damage evolution and provides information for structural integrity analysis. The integrated sensor can perform real-time monitoring of structures, and that may reduce non-destructive evaluation frequency and thus decrease maintenance cost as well as increase structural life safety, which is vital in areas such as aerospace engineering [36]. Sensors can be mounted on structures externally or embedded within structures [37]. Both internal and external sensors can be utilized for strain measurement.

Aluminium is a material widely used in aerospace engineering. FOS were integrated into an aluminium alloy part to analyse the influence of the position of the optical fibre sensor in a capillary [38]. The material of the aluminium alloy chosen was AlSi10Mg because AlSi10Mg has the advantage of good strength and low weight properties. It is often used for additive manufacturing in aircraft [39] and the specimen was manufactured with 3D printing. The embedded optical fibre sensor was used to monitor the strain information to record damage evolution and to provide information for structural integrity analysis.

In order to make a comparison between the simulated the results of the NP-doped optical fibre and commercial optical fibres, an experiment of an aerospace case was implemented to obtain real strain data. A set of experimental strain data was obtained from a commercial optical fibre sensor which was interrogated by LUNA system (ODISI-B).

Figure 6.7 shows a photo of the experimental setup used for monitoring the crack propagation with a four point bending test. The aluminium alloy part was installed on a static test machine (Zwick-10kN tensile/compression machine). The optical fibre sensor was embedded into the capillary of the aluminium alloy with injected adhesives. An initial notch was made at the middle of the bottom of the specimen. By static loading of 8 kN employed on the specimen, the crack propagated. More detail of the structure of the specimen is shown in Figure 6.8.

Figure 6.8 shows the structure of the specimen on the four point bending static test machine. There is a cylindrical capillary with a 3 mm diameter (between the white dashed lines). The centre of the capillary is about 16 mm to the bottom of the specimen. Force was applied on the top of the specimen and two holders supported the specimen under loading. The initial notch position is shown in Figure 6.8.

Generally, when the crack is generated close to the optical fibre sensor, the local stress will cause a local strain change. By analysing the local strain distribution, the crack could be monitored. Figure 6.9 shows the experimental results of strain distributions in the optical sensing fibre for different crack lengths (crack lengths: 2 mm, 4 mm, 8 mm in blue, yellow, green respectively). The data were averaged from 100 testing results. The crack length was defined as the distance between the end

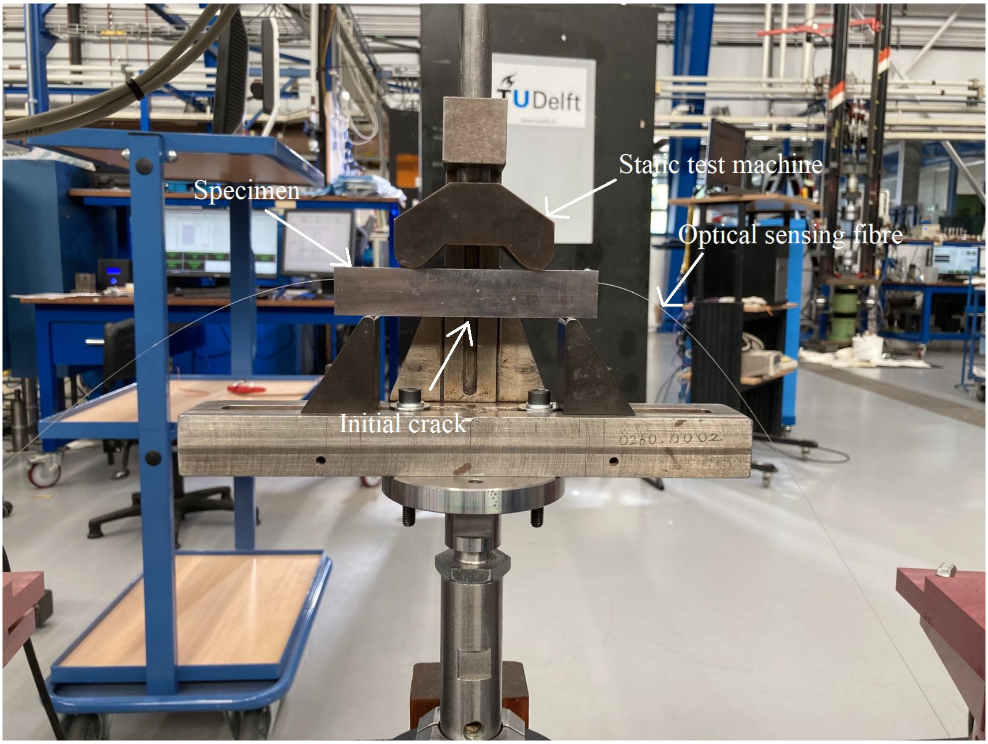

Figure 6.7: A photo of the experimental setup used for crack generation and detection. An optical fibre was embedded into the additive-manufactured aluminium alloy specimen to obtain strain data under static loading tests. The optical fibre was connected to LUNA system.

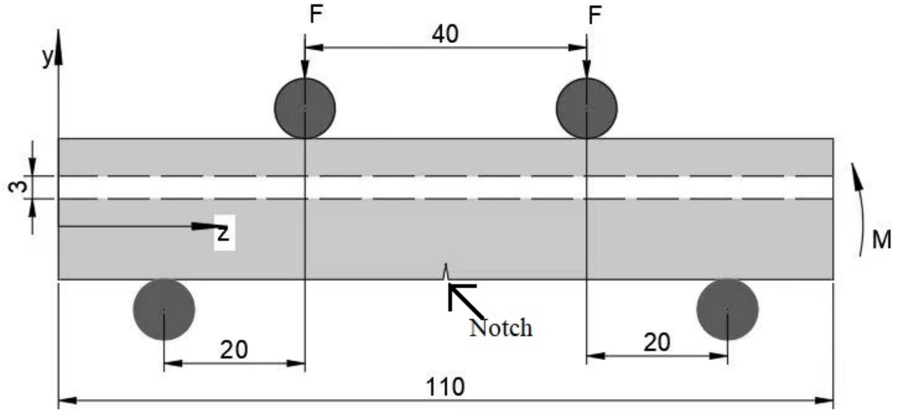

Figure 6.8: The structure of the specimen on the four point bending static test machine. The white dash hollow region is the capillary with 3 mm diameter. The optical fibre sensor was installed in the middle of the capillary but it is not shown in this figure.

of the crack to the bottom of the specimen. It can be seen that there is a peak in the middle of the sensing fibre and the peak increases when the crack propagates from 2 mm in length to 8 mm in length under load. When the crack length is small, for example 2 mm, the shape change from the original uniformed strain is quite small and it is comparable to the standard deviations (red bars). This makes it difficult to detect small cracks from the strain distribution pattern.

However, this drawback will be overcome when the backscattered light enhancement methods are used. The sensitivity of the strain sensing will increase when the backscattered light increases. By ultraviolet (UV) light exposure, the backscattered light in single mode fibre -28 (SMF-28) will increase by 20 dB [22]. With nanoparticle doping, more than 40 dB backscattered light increase has been achieved [26], [27]. The obtained standard deviations of strain from the experiment are about 11 $\mu\epsilon$ from the commercial optical fibre. From Equation 6.13, the strain standard deviations obtained from NP doped optical fibres can be lower than that obtained from commercial single mode optical fibres when the SNR_L is above 30 for gauge length of 1.3 mm and it will be easy to achieve a SNR_L of more than 30 with these backscattered light enhancement methods because of the dramatically increased backscattered light intensity.

Figure 6.10 shows a comparison between the simulated results with the sensitivity equation (Equation 6.14) and the experimental results. The black star shown in Figure 6.10 represents the experimental data point for the standard deviation of 11 $\mu\epsilon$ obtained from strain monitoring. If the photon noise obeys a Poisson distribution and the light intensity is proportional to the gauge lengths, the calibrated calculated sensitivity curve is shown in a blue line using this experimental data ($SNR_L = 30$

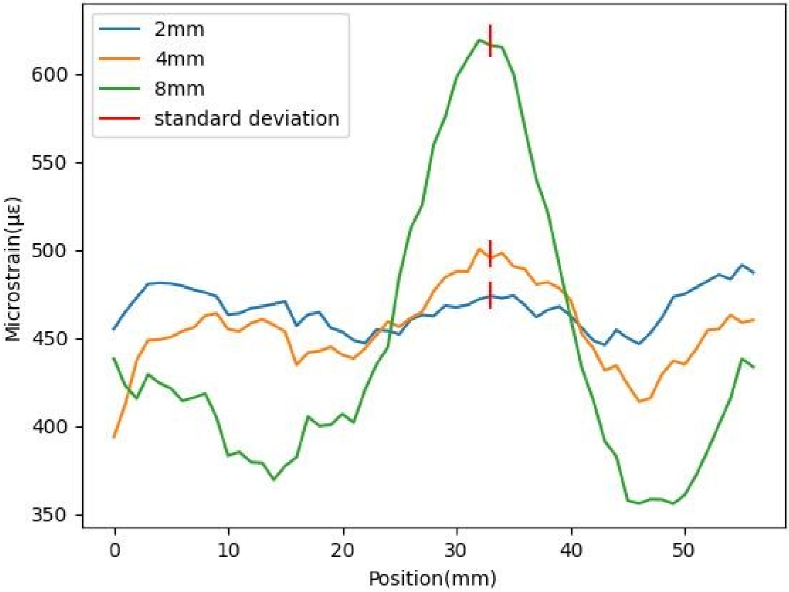

Figure 6.9: The experimental results of strain distributions in the optical sensing fibre for different crack lengths (2 mm, 4 mm and 8 mm in blue, yellow and green respectively) from LUNA ODISI-B. The crack lengths are the distances between the end of the crack to the bottom of the specimen.

for 1.3 mm gauge length). The blue circles represent the sample points that were used as typical gauge lengths in previous sections. The red triangles are the data from Loranger et al's paper [22] for SMF-28 and the calibration factor for strain and temperature used is 8.32 $\mu\epsilon/^{o}$C [22]. The sensitivity curve shows the same tendency and matches the experimental data from Loranger et al's paper [22].

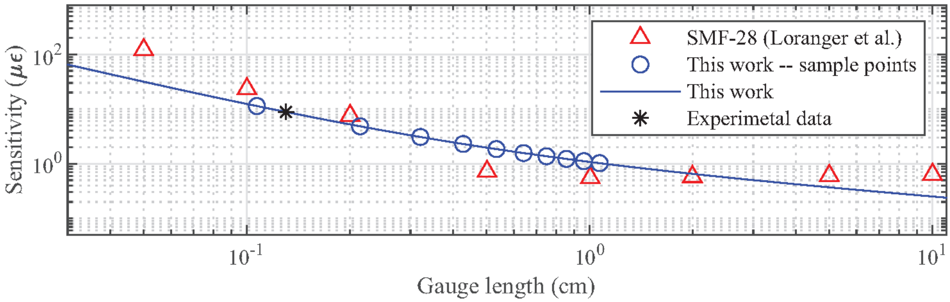

Figure 6.10: Comparison between simulated results and the experimental data. The results of single mode fibre -28 (SMF-28) [22] are in red triangles; The blue curve shows the calculated results with the sensitivity formula in this work and the blue dots show the gauge lengths used for simulations; The black star shows the experimental results from strain monitoring.

6.4.3. RESULTS OF THE NEW PROPOSED METHOD

The errors of the obtained spectral shifts are related to the spectral range as shown before (see Figure 6.4 (a)) and the period number is proportional to the spectral range [35]. Increasing the period number of the original spectrum may increase the acquisition accuracy of the spectral shift. Figure 6.11 shows the results of the proposed method with the comparison from the cross-correlation method.

The spectral range used was from 1540 nm to 1560 nm in Figure 6.11. The strain range was set at 500$\mu\epsilon$. In order to show the accuracy improvement with the proposed method compared with the traditional cross-correlation method, the error ratio was used in Figure 6.11, is defined as the ratio of the relative error between the spectral shift calculated by the proposed method and the theoretical value to the relative error between the spectral shift calculated by the cross-correlation method and the theoretical value.

One of the reasons for doping NPs into the core of the optical fibre is to increase the signal and then increase the SNR. For the SNR increased optical fibre strain sensing, the proposed method may be an easy way to improve the accuracy of the strain detection without occupying extra time-resources.

Figure 6.11 (a) and (b) show the relative errors between the results calculated with the cross-correlation method and theoretical values in blue lines with circles and the relative errors between the results calculated with the proposed method and theoretical values in red lines with stars under noise levels of 0 % and 10 % respectively. The errors decrease to half of their values for short gauge lengths when the proposed method is used. For longer gauge lengths, the improvement is not

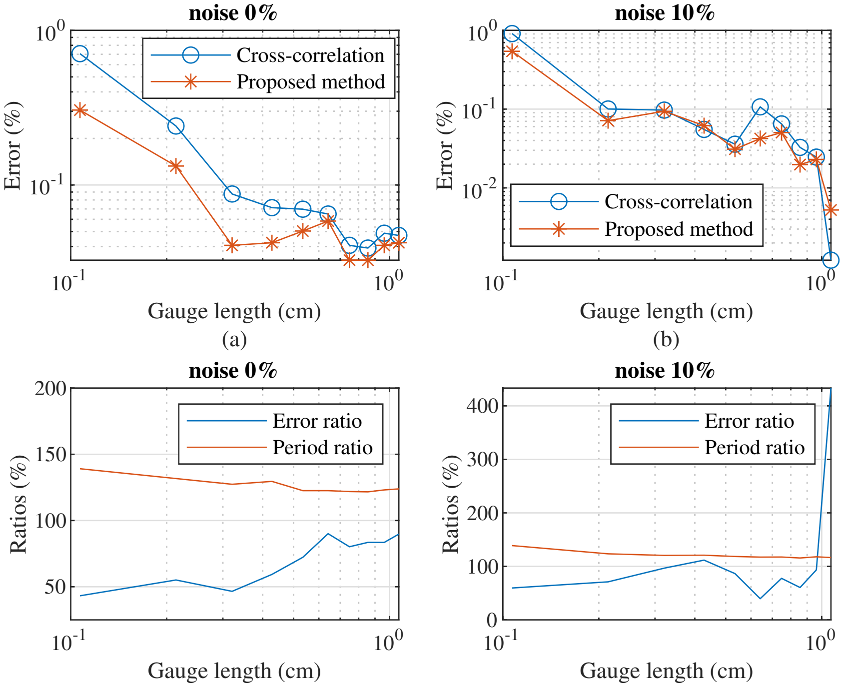

(a) (b)

(c) (d)

Figure 6.11: Comparisons between the proposed method and the traditional cross-correlation method at a strain value of 500 $\mu\epsilon$ and for a spectral range from 1540 nm to 1560 nm. The relative errors between mean values of the 100 cases and the true values with the improved cross-correlation method and traditional cross-correlation method under a noise level of (a) 0 % and (b) 10 %. The error ratios between the proposed method and traditional cross-correlation method and the corresponding period number ratios under a noise level of (c) 0 % and (d) 10 %.

noticeable.

Comparing Figure 6.11 (a) and (b), it seems that the errors are reduced at some gauge lengths when there is noise. The reason that is the theoretical result was assumed as the true value for all wavelengths but it can only be used as the theoretical result at 1550 nm incident light wavelength and the error defined is sensitive to the theoretical result that was chosen. The noise used in the simulation may shorten the mean values from the mean simulated result to the theoretical result.

To show the increase of the period numbers, the period ratio which was defined as the ratio of the period number with proposed method to the original period number is used in the red lines in Figure 6.11 (c) and (d) correspondingly. The blue lines in Figure 6.11 (c) and (d) show the error ratios between the two methods. The tendency of the error ratio is increasing when the gauge length increases and the decreasing tendency of the period ratio confirmed the idea of increasing the accuracy of the strain detection by increasing the period number with noise level 0. However, the period ratios are between 100 % and 150 %. The small increase of the period number indicates that the new characteristics of the spectra generated by the proposed method only increase the high spatial frequency components slightly and the increased high spatial frequency components have a difficulty to be distinguished from the noise if the noise level increases. Therefore, more efficient methods still need to be investigated. As shown in Figure 6.11 (d), the error ratios can be above 100 % when there is 10 % noise, which indicates that the proposed method is sensitive to noise but is beneficial to strain detection at short gauge lengths for low noise levels.

6.5. CONCLUSIONS

The sub-research question 4 (What is the effect of the sensitivity change and their effect for SHM for material?) is answered in this chapter. By increasing the signal to noise ratio of light and the gauge length, the sensitivity of the NP-doped optical fibre strain sensor will increase when the traditional cross-correlation method is used for demodulating the spectral shifts under axial strain. In addition, compared with the traditional cross-correlation method, the proposed method is a simple further step which has the ability to reduce the errors by 50 % to improve the accuracy of the spectral shift acquisition. The higher sensitivity and accuracy strain detection may be used and be beneficial for the critical positions in aircraft structures for cracks detection for SHM.

BIBLIOGRAPHY

[1] F. G. Yuan, *Structural health monitoring (SHM) in aerospace structures*. Woodhead Publishing, 2016.

[2] S. Goossens, B. De Pauw, T. Geernaert, M. S. Salmanpour, Z. S. Khodaei, E. Karachalios, D. Saenz-Castillo, H. Thienpont, and F. Berghmans, "Aerospace-grade surface mounted optical fibre strain sensor for structural health monitoring on composite structures evaluated against in-flight conditions", *Smart Materials and Structures*, vol. 28, no. 6, p. 065 008, 2019.

[3] A. J. Croxford, P. D. Wilcox, B. W. Drinkwater, and G. Konstantinidis, "Strategies for guided-wave structural health monitoring", *Proceedings of the Royal Society A: Mathematical, Physical and Engineering Sciences*, vol. 463, no. 2087, pp. 2961–2981, 2007.

[4] C. Kralovec and M. Schagerl, "Review of structural health monitoring methods regarding a multi-sensor approach for damage assessment of metal and composite structures", *Sensors*, vol. 20, no. 3, p. 826, 2020.

[5] A. Bassil, X. Chapeleau, D. Leduc, and O. Abraham, "Concrete crack monitoring using a novel strain transfer model for distributed fiber optics sensors", *Sensors*, vol. 20, no. 8, p. 2220, 2020.

[6] A. Kesavan, S. John, and I. Herszberg, "Strain-based structural health monitoring of complex composite structures", *Structural Health Monitoring*, vol. 7, no. 3, pp. 203–213, 2008.

[7] R. D. Sante, "Fibre optic sensors for Structural Health Monitoring of aircraft composite structures: Recent advances and applications", *Sensors*, vol. 15, no. 8, pp. 18 666–18 713, 2015.

[8] M. Ramakrishnan, G. Rajan, Y. Semenova, and G. Farrell, "Overview of fiber optic sensor technologies for strain/temperature sensing applications in composite materials", *Sensors*, vol. 16, no. 1, p. 99, 2016.

[9] A. Boersma, R. Cremers, and R. Jansen, "Fiber Bragg grating distributed chemical sensors", *Procedia Engineering*, vol. 168, pp. 1245–1248, 2016.

[10] M. R. Samsudin, Y. G. Shee, F. R. M. Adikan, B. B. A. Razak, and M. Dahari, "Fiber Bragg gratings hydrogen sensor for monitoring the degradation of transformer oil", *IEEE Sensors Journal*, vol. 16, no. 9, pp. 2993–2999, 2016.

[11] X. Liu, B. Jin, Q. Bai, Y. Wang, D. Wang, and Y. Wang, "Distributed fiber-optic sensors for vibration detection", *Sensors*, vol. 16, no. 8, p. 1164, 2016.

[12] S. C. M. Ho, W. Li, B. Wang, and G. Song, "A load measuring anchor plate for rock bolt using fiber optic sensor", *Smart Materials and Structures*, vol. 26, no. 5, p. 057 003, 2017.

[13] M. Froggatt and J. Moore, “High-spatial-resolution distributed strain measurement in optical fiber with Rayleigh scatter”, *Applied Optics*, vol. 37, no. 10, pp. 1735–1740, 1998.

[14] L. Fazzi, N. Dias, M. Holynska, A. Tighe, R. Rampini, and R. M. Groves, “Monitoring of silicone adhesive in space solar cells with an embedded multiparameter TFBG sensor in a simulated space environment”, *Measurement Science and Technology*, vol. 33, no. 8, p. 085 108, 2022.

[15] L. Fazzi, G. Struzziero, C. Dransfeld, and R. M. Groves, “A single three-parameter tilted fibre Bragg grating sensor to monitor the thermosetting composite curing process”, *Advanced Manufacturing: Polymer & Composites Science*, vol. 8, no. 1, pp. 33–41, 2022.

[16] W. Eickhoff and R. Ulrich, “Optical frequency domain reflectometry in singlemode fiber”, *Applied Physics Letters*, vol. 39, no. 9, pp. 693–695, 1981.

[17] Z. Ding, C. Wang, K. Liu, J. Jiang, D. Yang, G. Pan, Z. Pu, and T. Liu, “Distributed optical fiber sensors based on optical frequency domain reflectometry: A review”, *Sensors*, vol. 18, no. 4, p. 1072, 2018.

[18] J. Song, W. Li, P. Lu, Y. Xu, L. Chen, and X. Bao, “Long-range high spatial resolution distributed temperature and strain sensing based on optical frequency-domain reflectometry”, *IEEE Photonics Journal*, vol. 6, no. 3, pp. 1–8, 2014.

[19] S. T. Kreger, O. J. Ohanian III, N. Garg, M. A. Castellucci, D. Kominski, N. A. A. Rahim, M. A. Davis, N. B. Beaty, J. W. Jeans, E. H. Templeton, *et al.*, “Optical frequency domain reflectometry for aerospace applications”, in *Fiber Optic Sensors and Applications XIV*, International Society for Optics and Photonics, vol. 10208, 2017, p. 1 020 803.

[20] Y. Shan, H. Xu, Z. Zhou, Z. Yuan, X. Xu, and Z. Wu, “State sensing of composite structures with complex curved surface based on distributed optical fiber sensor”, *Journal of Intelligent Material Systems and Structures*, vol. 30, no. 13, pp. 1951–1968, 2019.

[21] H. Murayama, D. Wada, and H. Igawa, “Structural health monitoring by using fiber-optic distributed strain sensors with high spatial resolution”, *Photonic Sensors*, vol. 3, no. 4, pp. 355–376, 2013.

[22] S. Loranger, M. Gagné, V. Lambin-Iezzi, and R. Kashyap, “Rayleigh scatter based order of magnitude increase in distributed temperature and strain sensing by simple UV exposure of optical fibre”, *Scientific Reports*, vol. 5, no. 1, pp. 1–7, 2015.

[23] P. Lu, S. J. Mihailov, D. Coulas, H. Ding, and X. Bao, “Low-loss random fiber gratings made with an fs-IR laser for distributed fiber sensing”, *Journal of Lightwave Technology*, vol. 37, no. 18, pp. 4697–4702, 2019.

[24] F. Parent, S. Loranger, K. K. Mandal, V. L. Iezzi, J. Lapointe, J. S. Boisvert, M. D. Baiad, S. Kadoury, and R. Kashyap, “Enhancement of accuracy in shape sensing of surgical needles using optical frequency domain reflectometry in optical fibers”, *Biomedical Optics Express*, vol. 8, no. 4, pp. 2210–2221, 2017.

[25] V. Fuertes, N. Grégoire, P. Labranche, S. Gagnon, R. Wang, Y. Ledemi, S. LaRochelle, and Y. Messaddeq, “Engineering nanoparticle features to tune Rayleigh scattering in nanoparticles-doped optical fibers”, *Scientific Reports*, vol. 11, no. 1, pp. 1–12, 2021.

[26] D. Tosi, C. Molardi, and W. Blanc, “Rayleigh scattering characterization of a low-loss MgO-based nanoparticle-doped optical fiber for distributed sensing”, *Optics & Laser Technology*, vol. 133, p. 106 523, 2021.

[27] V. Fuertes, N. Grégoire, S. Morency, S. Gagnon, Y. Ledemi, S. LaRochelle, and Y. Messaddeq, “Tunable distributed sensing performance in Ca-based nanoparticle-doped optical fibers”, *Optical Materials Express*, vol. 12, no. 4, pp. 1323–1336, 2022.

[28] X. Wang, R. Benedictus, and R. M. Groves, “Optimization of light scattering enhancement by gold nanoparticles in fused silica optical fiber”, *Optics Express*, vol. 29, no. 13, pp. 19 450–19 464, 2021.

[29] V. Ewald, R. M. Groves, and R. Benedictus, “Transducer placement option of Lamb wave SHM system for hotspot damage monitoring”, *Aerospace*, vol. 5, no. 2, p. 39, 2018.

[30] H. Murayama, K. Ohara, N. Kanata, K. Kageyama, and H. Igawa, “Strain monitoring and defect detection in welded joints by using fiber-optic distributed sensors with high spatial resolution”, *E-Journal of Advanced Maintenance*, vol. 2, no. 3, pp. 191–199, 2011.

[31] M. Zhu and H. Murayama, “Fast demodulation of OFDR based long length FBG sensing system for noisy signals”, *Optics Express*, vol. 26, no. 16, pp. 19 804–19 814, 2018.

[32] S. T. Kreger, A. K. Sang, D. K. Gifford, and M. E. Froggatt, “Distributed strain and temperature sensing in plastic optical fiber using Rayleigh scatter”, in *Fiber Optic Sensors and Applications VI*, International Society for Optics and Photonics, vol. 7316, 2009, 73160A.

[33] Z. Guo, J. Yan, G. Han, D. Greenwood, J. Marco, and Y. Yu, “High sensing accuracy realisation with millimetre/sub-millimetre resolution in optical frequency domain reflectometer”, *Journal of Lightwave Technology*, vol. 40, no. 12, pp. 4050–4056, 2022.

[34] Z. Zhou, C. Chen, P. Lu, S. Mihailov, L. Chen, and X. Bao, “Random fiber grating characterization based on OFDR and transfer matrix method”, *Sensors*, vol. 20, no. 21, p. 6071, 2020.

[35] X. Wang, R. Benedictus, and R. M. Groves, “Spectral characteristics of gold nanoparticle doped optical fibre under axial strain”, *Scientific Reports*, vol. 12, no. 1, p. 16 593, 2022.

[36] D. Inaudi and B. Glisic, *Fibre optic methods for structural health monitoring*. John Wiley & Sons, 2008.

[37] F. K. Chang, J. F. C. Markmiller, J. Yang, and Y. Kim, *Structural Health Monitoring*. John Wiley & Sons, 2011, ch. 26, pp. 419–428.

[38] Y. Xiao, C. Rans, D. Zarouchas, and R. Benedictus, “Measurement accuracy of distributed sensing fibers embedded within capillaries of solid structures”, in *12th International Workshop on Structural Health Monitoring: Enabling Intelligent Life-Cycle Health Management for Industry Internet of Things (IIOT), IWSHM 2019*, DEStech Publications Inc., 2019, pp. 1645–1652.

[39] K. Kempen, L. Thijs, J. Van Humbeeck, and J. P. Kruth, “Mechanical properties of AlSi10Mg produced by selective laser melting”, *Physics Procedia*, vol. 39, pp. 439–446, 2012.

7

PLASMON RESONANCE BASED GOLD NANOPARTICLE DOPED OPTICAL FIBRE STRAIN SENSING

Due to the use of metal nanopaticles in the optical fibres, the metal nanoparticles introduce localised plasmon resonance phenomenon. For spherical gold nanoparticles, the absorption peaks occur in the visible or near infrard light range based on the particles' sizes. The shape of the nanoparticles also lead to the changes in the absoption peaks. When strain changes, will the plasmon resonance spectral peak shift? How is the spectral peak shift under strain? In this chapter, the plasmon resonance spectral peaks in the gold nanoparticle-doped optical fibres under axial strain was discussed.

Parts of this chapter have been published in Optics & Laser Technology **159**, (2022): 108272.

GOLD nanoparticle (NP) doped fibre optic sensors not only have the potential to increase the intensity of the backscattered signal to increase the signal to noise ratio but also have plasmon resonance peaks in the visible light range. The spectral peak shift of the plasmon resonance may be used for strain sensing. In this chapter, the spectral peak shift of the plasmon resonance of an optical fibre containing gold NPs under axial strain was analysed. A modified Lorentz-Drude (LD) model with the T-matrix method was used and the spectral peak shifts of spheroidal NPs under strain were calculated. An approximate analytical expression was derived for faster calculation. The modelling presented in this chapter shows that the ratio of the change of the peak wavelength to the strain can be related to the refractive index (RI) change of the optical fibre under strain, the shape change of the gold NP, and the RI change of the gold NP. The peak shift was also observed experimentally in an optical adhesive containing gold NPs under compression. The peak shifts were analysed at different RI of the optical fibres, 1.35, 1.45, 1.55 and 1.65 respectively, in order to cover the range of RI of fused silica and some polymer materials. The results confirm experimentally that the applied axial strain can induce the peak wavelength shift by the NPs. By choosing a different optical fibre or the properties of the NPs, the wavelength change ratio has the potential to be tuned, which may be used for highly sensitive strain sensing. This chapter is related to the main research question: how can the enhancement of light scattering used in distributed fibre optic sensing be an advantage for SHM?

7.1. INTRODUCTION

In recent years, nanoparticle (NP) doped optical fibre sensing has attracted the interest of researchers [1]–[4] because the doped NPs in the core of the optical fibre enhance the backscattered light dramatically. The enhanced backscattered signal is beneficial to the signal to noise ratio for strain detection. Gold is one of the potential materials for NP doped fibre optic sensing due to its high backscattering properties [5]. Gold NPs not only increase the intensity of backscattered light but also have a high extinction for light transmission, which is caused by localized surface plasmon resonance (LSPR) [6]. Surface plasmon resonance (SPR) a phenomenon caused by the resonance of free electrons in a metal due to an incident light wave. Gold as a metal can be used as the material for SPR. There are several applications for optical fibre sensors based on the SPR of gold. For example, coating a thin gold layer on optical fibres to achieve twist detection [7], [8] or to achieve high sensitive flow rate detection [9] or to achieve refractive index (RI) detection [10]. Gold NPs as metallic NPs have small geometric size compared with the wavelengths of visible light in all spatial dimensions. Therefore, the SPR for gold NPs is localized. The SPR based sensors may have advantages in some applications for example higher RI sensitivity compared with LSPR based sensors [11]. However, the sensitivity based on LSPR is tunable based on the shape of the NPs. In this circumstance, tunable sensitivity strain sensing may be achieved via detecting transmitted light in the visible light range (generally the plasmon resonance peak is in the visible light range for small size spherical gold NPs [12]) with an optical fibre containing gold NPs in the core. The wavelength range can be different from that used for distributed fibre optic sensing strain detection, for example the light wavelengths for LUNA ODiSI-B are around 1550 nm in near-infrared wavelength range. Previous research has shown that the RI of the gold NP will change under strain change [13]–[15]. Along with the shape change of the NPs and the RI change of the optical fibre, the resonance peak may shift. Therefore, doping gold NP into the core of the optical fibre may have the potential for strain detection based on the plasmon resonance peak shift in the visible light range. Therefore, it may be an auxiliary strain detection method along with distributed fibre optic sensing based on Rayleigh scattering in different wavelength ranges. However, the behaviour of the peak wavelength change under strain change along optical fibre has not yet been fully studied.

In this work, the strain sensing feasibility of gold NP doped optical fibre will be investigated using analytical expressions, simulations and experiments. First the modified Lorentz-Drude model is proposed to show the RI change of spherical gold NP under strain change. Then, based on the modified Lorentz-Drude (LD) model and the T-matrix method (also called the extended boundary-condition method (EBCM) method) [16], [17] for light scattering by spheroidal NP, the plasmon resonance peak shift will be calculated in optical fibres with RI of 1.35, 1.45, 1.55 and 1.65 respectively. The case for gold NPs in an optical adhesive and in fused silica optical fibre will be calculated specifically and the former will be demonstrated experimentally. Finally, as the formula for the calculation of the resonance wavelength shift is complex and time-consuming, a simplified analytic formula will be used, which is based on the formula for small NP extinction cross section, but only considering its main factors, in order to show the wavelength shift tendency.

7.2. THEORY

Figure 7.1 shows the modelled structure. 100 nm size gold NPs are doped inside the core of the optical fibre over a short distance (several millimetres length). To make it clear, there is only one NP shown in the figure to illustrate the theory of the sensing method. Cartesian coordinates are defined as shown in Figure 7.1. The Z axis is along the optical fibre and it is also the light transmission direction. The electrical field of the incident light is defined to be along the X direction.

Light is emitted from a broad band visible light source (for example a halogen lamp to cover the light wavelength range of the plasmon resonance of the NPs) and then light is coupled into the left side of the optical fibre. The gold NP is shown in Figure 7.1 in blue. The original status (without strain change) of the sensor is shown, not to scale, in Figure 7.1 (a). The shape of the NP is spherical with a radius R (50 nm). Figure 7.1 (b) shows the case of the sensor under axial strain. The length of the optical fibre is changed from l to $l+\Delta l$. If the material property of the optical fibre is isotropic and the gold NP is also approximated as an isotropic material because the elastic anisotropy index of gold is small [18], then the spherical gold NP changes its shape to a spheroidal NP. The half axis of the spheroid along the optical fibre changes from R to $R_z \equiv a \equiv R + \Delta R_z$. The half axis along the X and Y axis have the same values as $R_x = R_y$ and $R_x \equiv b \equiv R + \Delta R_x$ and $R_y \equiv c \equiv R + \Delta R_y$. $\Delta R_x = \Delta R_y$ and $b = c$.

Light will be extincted by the NPs which induces the plasma resonance peak due

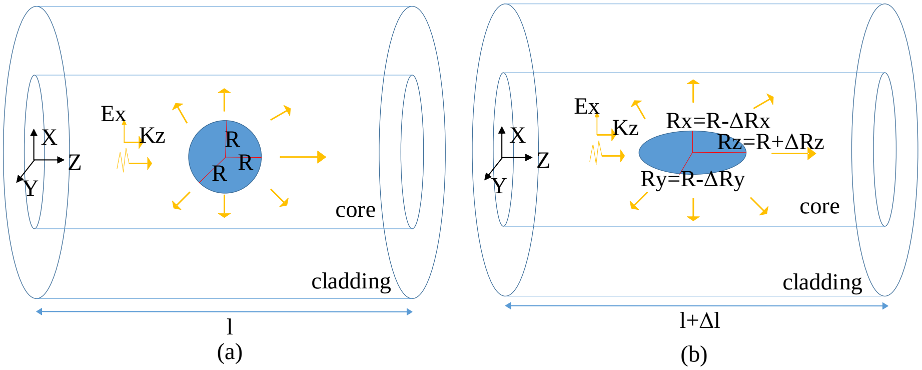

Figure 7.1: Light extinction by the gold NP in the optical fibre. (a) Case of original status. (b) Case of strain change.

to the LSPR. The LSPR is caused by the coherent oscillation of free electrons [6], [19] and it changes when the shape of the NP change [6], [20]. The propagating light after extinction is then detected by a spectrometer which is connected to the right side of the optical fibre. By determining the peak wavelength shift of the absorbance spectra, strain change values may be obtained.

To describe the shape change of the NP clearly in the optical fibre, the relative strain change along the optical fibre (α) between the NP and the optical fibre is defined as:

$$\alpha = \frac{\Delta R_z}{R} / \frac{\Delta l}{l}. \tag{7.1}$$

The shape change of the NP (β) is defined as:

$$\beta = \frac{\Delta R_t}{\Delta R_z}, \ (t = x, y), \tag{7.2}$$

which is similar to the definition of the Poisson's ratio [21].

The shape and the RI change of the NPs will induce the plasmon resonance peak change. In addition, the plasmon resonance peak is also influenced by the RI of the optical fibre. Therefore, the peak wavelength shift of the absorbance spectra under strain is a formula including these parameters.

To describe the influence by these parameters, in the following paragraphs, the RI for gold NP, the RI change of gold NP based on the modefied LD model under strain change and the plasmon resonace wavelength and the wavelength shift under strain change will be analysed. The reason for using the LD model is that the LD model is a sum of the expressions of the oscillators and may generate a simpler analytic equation for the spectra shift under strain.

7.2.1. MODIFIED LORENTZ-DRUDE MODEL FOR GOLD NP UNDER STRAIN

Two parts constitute the permittivity of gold. They are free charge component (ϵ_{free}) and bound charge component (ϵ_{bound}) [22]. The permittivity of gold can be expressed as:

$$\epsilon_{Au} = \epsilon_{free} + \epsilon_{bound}. \tag{7.3}$$

For nanometer size gold NPs, Scaffardi and Tocho's model has a good match with the experimental data for nanometer size gold NPs as low as 0.6 nm diameter gold NP [22] and also has a good match with the RI of bulk gold. See the experimental data from Johnson and Christy's experiment [23] (blue stars) and the RI calculated by Scaffardi and Tocho's model (red solid lines) shown in Figure 7.2. n is the real part of the RI and k is the imaginary part of RI. The red dashed lines show the real and imaginary part of RI of a 100 nm size gold NP to give an intuitive deviation of RI for small size of gold and the deviation becomes smaller when the size of the NPs increases.

With Scaffardi and Tocho's model the free charge component of the permittivity of gold can be expressed as:

$$\epsilon_{free}(\omega) = 1 - \frac{\omega_p^2}{\omega^2 + i(\gamma_{bulk+H\frac{v_F}{R}})\omega}, \tag{7.4}$$

where, ω is the angular frequency of light in vacuum, ω_p is the bulk plasma frequency of gold, γ_{bulk} is the damping constant for free electrons, H is a scattering constant, v_F is the electron velocity at the Fermi surface, and R is the radius of the gold particle [5], [22]. Equation 7.4 is an expression about R and ω. Figure 7.3 (a) and (b) show the deviation of the real part of free charge component of the permittivity and imaginary part of free charge component of the permittivity to the free charge component of the permittivity bulk gold respectively. The imaginary part is more influenced by the radius R than the real part.

The bound charge component of the permittivity of gold can be expressed as

$$\epsilon_{bound}(\omega) = Q_{bulk}[1 - \exp(-\frac{R}{R_0})]G(\omega), \tag{7.5}$$

where,

$$G(\omega) = \int_{\omega_g}^{\infty} \frac{\sqrt{\omega' - \omega_g}}{\omega'}[1 - F(\omega', T)] \frac{\omega'^2 - \omega_g^2 + \gamma_b^2 + i2\omega\gamma_b}{(\omega'^2 - \omega_g^2 + \gamma_b^2)^2 + 4\omega^2\gamma_b^2} \mathrm{d}\omega', \tag{7.6}$$

where, the parameter $Q_{bulk} = 2.3 \times 10^{24}$, ω' is the angular frequency in the integral equation, $R_0 = 0.35\,\mathrm{nm}$, $\omega_g = 3.19 \times 10^{15}\,\mathrm{Hz}$ is the angular frequency of the gap energy of gold, $F(\omega, T)$ corresponds to the Fermi energy distribution, k_b is the Boltzmann constant, $E_f = 2.5\,\mathrm{eV}$ is the Fermi energy and γ_b corresponds to the damping constant of bound electrons of gold (refer to [5], [22]).

The bound charge component of the permittivity of gold is an formula with R and ω (see Equations 7.5 and 7.6). However, the modification caused by R is quite small for large size NPs (>100 nm diameter) and the modification of $(1 - \exp(-\frac{R}{R_0}))$ is less than 9.08×10^{-61} % because R_0 is only 0.35 nm and the bound charge component will change only when the diameters of the NP are in the several nanometer or smaller size. For example, when the size of the gold NP is 1 nm, this modification is

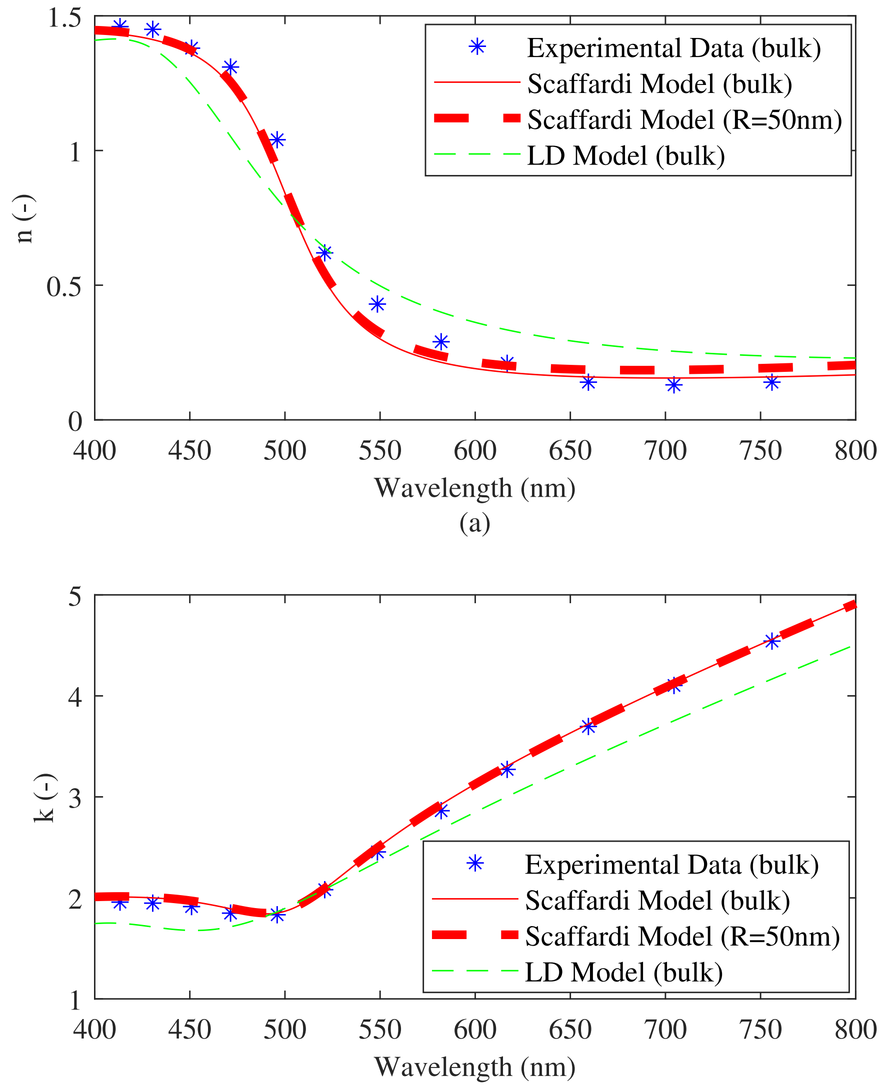

(a)

(b)

Figure 7.2: The RI of gold. (a) The real part of the RI (n). (b) The imaginary part of the RI (k).

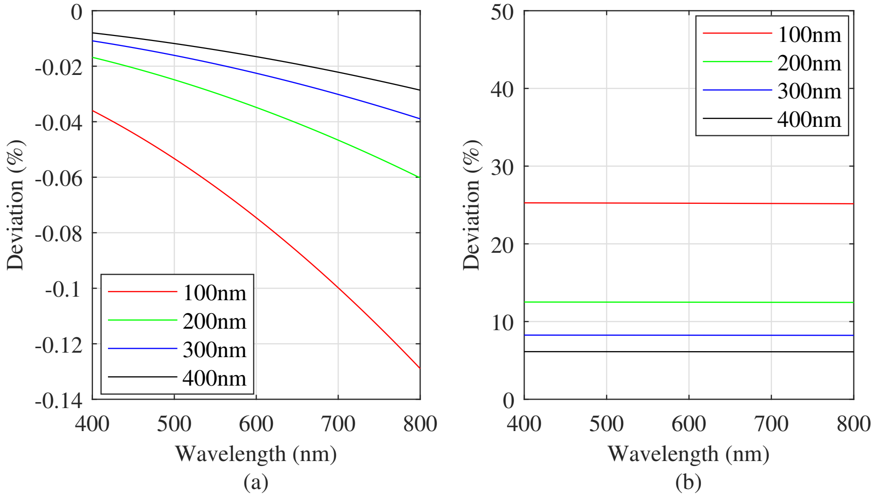

(a)

(b)

Figure 7.3: The deviation of contribution of the permittivity of free-charge between gold NP and bulk gold. (a) The deviation of the real part. (b) The deviation of the imaginary part.

about 76.0 %. Therefore, the influence of the bound charge component of the permittivity caused by R can be neglected compared with the deviation of the free charge component (see Figure 7.3). As shown in Figure 7.2, the RI of the gold NP with diameter of 100 nm calculated from the permittivity via Scaffardi and Tocho's model is close to the RI of bulk gold. Therefore, the permittivity may vary for different radii of NPs can be expressed as:

$$\epsilon_{Au}(R,\omega) = \epsilon_{free}(R,\omega) + \epsilon_{bound}(\omega), \tag{7.7}$$

However, the Scaffardi and Tocho's model was not chosen to obtain the approximate analytical expression of the spectral peak shift in this chapter because the bound charge component of the permittively is complicated. The simpler model, the LD model, assuming the bound charge component of the permittively is caused by a lot of oscillators [20] was used for the concise expression. According to the LD model, for bulk gold the permittivity of gold can be expressed as [24]:

$$\epsilon_{Au-LD} = 1 - \frac{f_0\omega_{p0}^2}{\omega(\omega + i\Gamma_0)} + \sum_{j=1}^{k} \frac{f_j\omega_{p0}^2}{(\omega_j^2 - \omega^2) - i\omega\Gamma_j}, \tag{7.8}$$

where ω_{p0} is the plasma frequency of gold, ω is the angular frequency of the incident light in vacuum, ω_j is the resonance frequency of the jth oscillator, Γ_0 is the damping constant of the free electron, Γ_j is the damping constant of the jth oscillator. f_0 and f_j can be obtained by fitting the experimental permittivity data. The tendency of the RI also matches well with the experimental data (see Figure 7.2 blue stars and green dashed lines).

When the R equals infinite large, the bound charge component of the permittively can be expressed as:

$$\epsilon_{bound}(\omega) = \epsilon_{Au-LD} - \epsilon_{free}(R \to \infty), \tag{7.9}$$

where,

$$\epsilon_{free}(R) = 1 - \frac{\omega_p^2}{\omega^2 + i\gamma(R)\omega}, \tag{7.10}$$

where, ω_p is the plasma frequency of gold and γ is the damping constant of the free electron,

$$\gamma(R) = \gamma_0 + A\frac{v_F}{L_{eff}(R)}, \tag{7.11}$$

and

$$L_{eff}(R) = 4\frac{V}{S} = \frac{4R}{3}, \tag{7.12}$$

where, L_{eff} is the reduced effective mean free path, v_F is the Fermi velocity, V is the volume of the NP and S is the surface area of the NP [13].

When the strain changes, the shape of the spherical NP will become spheroidal and the density of the electrons will change. The plasma frequency is related to the electron density,

$$\omega_p = \sqrt{\frac{Ne^2}{\epsilon_0 m_{eff}}}, \tag{7.13}$$

where, N is the electron density, e is the electron charge, ϵ_0 is the vacuum dielectric constant and m_{eff} is the effective electron mass. v_F can also be influenced by the electron density as

$$v_F = \sqrt{\frac{2E_F}{m}}, \tag{7.14}$$

where

$$E_F = \frac{h^2}{2m}\left(\frac{3}{8\pi}\right)^{2/3} N^{2/3}, \tag{7.15}$$

h is the Planck constant, E_F is the Fermi energy, m is the mass of electron and for face centred cubic (FCC) structure metals.

$$N = \frac{4}{a_0^3}, \tag{7.16}$$

where a_0 is the lattice constant of gold [13], which corresponds to the electron density before strain change. When the volume ratio is introduced to describe the density change, the electron density under strain change becomes:

$$N' = N \times \frac{V}{V'}, \tag{7.17}$$

where V' is the volume of the gold NP under strain and $V' = 4\pi abc/3$. The surface area of the gold NP becomes $S' = 4\pi(ab + bc + ac)/3$. The strain will not only change the permittivity of the free-charge contribution but it will also change the permittivity of the bound-charge of the NP because of the electron density change [13]. Therefore, Equation 7.9 needs to be modified by strain as:

$$\epsilon_{bound}(\omega) = \epsilon_{core}(\omega) - 1, \tag{7.18}$$

and ϵ_{core} is replaced by ϵ_c when the shape of the NP change:

$$\epsilon_c(\omega) = \frac{\epsilon_{core}(\omega) + 2 + 2\nu(\epsilon_{core}(\omega) - 1)}{\epsilon_{core}(\omega) + 2 - \nu(\epsilon_{core}(\omega) - 1)}, \tag{7.19}$$

where ϵ_{core} is the permittivity of the core part and the volume change ratio $\nu = R^3/abc$.

Therefore, by introducing strain related permittivity components, the modified LD model under strain change may eventually be expressed as:

$$\epsilon_{Au}(R) = \epsilon_{free}(R) + \epsilon_c(\epsilon_{core}) - 1, \tag{7.20}$$

where,

$$\epsilon_{core} = \epsilon_{Au-LD} - \epsilon_{free}(R \to \infty). \tag{7.21}$$

7.2.2. PLASMON RESONANCE WAVELENGTH SHIFT OF GOLD NP

By acquiring the wavelength of the extinction cross section (C_{ext}), the plasmon resonance wavelength can be obtained. The extinction cross section of the NP can be calculated by Mie theory for spherical NPs [20] or by the T-matrix method for spheroidal NPs [17], [25], [26].

According to Mie theory [20], for a spherical particle,

$$C_{ext} = \frac{2\pi}{k^2} \Re \sum_n (2n+1)(a_n + b_n), \tag{7.22}$$

where, k is the wave vector in the medium. $\Re$ is the symbol of the real part, and a_n and b_n are the scattering coefficients.

The T-matrix method also expands the field in terms of vector spherical wave function which is similar to Mie theory [17]. By constituting the relationship between the incident wave and the scattering wave with the matrix T as [27]:

$$\begin{bmatrix} p_\nu \\ q_\nu \end{bmatrix} = T \begin{bmatrix} a_\nu \\ b_\nu \end{bmatrix}, \tag{7.23}$$

where, p_ν and q_ν are the coefficients of the expanded scattered wave, a_ν and b_ν are the coefficients of the expanded incident wave, the subscript $\nu = (m, n)$ and $|m| \leq n$. and solving matrix T by integrating the vector spherical function on the particle's surface[28], the scattering and absorption by the NP can be calculated. According to the T-matrix method for a spheroidal particle [25],

$$C_{ext} = \frac{-1}{k^2} \sum_\nu (p_\nu^* a_\nu + q_\nu^* b_\nu), \tag{7.24}$$

For more information about solving Equation 7.24 and T-matrix refer to [25].

The method of using the T-matrix method along with fitting the plasmon resonance wavelengths under different strains values to obtain the peak shift values is generally time-consuming. Therefore, the high performance computing (HPC) cluster of the Aerospace Structures and Materials (ASM) department of Delft University of Technology was used to accelerate the calculation. The aimed NPs sizes are relatively small (100 nm) when compared with the incident visible light wavelengths (around 600 nm), so in the following part the small size assumptions for the extinction of the NPs are used in order to attempt to obtain a simpler analytical solution of the plasmon resonance wavelength shift.

Calculating the spectrum of the extinction of the spheroidal NPs is generally time-consuming under different strain values even with HPC clusters with T-matrix method. However, the size of NPs considered in this chapter (100 nm) is smaller compared with the incident wavelengths (>500 nm). In this circumstance, the small extinction cross section may be used to simplify the calculation by deriving an approximate analytical expression to achieve fast calculation.

For small spheroidal NPs [20] ($b = c$) compared with the incident light, the polarizabilities α_1 and α_2 for parallel X axis and Y axis electrical field can be expressed as

$$\alpha = \alpha_1 = \alpha_2 = 4\pi abc \frac{\epsilon_{Au} - \epsilon_m}{3\epsilon_m + 3L(\epsilon_{Au} - \epsilon_m)}, \tag{7.25}$$

where, $L = 1/3$ for a spherical NP [20]. For small size NPs, the extinction cross section may be expressed as

$$C_{ext} = k\Im(\alpha) = 4\pi abck\Im\left(\frac{\epsilon_{Au} - \epsilon_m}{3\epsilon_m + 3L(\epsilon_{Au} - \epsilon_m)}\right), \tag{7.26}$$

where, $\Im$ is the symbol of the imaginary part.

When $\Re[3\epsilon_m + 3L(\epsilon_{Au} - \epsilon_m)] = 0$, the approximate plasmon resonance frequency, is obtained by solving the equation

$$\Re\epsilon_{Au}(\omega_{Fv}) = \epsilon_m\left(1 - \frac{1}{L}\right), \tag{7.27}$$

where ϵ_m is the permittivity of the medium which can be expressed as

$$\epsilon_m = \epsilon_{m0}(1 + \eta\frac{\Delta l}{l})^2, \tag{7.28}$$

and η is the strain induced RI change of the medium.

The solution of Equation 7.27 is ω_{Fv} which is the well-known Fröhlich frequency if $\Re\epsilon_{Au}$ satisfies Equation 7.27 and $\Im\epsilon_{Au} \approx 0$. For a spherical NP with $L = 1/3$, Equation 7.27 changes to $\Re\epsilon_{Au} = -2\epsilon_m$.

When the strain changes, the spectral peak calculated by Equation 7.27 will shift. Equation 7.27 is an implicit function of the spectral peak wavelength and the strain. The derivative of wavelength shift under strain can be calculated from the implicit function as a function of F

$$F = \Re\epsilon_{Au}(R) - \epsilon_m\left(1 - \frac{1}{L}\right). \tag{7.29}$$

Then, the peak wavelength shift can be obtained from

$$\left[\frac{\mathrm{d}\omega}{\mathrm{d}l/l}\right]_{\omega_{Fv}} = -\left[\frac{\mathrm{d}F/(\mathrm{d}l/l)}{\mathrm{d}F/\mathrm{d}\omega}\right]_{\omega_{Fv}}, \tag{7.30}$$

in angular frequency or can be expressed in wavelength as

$$\left[\frac{\mathrm{d}\lambda}{\mathrm{d}l/l}\right]_{\lambda_0} = \left[\frac{\lambda^2}{2\pi c'}\frac{\mathrm{d}F/(\mathrm{d}l/l)}{\mathrm{d}F/\mathrm{d}\omega}\right]_{\lambda_0}, \tag{7.31}$$

where c' the velocity of light in vacuum. The further approximation of Equations 7.30 and 7.31 are shown in the Results sections (see Equations 7.33, 7.34 and 7.35).

7.3. METHODS

7.3.1. EXPERIMENTAL METHODOLOGY

Gold NP suspension (100 nm NP diameter, stabilized suspension in citrate buffer, 3.45×10^9- 4.22×10^9 ml^{-1}, Sigma Aldrich) was put into a plastic tube and the water was evaporated at about 80°C. When the liquid of the gold NP suspension had been evaporated, 1 ml optical adhesive (146H, Norland Products) was added to the tube and then stirred by an ultrasonic processor (750 Watt, Cole-Parmer) for 3 min. During each minute the ultrasonic processor worked for 5 sec with 30 % of its total power. After the stirring process, part of the gold NP suspension was mixed into the optical adhesive. The optical adhesive containing gold NPs was then dropped onto two optical fibre end tips and cured by ultraviolet light using an ultraviolet lamp (PH135 SX Super Xenon, LABINO AB). Figure 7.4 shows a photo of the optical end tips part of the experimental setup with the optical adhesive cured by the ultraviolet lamp. A USB (universal serial bus) microscope was put beside the optical fibre end tips to view the position change of the optical fibre end tips under pressure. The optical fibre end tips were made by connectors (30640G3, ϕ 640 µm bore, Thorlabs) with multimode optical fibre (FP600ERT, 0.50 NA, ϕ 600 µm core, Low OH, Thorlabs) and were fixed on a 3-axis stage (MAX373D, Thorlabs). The upper optical fibre was connected to a broad band light source (Tungsten Halogen light source, Ocean Optics). The light propagated along the optical fibre to the upper optical fibre end tip and then went through the optical adhesive to the lower optical fibre and was finally detected by a spectrometer (Cobra Vis, Wasatch Photonics, about 100 pm resolution). When adjusting the Z direction along the optical fibre, the upper optical fibre end tip lowered its position and the lower optical fibre was fixed, so the cured optical adhesive was slightly compressed. Obtaining the spectrum without sample compression is used as the reference spectrum to obtain the peak absorbing wavelength. Then compressing the cured optical adhesive in Z direction and obtaining the corresponding absorbing spectra. By analysing the absorbance peak wavelengths obtained by the spectrometer under compression, the relationship between the Z displacement and the absorbance peak wavelengths can be obtained. The accuracy of the position adjusting of the stage in Z direction is 1 µm. The relative positions of the two optical fibre end tips were recorded by reading the Z direction change from the stage. However, when the optical adhesive

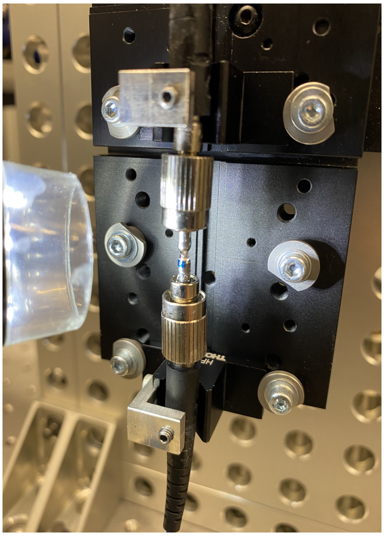

Figure 7.4: Photo of the experimental setup.

is in compression, the force on the optical adhesive will cause a deviation of the real relative positions of the two optical fibre end tips to the values read from the stage's micrometer, especially when the pressure is high. Therefore, a microscope was used to correct the relative position change. By obtaining the images from the microscope, the size of the ferrule of the optical fibre was obtained first for calibration. The relative positions of the two optical fibre end tips were then obtained by measuring the distances between the centres of the two end tips.

7.3.2. NUMERICAL METHODOLOGY

For the cases of 100 nm size gold NPs in the optical adhesive and in the fused silica, the shape of the NP change was obtained using the finite element method (FEM) with the software Abaqus CAE 2019 (Dassault Systèmes). It is assumed that in the modelling region, there is only one NP and the NP is in the centre of model. The perfect contact condition was used for the interfaces of NPs and the optical fibre. The parameters of the spheroidal NP obtained from the FEM by Abaqus were then used for the simulation in the software MATLAB 2019a (The MathWorks) with the T-matrix method to calculate the extinction cross sections in visible light range around the plasmon resonance wavelengths on the HPC cluster. The plasmon resonance wavelengths under different strain values can be obtained using Equation 7.24 to obtain the extinction spectrum first and then by fitting the peak of the spectra of the extinction cross section, the plasmon resonance wavelengths under different strain values can be obtained. The parameters for the calculation are shown in Table 7.1. The analytical results of the resonance wavelength shift were obtained using Equations 7.31 under small particle approximation.

Table 7.1: Parameters for calculation.

Parameters	Values	Parameters	Values
$\hbar\omega_{p_0}$	9.03 eV [24]	f_5	4.384 [24]
$\hbar\omega_1$	0.415 eV [24]	$\hbar\Gamma_0$	0.053 eV [24]
$\hbar\omega_2$	0.830 eV [24]	$\hbar\Gamma_1$	0.241 eV [24]
$\hbar\omega_3$	2.969 eV [24]	$\hbar\Gamma_2$	0.345 eV [24]
$\hbar\omega_4$	4.304 eV [24]	$\hbar\Gamma_3$	0.870 eV [24]
$\hbar\omega_5$	13.32 eV [24]	$\hbar\Gamma_4$	2.494 eV [24]
f_0	0.760 [24]	$\hbar\Gamma_5$	2.214 eV [24]
f_1	0.024 [24]	A	0.13 [13]
f_2	0.010 [24]	v_F	1.41×10^6 m/s [13]
f_3	0.071 [24]	$1/\gamma_0$	9.3×10^{-15} s [13]
f_4	0.601 [24]	m_{eff}	9.108×10^{-31} kg [13]

7.4. RESULTS

Figure 7.5 shows the experimental and simulated results of the absorbance of 100 nm size gold NP suspensions. The spectra of the absorbance of gold NP in citrate buffer (100 nm diameter spherical gold NP, mean concentration 3.835×10^9 ml^{-1}), were obtained using a UV-Visible spectrometer (Lambda 35, Perkin Elmer), see the blue line in Figure 7.5 (a). The peak wavelength is 575 nm. This was compared with the simulated results for the same concentration and size gold NPs with the modified LD model with T-matrix method, which is shown with a green dashed dot line (peak wavelength 579 nm) respectively, both simulated results match the experimental result well. The RI of the medium is set as 1.33 which is the same as the RI of water as the major component of citrate buffer is water. The Scaffardi and Tocho's model [22] was also used as a comparison see the red dashed line (peak wavelength 562 nm).

The experimental results of the absorbance of gold NP suspension in the optical adhesive (Norland Optical Adhesive 146H, Norland Products, whose RI 1.46) is shown in Figure 7.5 (b) by a blue line. The gold NPs have been mixed into the optical adhesive with ultrasonic stirring as mentioned in the Methods Section. Scaffardi and Tocho's model [22] and the modified LD model are also used to show the simulated absorbance spectra with RI 1.46, which are shown by a red dashed line and a green dashed dot line respectively in Figure 7.5 (b) for the same mean gold NP concentration (3.835×10^9 ml^{-1}). Note: due to the low percentage of gold NPs transferred to the optical adhesive, the simulated results have been multiplied by a factor of 0.02 in order to show the results in the same scale. The peak wavelength of the experimental result with polynomial fitting is 592 nm, which is close to the simulated results both from Scaffardi and Tocho's model of 588 nm and from the modified LD model of 610 nm.

The simulated results with the T-matrix method have been compared with the solutions calculated by Mie theory and the errors beween them are quite small. Within the wavelength range from 500 nm to 650 nm, the errors are less than 0.3 %.

When moving the upper optical fibre end tip closer to the lower optical fibre end

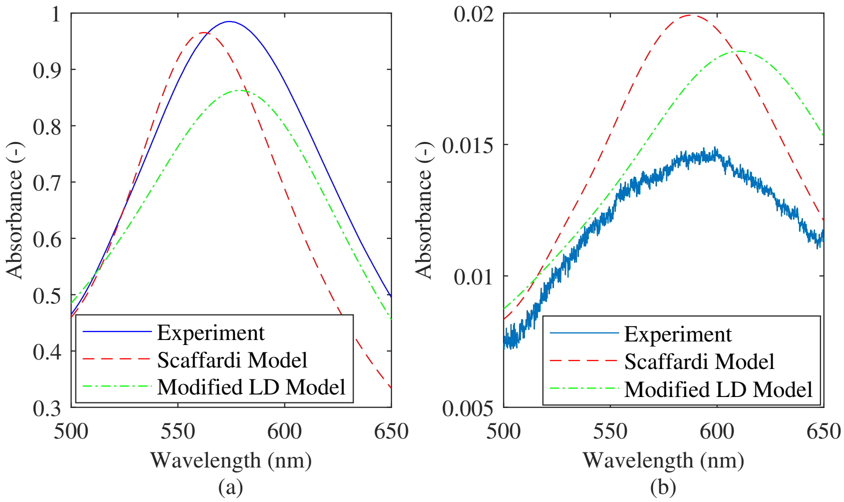

Figure 7.5: Experimental and simulated results of the absorbance of 100 nm size gold NP suspensions. (a) Gold NPs in water. (b) Gold NPs in the optical adhesive.

tip, as shown in Figure 7.4, there is a compressive force on the cured optical adhesive containing gold NPs. Figure 7.6 shows the experimental results of the transmittance and the absorbance for different position change values. The transmittance shown in Figure 7.6 (a) was obtained by dividing the transmitted light for the cured optical adhesive containing gold NPs by the intensity of the transmitted light intensity for only optical adhesive between the optical fibre end tips. The absorbance shown in Figure 7.6 (b) is obtained from the transmittance in Figure 7.6 (a). It can be seen from Figure 7.6 (b) that there is a blue shift when pressing the cured optical adhesive containing gold NPs.

Figure 7.7 (a) shows the peak wavelengths shift under compressive strain. The precision of obtaining the peak wavelengths depends on the method used for tracking the spectral peak and the noise level of the spectrum. In this work, the peak wavelengths were obtained from polynomial fittings. In order to reduce the influence of the noise on the peak values, the data were averaged by measurements. By averaging the data from multiple measurements, a more precise peak wavelength can be obtained. 50 measurements were used to check the deviation of the peak wavelength values obtained by polynomial fitting and the standard deviation is about 191.2 pm. The data shown in Figure 7.7 are the peak wavelengths obtained by the 8-order polynomial fittings with 400 measurements. In Figure 7.7 (a), the blue dots show the peak wavelengths with their position change values read directly from the 3-axis stage. The red dashed line shows the linear fit of the blue dots for a position change range from 0 µm to 100 µm in the yellow region of Figure 7.7 (a). The gradient of the fitting curve is 0.0464 nm/µm. It can be seen from Figure 7.7 (a) that the gradient is reduced for at a larger position change. This is because the lower optical fibre cannot withstand too much force when the compressive force is

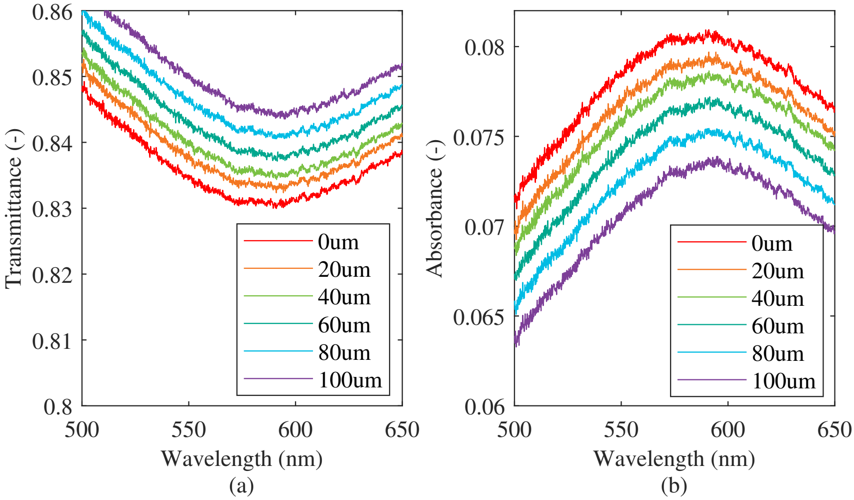

(a)

(b)

Figure 7.6: Experimental results of the spectra of gold NP in the cured optical adhesive under pressure (the position change of the upper optical fibre end tip is read from a 3-axis stage directed as shown in the legend). (a) Transmittance. (b) Absorbance.

high. The lower optical fibre's position will also move slightly. In order to reduce the effect from this movement, a microscope was used for the distance correction. The distance modification used two measurements. One is the original distance, the other is when the readout position changed by 100 µm. Each was measured 6 times. The orange dots in Figure 7.7 (a) are the modified results. The gradient of its linear fitting curve is 0.1328 nm/µm. The original distance between the two optical fibre end tips, before applying the compressive force, is 1.3505±0.0129 mm from the microscope. Based on the original distance, the peak wavelengths under different strain values were obtained as shown in Figure 7.7 (b). The red line is the linear fitting curve and its gradient is -0.1915 ± 0.1108 pm/µε with the peak wavelength 587.7 nm at strain 0. As shown in Figure 7.7 (b), the dynamic range of the setup is from about $-0.03\,\varepsilon$ to $0\,\varepsilon$. It is a large dynamic range but the setup only can apply compression on the sample. The theoretical dynamic range depends on the material used as the optical fibre. For fused silica, the dynamic range can be up to 4 % [29].

FEM has been previously used for the simulation of composites containing NPs [30] and the size of the NP is relatively large (100 nm), therefore an FEM simulation with the software Abaqus was used to determine the shape change of gold NP in the optical adhesive. Although the simulated results will have an error due to the restriction of the small size of the NPs, the simulated results are expected to approximate the behaviour of the NPs inside the optical fibre under strain change. This mechanical behaviour of the optical fibre containing NPs needs to be verified by experiment.

The Young's modulus of the medium (optical adhesive) is set as 10×10^{-5} nN/nm^2 as a typical value. Poisson's ratio of the optical adhesive is 0.43. From FEM, the

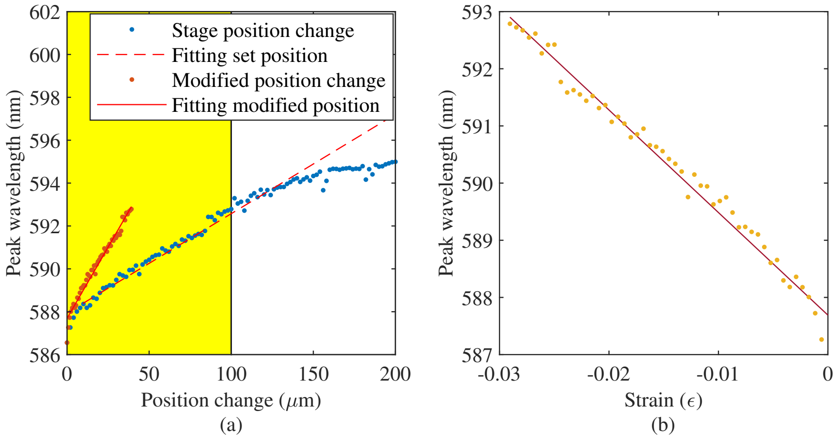

Figure 7.7: Peak wavelength shift under pressure. (a) The original peak wavelength shift (blue dots) and the modified shift (orange dots) with their linear fitting curves. (b) Peak wavelength shift under different strain values with the linear fitting curve.

shape change of the NP in the optical adhesive is 5-orders smaller than the shape change of the optical adhesive. Therefore, the shape change of the NP in the optical adhesive can be neglected mechanically. By adjusting the RI change of the optical adhesive in the simulation to match the gradient of the peak wavelength shift of the experimental result, the corresponding RI change of the optical adhesive is -0.52 ± 0.28 ppm/$\mu\varepsilon$.

A gold NP is expected to enhance the contrast ratio in the distributed sensing [5] for high sensitivity strain sensing. The case of a gold NP in fused silica is also calculated. The Young's modulus of the medium (fused silica) used in FEM is 73 nN/nm^2 [31] and the Poisson's ratio is 0.17 [32].

The RI change of fused silica can be taken into account in the T-matrix method by using the modified LD model to calculate the peak wavelength change ratio. The light propagating along the optical fibre sees the RI change of the fused silica is [33]

$$\Delta n = -\frac{1}{2} n^3 [(1-\nu')p_{12} - \nu' p_{11}]\epsilon, \tag{7.32}$$

where, ν' is the Poisson's ration for fused silica. For silica fibre at 633 nm incident light, $p_{11} = 0.113$, $p_{12} = 0.252$, [34] The RI change is -0.200 ppm/$\mu\varepsilon$ when $n = 1.45$.

For fused silica or some polymer materials, the RI range is in the range of 1.3 to 1.7. Figure 7.8 shows 4 cases in this RI range with the RI of the optical fibre of 1.35, 1.45, 1.55 and 1.65 in Figure 7.8 (a) to (d). Figure 7.8 is plotted based on the T-matrix method for a gold NP with the modified LD model under RI change of the medium (η) and NP shape change ratio (β) (with 116 Central Processing Units (CPUs) from the HPC cluster for about 1 day). The fitting wavelength range is from 550 nm to 650 nm. The wavelength interval is 0.1 nm. The RI change is from -10 ppm/$\mu\varepsilon$ to 10 ppm/$\mu\varepsilon$ with an interval of 0.5 ppm/$\mu\varepsilon$.

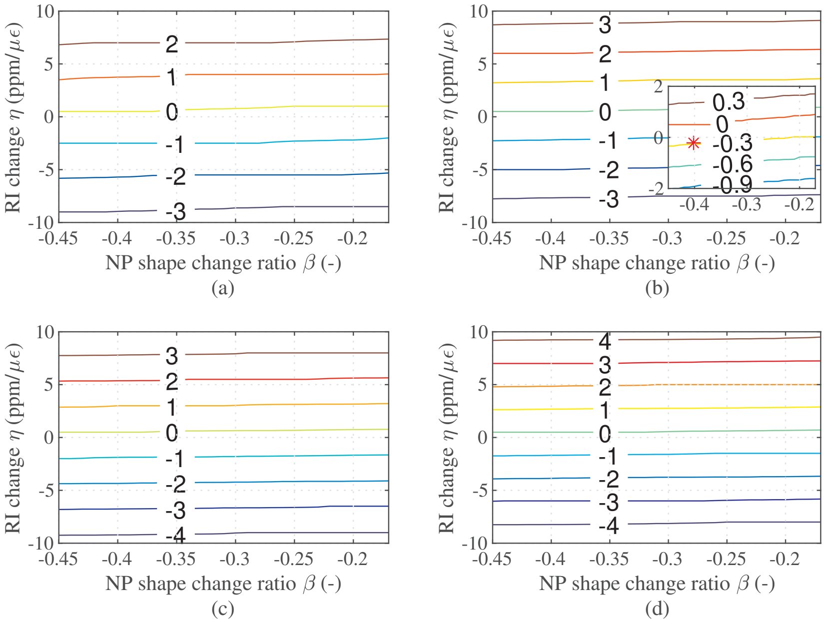

Figure 7.8: The peak wavelength change ratio in small strain (±0.001ε range linear fitting, $\alpha = 1$). The RI of the optical fibre in (a) - (d) are 1.35, 1.45, 1.55 and 1.65 respectively. The unit of the peak wavelength change ratio of the contour line is pm/$\mu\varepsilon$.

The NP shape change ratio is from -0.45 to -0.17 with an interval of 0.01. The peak wavelength change ratio is obtained by linear fitting of the peak wavelengths in a small strain range $-1000\,\mu\varepsilon$ to $1000\,\mu\varepsilon$ with the interval of $100\,\mu\varepsilon$.

It can be seen from Figure 7.8 that the RI change of the optical fibre is the main factor of the values of peak wavelength change ratio when compared with the NP shape change and shape change induced gold RI change as well. By comparing Figure 7.8 (a) to (d), it can be seen that when the RI of the medium increases the value of the peak wavelength change ratio becomes intense. The NP shape change will also modulate the peak wavelength change ratio slightly but it only becomes important when the RI change is around $0\,\text{ppm}/\mu\varepsilon$. The NP shape change in the range shown in Figure 7.8 shows a blue shift of the peak wavelength change, which can be seen more clearly in the embedded graph in Figure 7.8 (b). As shown in the embedded graph in Figure 7.8 (b), the peak wavelength shifts are not zero when the RI change η (RI change of the optical fibre) is zero. Figure 7.8 (b) shows the peak wavelength shift caused by the morphing of the gold NPs in the optical fibres. The peak wavelength shifts are influenced by the NP shape change ratios. Some commercial optical fibres are manufactured based on fused silica (RI of about 1.45) for their low loss especially in the telecom optical wavelength bands. For an example, a red star is plotted in Figure 7.8 (b) to show that when the ratio of length change of the NP to axial fused silica is 0.9208, the RI change is $-0.216\,\text{ppm}/\mu\varepsilon$, which corresponds to concentrations of NPs of $1.25 \times 10^{14}\,\text{ml}^{-1}$. Note: Figure 7.8 is plotted for relative strain change α between the optical fibre and the NP at 1. The advantage of using the factor 1 is that for other values of α it is simple to obtain the corresponding values by scaling. For examples, for other values of α, the RI change in Figure 7.8 only needs to be multiplied by $1/\alpha$ and the final result needs to be multiplied by α to obtain the corresponding peak wavelength change ratio when the NP longitude length change is $1\,\text{ppm}/\mu\varepsilon$. Therefore, the value of the red star plotted on Figure 7.8 (b) is $-0.282\,\text{pm}/\mu\varepsilon$ and after multiplication by α becomes $-0.260\,\text{pm}/\mu\varepsilon$.

Because the RI change of the optical fibre is the main factor of the values of peak wavelength change ratio, Equation 7.31 may be simplified when the change of RI and shape of the NPs are not taken into consideration. Then, Equation 7.31 may be simplified as

$$\left[\frac{\mathrm{d}\lambda}{\mathrm{d}l}\right]_{\lambda_0} = G\frac{\lambda_0^2}{2\pi c'}\frac{[\mathrm{d}F/(\mathrm{d}l/l)]_{\omega_{F\nu}}}{[\mathrm{d}F/\mathrm{d}\omega]_{\omega_{F\nu}}}, (G=1) \tag{7.33}$$

where,

$$\left[\frac{\mathrm{d}F}{(\mathrm{d}l/l)}\right]_{\omega_{F\nu}} = 4\epsilon_{m0}\eta. \tag{7.34}$$

and

$$\begin{aligned}\left[\frac{\mathrm{d}F}{\mathrm{d}\omega}\right]_{\omega_{F\nu}} &= \frac{2\omega_p^2\omega_{F\nu}}{(\omega_{F\nu}^2+\gamma^2)^2} + \frac{2f_0\omega_p^2\omega_{F\nu}}{(\omega_{F\nu}^2+\Gamma_0^2)^2} + \sum_{j=1}^{k}\frac{2f_j\omega_{p0}^2\omega_{F\nu}(\omega_j^2-\omega_{F\nu}^2)^2}{[(\omega_j^2-\omega_{F\nu}^2)^2+\omega_{F\nu}^2\Gamma_j^2]^2} \\ &\quad - \sum_{j=1}^{k}\frac{2f_j\omega_{p0}^2\omega_{F\nu}(\omega_j^2-\omega_{F\nu}^2)}{[(\omega_j^2-\omega_{F\nu}^2)^2+\omega_{F\nu}^2\Gamma_j^2]^2} + \sum_{j=1}^{k}\frac{f_j\omega_{p0}^2\omega_{F\nu}^2\Gamma_j^2}{[(\omega_j^2-\omega_{F\nu}^2)^2+\omega_{F\nu}^2\Gamma_j^2]^2} - \frac{2\omega_p^2\omega_{F\nu}}{(\omega_{F\nu}^2+\gamma_0^2)^2}.\end{aligned} \tag{7.35}$$

It can be seen from Equation 7.34 that η determines the sign of the ratio. The results from Equations 7.33 to 7.35 are shown in Figure 7.9 to make a comparison. The embedded graph shown in Figure 7.9 (b) shows the identical region shown in Figure 7.8 (b). The results become anti-symmetric around 0 because of the lacking of the influence caused by the RI change of gold. The red star is at the same position in Figure 7.8 (b). The approximated plasmon resonance wavelengths were calculated based on Equation 7.27. The features caused by the NP shape change are lost but the features caused by the RI change are maintained even though the values deviate from the values calculated by elaborated calculation shown in Figure 7.8.

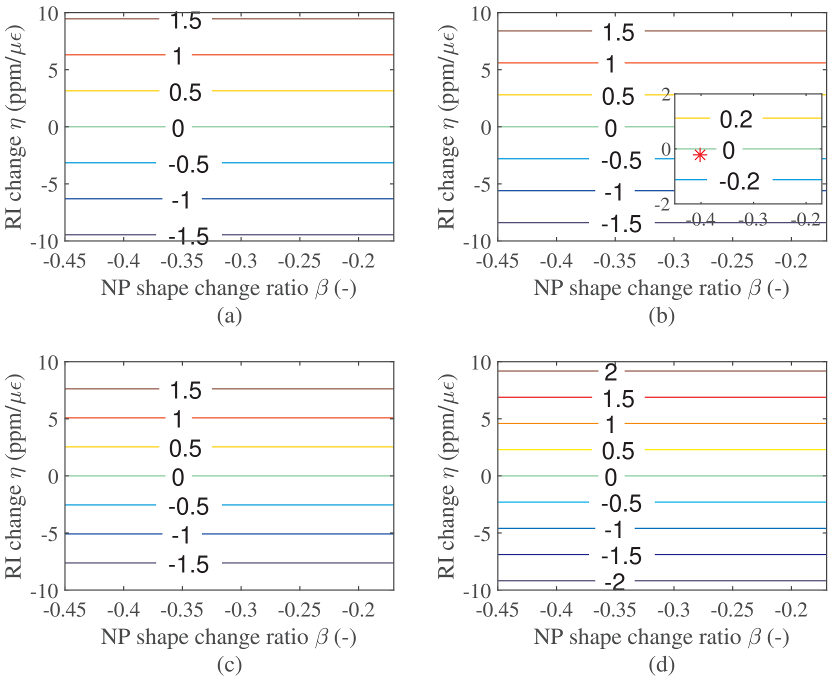

(a) (b) (c) (d)

Figure 7.9: Estimated peak wavelength change ratio. RI of the optical fibre in (a) - (d) are 1.35, 1.45, 1.55 and 1.65 respectively. The unit of the peak wavelength change ratio of the contour line is pm/με.

7.5. DISCUSSION

The modified LD model has been compared with the experimental results and the Scaffardi and Tocho's model in Figure 7.5. The modified LD model not only matches the experimental results and the Scaffardi and Tocho's model well for the spherical gold NP, but also can be used for the spheroidal NP under strain change. Compared with other methods, for example Scaffardi and Tocho's model or the Brendel-Bormann model, it does not exactly match the experimental results. However, the

LD model has a simpler expression and its derivative function is more explicit in order to derive the analytic expression under strain change.

From the modified LD model in this chapter, the plasmon resonance peak wavelength change ratio can be related to the shape change of the NP, the shape change induced RI change of the NP, the RI of the optical fibre and the RI change of the optical fibre. The Young's modulus and the Poisson's ratio and the concentration of the NP are also factors to adjust the values of the plasmon resonance peak wavelength change ratio. From Figure 7.8, it can be seen that the RI change is the major factor to influence the peak wavelength change ratio. Therefore, by choosing different materials for the optical fibre, the sensitivity of the plasmon resonance peak wavelength change can be tuned.

For a commercial fused silica based optical fibre or fibre Bragg grating, the strain induced peak wavelength change is about 1.2 pm/$\mu\varepsilon$ for about 1550 nm incident light. If the optical fibre properties are modified, especially by introducing a higher RI and photo-elastic coefficient of the optical fibre, a high sensitivity of the plasmon resonance peak wavelength change may be achieved. Compared with those for infrared light, detectors for the visible light are not expensive which is an advantage for the plasmon peak detection. For some metal NPs the plasmon peak is in the visible range.

In addition, the shape change of the NP will also change the peak wavelength change ratio, especially when the RI change is around 0. In this case, by choosing optical fibres with suitable Young's modulus and Poisson's ratio, the shape change of the NP can be tuned and then the peak wavelength change ratio can be tuned finely. Other face centred cubic materials for example silver, have a larger sensitively based on its shape change.

The simplified analytic equation for calculating the peak wavelength shift under strain can show the trend, but the values deviates from the exact calculation results shown in Figure 7.8 because the NP size is quite large. The calculated plasmon resonance wavelengths for RI of 1.35, 1.45, 1.55, 1.65 are 513 nm, 521 nm, 537 nm, and 550 nm respectively, which are also deviates from the peak wavelengths by fitting. However, it can be found that the results in Figure 7.9 match the results in Figure 7.8 well when the approximated results multiples a factor (G) of about 2. This indicates that a larger size of gold NP has a larger peak wavelength change response to the axial strain change. From simulations of gold and silver NPs for larger sizes (larger than 100 nm), the peak wavelength ratio will also increase slightly when the sizes of the NPs increase. Therefore, by using larger size gold NPs, the sensitivity will increase. However, the width of the peak wavelength will also increase which may cause a difficulty in determining the peak wavelength values.

For 100 nm size gold NP, there are a lot of atoms (about 245 atoms) along its diameter, so the Young's modulus and Poisson's ratio may be still appropriate for the calculation for this size safely. However, for smaller NPs especially several nanometer size NPs, the number of atoms is quite small and material parameters may vary from those of bulk materials, so for these small NPs this effect still needs to be investigated.

The temperature is also a factor which influences the strain sensing because the variation of temperature will cause the length change of the optical fibre and the RI change of both of the NPs and the optical fibre. This may cause a difficulty in decoupling the strain information and temperature information. In this chapter, it is assumed that the room temperature is constant. Therefore, the influence of the variation of the temperature needs to be investigated in the future. It can be noticed that the strain detection channels of the plasmon resonance based strain sensing and the traditional distributed fibre optic sensing based on Rayleigh backscattering is different, using visible light channel and near infrared channel respectively. By combining these two methods, the strain information may be decoupled from the temperature variation. There is a remarkable advantages of doping gold NPs over other oxide materials or fused silica fibre without doping NPs. Gold NP doped optical fibres generate plasmon resonance. This makes it possible to provide additional strain information by obtain the plasmon resonance shift. However, the method of spectral peak tracking with polynomial fitting is sensitive to the noise. Therefore, methods to precisely track the spectral peaks and methods for depressing the noise level in the measurements still need to be investigated.

7.6. CONCLUSION

This chapter can supplementally answer the main research question: How can the enhancement of light scattering used in distributed fibre optic sensing be an advantage for SHM? The plasmon resonance induced by the introduction of the gold NPs in the optical fibre can be used for strain detection based on the plasmon resonance spectral shift under strain. Due to the sensing wavelength range being different from typical distributed fibre optic sensing based on Rayleigh scattering, it may be an auxiliary strain detection method along with distributed fibre optic sensing based on Rayleigh scattering. In addition, by changing the shape of the NP, the type and size of the NP, and the materials of the optical fibre, the peak wavelength change ratio can be tuned. These can be beneficial for strain detection for SHM.

BIBLIOGRAPHY

[1] D. Tosi, C. Molardi, and W. Blanc, “Rayleigh scattering characterization of a low-loss MgO-based nanoparticle-doped optical fiber for distributed sensing”, *Optics & Laser Technology*, vol. 133, p. 106 523, 2021.

[2] V. Fuertes, N. Grégoire, P. Labranche, S. Gagnon, R. Wang, Y. Ledemi, S. LaRochelle, and Y. Messaddeq, “Engineering nanoparticle features to tune Rayleigh scattering in nanoparticles-doped optical fibers”, *Scientific Reports*, vol. 11, no. 1, pp. 1–12, 2021.

[3] A. Beisenova, A. Issatayeva, I. Iordachita, W. Blanc, C. Molardi, and D. Tosi, “Distributed fiber optics 3D shape sensing by means of high scattering NP-doped fibers simultaneous spatial multiplexing”, *Optics Express*, vol. 27, no. 16, pp. 22 074–22 087, 2019.

[4] A. Beisenova, A. Issatayeva, S. Korganbayev, C. Molardi, W. Blanc, and D. Tosi, “Simultaneous distributed sensing on multiple MgO-doped high scattering fibers by means of scattering-level multiplexing”, *Journal of Lightwave Technology*, vol. 37, no. 13, pp. 3413–3421, 2019.

[5] X. Wang, R. Benedictus, and R. M. Groves, “Optimization of light scattering enhancement by gold nanoparticles in fused silica optical fiber”, *Optics Express*, vol. 29, no. 13, pp. 19 450–19 464, 2021.

[6] S. Jayabal, A. Pandikumar, H. N. Lim, R. Ramaraj, T. Sun, and N. M. Huang, “A gold nanorod-based localized surface plasmon resonance platform for the detection of environmentally toxic metal ions”, *Analyst*, vol. 140, no. 8, pp. 2540–2555, 2015.

[7] C. Shen, Y. Zhang, W. Zhou, and J. Albert, “Au-coated tilted fiber Bragg grating twist sensor based on surface plasmon resonance”, *Applied Physics Letters*, vol. 104, no. 7, p. 071 106, 2014.

[8] X. Zhang, J. Chen, Á. González-Vila, F. Liu, Y. Liu, K. Li, and T. Guo, “Twist sensor based on surface plasmon resonance excitation using two spectral combs in one tilted fiber Bragg grating”, *Journal of the Optical Society of America B*, vol. 36, no. 5, pp. 1176–1182, 2019.

[9] B. Han, Y. N. Zhang, X. Wang, D. Yang, Y. Liu, J. Sun, and Y. Wang, “High-sensitive fiber anemometer based on surface plasmon resonance effect in photonic crystal fiber”, *IEEE Sensors Journal*, vol. 19, no. 9, pp. 3391–3398, 2019.

[10] J. Garca, D. Monzón-Hernández, J. Manrquez, and E. Bustos, “One step method to attach gold nanoparticles onto the surface of an optical fiber used for refractive index sensing”, *Optical Materials*, vol. 51, pp. 208–212, 2016.

[11] J. Cao, E. Galbraith, T. Sun, and K. Grattan, “Comparison of surface plasmon resonance and localized surface plasmon resonance-based optical fibre sensors”, in *Journal of physics: Conference series*, IOP Publishing, vol. 307, 2011, p. 012 050.

[12] V. Amendola, R. Pilot, M. Frasconi, O. M. Marago, and M. A. Iati, “Surface plasmon resonance in gold nanoparticles: A review”, *Journal of Physics: Condensed Matter*, vol. 29, no. 20, p. 203 002, 2017.

[13] X. Qian and H. S. Park, “The influence of mechanical strain on the optical properties of spherical gold nanoparticles”, *Journal of the Mechanics and Physics of Solids*, vol. 58, no. 3, pp. 330–345, 2010.

[14] W. Cai, H. Hofmeister, and M. Dubiel, “Importance of lattice contraction in surface plasmon resonance shift for free and embedded silver particles”, *The European Physical Journal D-Atomic, Molecular, Optical and Plasma Physics*, vol. 13, no. 2, pp. 245–253, 2001.

[15] J. Lerme, M. Pellarin, E. Cottancin, M. Gaudry, M. Broyer, N. Del Fatti, F. Vallee, and C. Voisin, “Influence of lattice contraction on the optical properties and the electron dynamics in silver clusters”, *The European Physical Journal D-Atomic, Molecular, Optical and Plasma Physics*, vol. 17, no. 2, pp. 213–220, 2001.

[16] W. Somerville, B. Auguié, and E. Le Ru, “Accurate and convergent T-matrix calculations of light scattering by spheroids”, *Journal of Quantitative Spectroscopy and Radiative Transfer*, vol. 160, pp. 29–35, 2015.

[17] W. Somerville, B. Auguié, and E. Le Ru, “Smarties: User-friendly codes for fast and accurate calculations of light scattering by spheroids”, *Journal of Quantitative Spectroscopy and Radiative Transfer*, vol. 174, pp. 39–55, 2016.

[18] S. I. Ranganathan and M. Ostoja-Starzewski, “Universal elastic anisotropy index”, *Physical Review Letters*, vol. 101, no. 5, p. 055 504, 2008.

[19] J. Cao, T. Sun, and K. T. Grattan, “Gold nanorod-based localized surface plasmon resonance biosensors: A review”, *Sensor. Actuat. B-Chem.*, vol. 195, pp. 332–351, 2014.

[20] C. F. Bohren and D. R. Huffman, *Absorption and scattering of light by small particles*. John Wiley & Sons, 1998.

[21] G. N. Greaves, A. Greer, R. S. Lakes, and T. Rouxel, “Poisson’s ratio and modern materials”, *Nature Materials*, vol. 10, no. 11, pp. 823–837, 2011.

[22] L. B. Scaffardi and J. O. Tocho, “Size dependence of refractive index of gold nanoparticles”, *Nanotechnology*, vol. 17, no. 5, pp. 1309–1315, Feb. 2006.

[23] P. B. Johnson and R.-W. Christy, “Optical constants of the noble metals”, *Physical Review B*, vol. 6, no. 12, p. 4370, 1972.

[24] A. D. Rakić, A. B. Djurišić, J. M. Elazar, and M. L. Majewski, “Optical properties of metallic films for vertical-cavity optoelectronic devices”, *Applied Optics*, vol. 37, no. 22, pp. 5271–5283, 1998.

[25] M. I. Mishchenko, L. D. Travis, and A. A. Lacis, *Scattering, absorption, and emission of light by small particles*. Cambridge University Press, 2002.

[26] W. Somerville, B. Auguié, and E. Le Ru, “A new numerically stable implementation of the T-matrix method for electromagnetic scattering by spheroidal particles”, *Journal of Quantitative Spectroscopy and Radiative Transfer*, vol. 123, pp. 153–168, 2013.

[27] W. R. Somerville, B. Auguié, and E. C. Le Ru, “Simplified expressions of the T-matrix integrals for electromagnetic scattering”, *Optics letters*, vol. 36, no. 17, pp. 3482–3484, 2011.

[28] F. Xu and A. B. Davis, “Derivatives of light scattering properties of a non-spherical particle computed with the T-matrix method”, *Optics letters*, vol. 36, no. 22, pp. 4464–4466, 2011.

[29] W. B. Hillig, “Strength of bulk fused quartz”, *Journal of Applied Physics*, vol. 32, no. 4, pp. 741–741, 1961.

[30] Y. Hua, L. Gu, and H. Watanabe, “Micromechanical analysis of nanoparticle-reinforced dental composites”, *International Journal of Engineering Science*, vol. 69, pp. 69–76, 2013.

[31] H. McSkimin, “Measurement of elastic constants at low temperatures by means of ultrasonic waves–data for silicon and germanium single crystals, and for fused silica”, *Journal of Applied Physics*, vol. 24, no. 8, pp. 988–997, 1953.

[32] P. Vlugter and Y. Bellouard, “Elastic properties of self-organized nanogratings produced by femtosecond laser exposure of fused silica”, *Physical Review Materials*, vol. 4, no. 2, p. 023 607, 2020.

[33] C. D. Butter and G. Hocker, “Fiber optics strain gauge”, *Applied Optics*, vol. 17, no. 18, pp. 2867–2869, 1978.

[34] A. Bertholds and R. Dandliker, “Determination of the individual strain-optic coefficients in single-mode optical fibres”, *Journal of Lightwave Technology*, vol. 6, no. 1, pp. 17–20, 1988.

8

CONCLUSION AND RECOMMENDATIONS

This research, development of highly scattering distributed fibre optic sensing for structural health monitoring, is focused on answering the main research question 'How can the enhancement of light scattering used in distributed fibre optic sensing be an advantage for SHM?'. This dissertation can be summarised as follows: First of all, doping gold nanoparticles into the core of the optical fibres was chosen to enhance the backscattered light in the optical fibres at the beginning of this work. However I had to deal with the difficulty of doping nanoparticle to optical fibres in an optical laboratory. The method of dropping refractive index matching liquid containing gold nanoparticles was investigated to evaluate the backscattered light by the NPs coupled into the optical fibres with experiments and with simulations. Further simulations about optimisation sizes of the gold NPs doped into the core of the optical fibres were investigated. The optimised sizes and concentrations of gold NPs were obtained to enhance the backscattered light within desired penetration depths. Besides investigation of increasing light intensity by gold NPs, the characteristics of the backscattered light spectra from gold NPs and the spectral shift under strain with different gauge lengths and concentrations were investigated in order to show the response of backscattered light spectra to strain. The sensitivity of the strain detection with the gold NP-doped optical fibre sensors were investigated later by case study. At the end, the side effect caused by doping gold NPs, plamsmon resonance, were investigated under strain to make it an advantage for strain detection used for SHM. Figure 8.1 gives a graphic guideline of this work and some points which are used to direct the readers to the relevant chapters for more information.

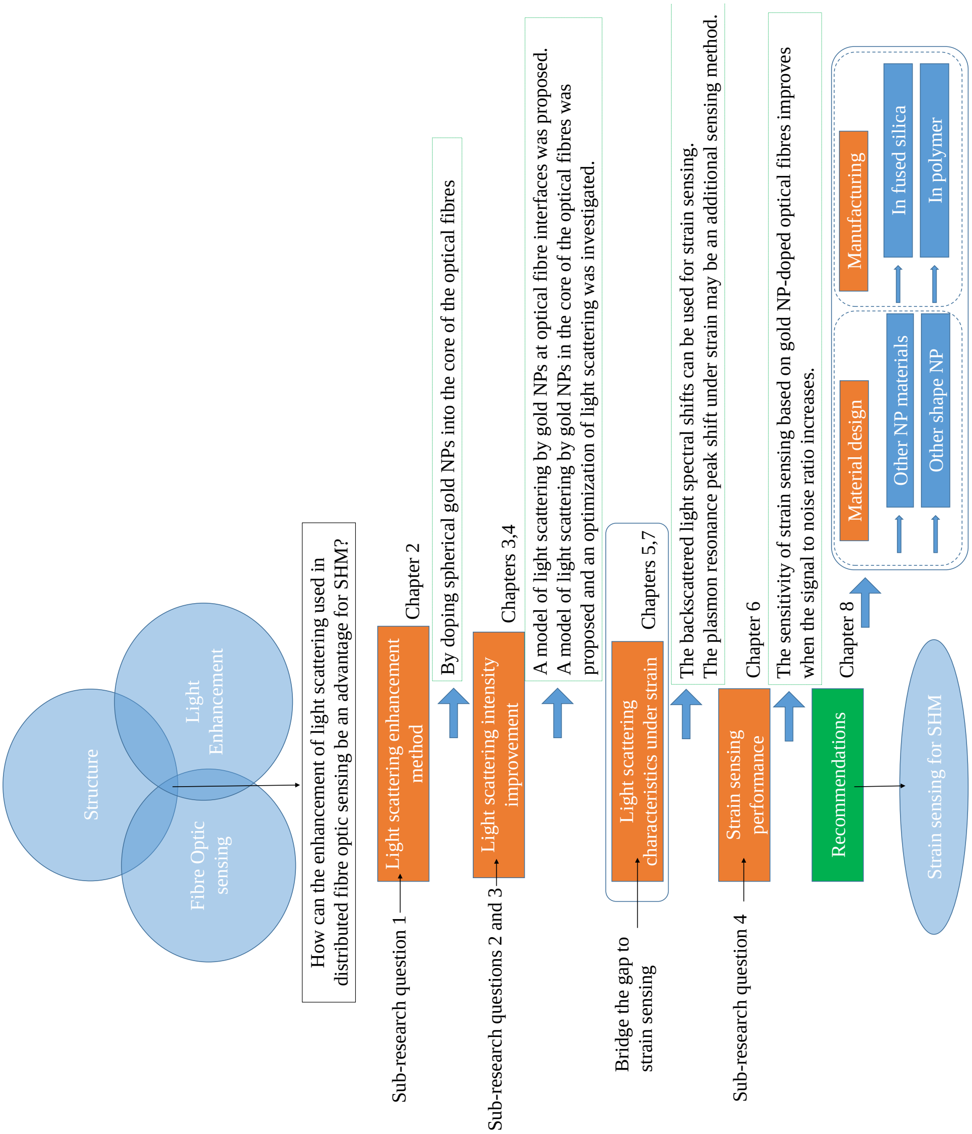

Figure 8.1: The final guideline of this dissertation. This research starts at the joint point of multiple disciplines and mainly based on fibre optic sensing and light enhancement technique. To answer the main research question 'How can the enhancement of light scattering be an advantage for SHM?', sub-research questions need to be answered and gaps need to be bridged. Some points have be listed for these chapters in the green dash frames. For the recommendation part, the blue dash frame is used to distinguish between work that has been done and work for the future.

Here are some conclusions for the proposed research questions which are assembled from this dissertation. Some recommendations are provided for potential research that can follow by this work.

8.1. CONCLUSIONS TO THE PROPOSED QUESTIONS

Question 1:

What are the potential methods to enhance the intensity of scattered light in optical fibre in distributed fibre optic sensing detected based on the conventional LUNA interrogator available in the laboratory?

`Answer:`

Damaging the core of the optical fibres with exposing UV laser, making nano structures with fs-IR laser in the core of the optical fibres, and doping NPs into the core of the optical fibres become the major methods used for backscattered light enhancement for distributed fibre optic sensing based on Rayleigh backscattering in recent years. They used the LUNA interrogator to demodulate strain from backscattered light spectra.

Question 2:

If nanometre to micrometre size particles are introduced into an optical fibre, what is the intensity characteristic of the scattered light in optical fibre with these particles?

`Answer:`

10 nm to 400 nm diameters of spherical gold NPs have been investigated for NP-doped optical fibre sensors. Small size (<100 nm) gold NPs induce high absorption which can be a drawback for the sensors based on backscattering. The optimised sizes for light scattering enhancement have been obtained by consideration of the penetration depth or without considering the penetration depth. For 1550 nm incident light, the best size of gold NPs for light enhancement is around 315 nm if the penetration depth is not taken into consideration. If the penetration depth is taken into consideration the optimised size of gold NPs is about 224 nm.

8

Question 3:

The increased scattered light is also likely to reduce the transmission of light along the optical sensing fibre. What is the optimised scattering increase at some key areas?

`Answer:`

By introducing the penetration depth restriction for NP doped fibre optic sensors, the transmission loss is reduced to 3 dB for the whole NP doped optical fibre. For 1550 nm incident light, the optimised size of gold NPs is about 224 nm. It can achieve up to about −36 dB/mm backscattering intensity by doping 224 nm diameter gold NPs with concentrations of $1.51 \times 10^9\,\mathrm{mL}^{-1}$, $1.51 \times 10^8\,\mathrm{mL}^{-1}$, $1.51 \times 10^7\,\mathrm{mL}^{-1}$ with the penetration depths of 10 mm, 100 mm and 1000 mm, respectively. Compared with commercial optical fibres (about −100 dB/mm [1]), the increase is about 64 dB/mm.

Question 4:

What is the effect of the sensitivity change and their effect for SHM for material?

`Answer:`

The sensitivity change can be evaluated by the following equation:

$$Sensitivity = \frac{1}{\sqrt{SNR}}\left[\frac{5.9246}{L} + 14.3808\right]/1.24\ [\mu\epsilon], \tag{8.1}$$

where, L is the gauge length in centimetre, SNR is the signal to noise ratio of the electrical signals obtained from light signals. It can be seen from the equation that the standard deviation is proportional to the reciprocal of the square root of SNR. By increasing the SNR, the sensitivity of the strain detection will be improved. Damage (for example cracks) causes local strain change. By improving the sensitivity of the strain detection, the damage might be diagnosed earlier.

Main research question:

How can the enhancement of light scattering used in distributed fibre optic sensing be an advantage for SHM?

`Answer:`

By spectral analysis of the gold NP doped optical fibre, the NP doped optical fibres have similar spectral shift behaviour under strain compared with FBGs or distributed strain sensing based on Rayleigh scattering. Doping gold NPs into the core of the optical fibres has the advantage of enhancing the backscattered light in the optical fibre dramatically. The increased signals induce the increasing of the SNR then the sensitivity of the distributed fibre optic sensing based on Rayleigh scattering will be improved, which is beneficial to strain based SHM. The plasmon resonance spectrum from gold NPs can be used as an auxiliary strain detection method along with distributed fibre optic sensing based on Rayleigh scattering due to the sensing wavelength range being different from typical distributed fibre optic sensing based on Rayleigh scattering.

8.2. RECOMMENDATIONS FOR FUTURE WORK

The research in this thesis shows the potential of gold NP doped optical fibre sensors for SHM. However, to apply the gold NP doped optical fibre sensors to the real application in industry still needs much more work. More efforts should be paid on further research about the other characteristics of the NP doped sensors (for example, temperature properties and birefringence of NP doped sensors) and especially the techniques for manufacturing of the sensors. There are some recommendations for future work:

The influence from the fluctuation of temperature is not taken into account in this work. It is assumed that the sensors are used in the room temperature and the temperature is constant. However, the environmental temperature may change. Therefore, the spectral characteristics of NP doped optical fibre under temperature change would be a separate study, if the thermal expansion of gold and the optical fibre needs to be taken into consideration as the refractive index change of gold and the optical fibre under temperature change need to be taken into account.

The axial strain is applied on the optical fibre sensors. Birefringence of the NP doped optical fibre would be a study in the future to obtain the strain differences in transverse directions .

Although most of the parts of this thesis are focused on simulations, a lot of attempts of experiments have been implemented during the PhD research. In order to reduce the scattered light from the interfaces of the optical fibres, gold NPs were transferred to refractive index matching liquid (see [2]) but the efficiency of transferring gold NPs to the liquid needs to be improved. Gold NPs were mixed into an optical adhesive and by UV lamp curing the adhesive to make it a point sensor, but the NPs generally combine as clusters, so the dispersion methods need to be investigated.

Manufacturing gold NP doped optical fibre is a challenge for an optical laboratory. Our ideal at present is to dope gold NPs to PMMA (Poly(methyl methacrylate)) optical fibres. Firstly, PMMA filaments containing gold NPs need to be manufactured. Secondly, drawing the NP doped PMMA optical fibre from the filament via a 3D printer. Lastly, the PMMA fibre sensors need to be enbedded or attached to the surface of the materials. The adhesive to attach the optical fibre to the material or materials themselves around the optical fibre can be the cladding of the optical fibre. If the process of printing the NP doped optical fibre sensors is in the process of manufacturing of the materials, the NP doped optical sensors would be integrated as a part of the structures. Figure shows a PMMA optical fibre (about 600 µm diameter) drawn from a 3D printer in the Aerospace Structures and Materials department in TU Delft.

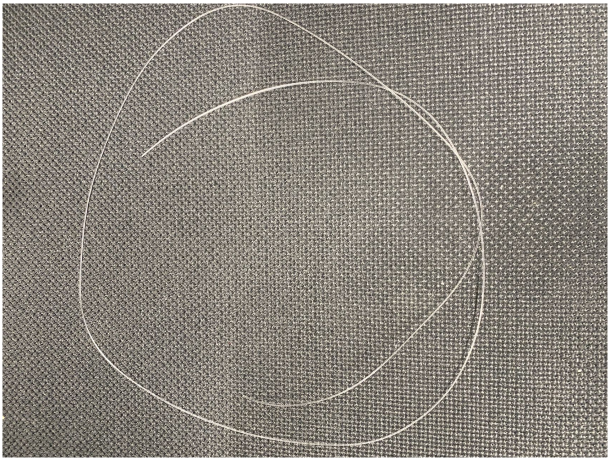

Figure 8.2: A photo of a PMMA optical fibre drawn from a 3D printer.

BIBLIOGRAPHY

[1] P. Lu, S. J. Mihailov, D. Coulas, H. Ding, and X. Bao, “Low-loss random fiber gratings made with an fs-IR laser for distributed fiber sensing”, *Journal of Lightwave Technology*, vol. 37, no. 18, pp. 4697–4702, 2019.

[2] X. Wang, R. Benedictus, and R. M. Groves, “Light scattering and rheological effects in an optical fibre coupled nanoparticle suspension”, in *Optical Sensing and Detection VI*, International Society for Optics and Photonics, vol. 11354, 2020, p. 113540V.

ACKNOWLEDGEMENTS

First of all, I would like to thank Prof. Rinze Benedictus and Dr. Roger M. Groves. You gave me the opportunity to start my PhD research in TU Delft.

Secondly, I would like to thank our secretory Gemma, you helped me complete the documents to come to the Netherlands, arranged the workplace, ordered the computer, and helped me solve many problems during the PhD research. Thanks to your help, my PhD journey became smoother.

I would like to thank the academic staff members in Aerospace Structures and Materials (ASM) group. I would like to thank my second supervisor Calvin Rans. Thank you for meeting with me and for providing relevant potential background for my research. I would like to thank Andrei, John, Durga, Marlies. You gave me support in the laboratory to accelerate my experiments. I would like to thank Atsushi Nagai. You accompanied me every afternoon in a whole week in the Chemistry laboratory and told me the secret of success of becoming a chemist. I would like to thank Kunal Masania. Thank you for providing 3D printers for me to draw PMMA optical fibre containing gold nanoparticles. You also gave me fantastic ideas that can be implemented in the future. Thank you Sybrand for talking about metal nanoparticles. It is my pleasure be acquainted with Vahid, John-Alan, Dimitrios, Clemens, Marianne, Michiel, Sofia, Baris, Baris, Julie, Jos, Bilim, Amin and other staff members in the ASM group.

I would like to thank the NDT group members. Andrei, Nan, Pratik, Dmitry, Michael, Ali, Nakash, Luigi, Sebastian, Vincentius, Lu, Chirag, Pedro, Aydin, Muping and other group members. We had NDT colloquiums and badminton activities together. We joined the precision fair, Day of Photonics events and Dutch Photonics Events together.

I would like to thank Agnes, Bram, Camila, Nitesh, Nicolas, Ozan, Ioannis, Jesse, Morteza, Megan, Chantal, Eva, Davide, Satya, Silvia, Deniz, Ujala, Chizoba, Ranjan, Muhamad, Stratos, Thanasis, Shankar, Francesco and other ASM student members and visiting student members. We enjoyed lunch at the canteen, attended PhD events and PhD drinks. Thank you so much Huub for revising my PhD thesis's summary's Dutch version.

I would like to thank my Chinese friends. Thank you Nan Tao, Nan Yue, Lubin, Yuzhe, Hongwei, Xi, Wenjie, Zhiyuan, Yuqian, Ximan, Jun, Wenli, Haoran, Yu, Peng, Ran, Qianqian, Shichen, Xiaodong, Xiaopeng, Qiuyu and other Chinese friends. Thank you Tian, Xianfeng for the trip to Belgium for the first Christmas holiday in my PhD journey. Thank you Lubin, Shichen for the trip to Rome after the Go/NoGo meeting. Thank you Xianfeng, Tian, Lubin, Shuo, Dengxiao, Shanshan, and Yang for the 500-kilometre cycling and camping trip from Delft to the northern island above Groningen in the Netherlands. Thank you Kaisheng, Ming, Jingna, Guanqun, Yanan, Dong, Ji, Wencan and Yifu for the trips around Europe.

Most of the time of my PhD study was spent in the workplace NB0.38 in the Faculty of Aerospace Engineering. I would like to thank my roommates in my workplace. Thank you Hongwei, Nakash, Caroline, Sasan and Giovanna. The pringles collection on the top of the cabinet recalls me the good old-days.

I would like to show my appreciate to my daily supervisor Roger. You guided me in my PhD research. You are knowledgeable and patient and helped my develop my research skills step by step. During my PhD research, you gave me solid support and provided me the opportunities to participate in conferences (SPIE Photonics Europe, SPIE Optical Metrology, Photon) and summer schools (Siegman International School on lasers etc.) to build broad academic networks.

In addition, I would like to show my appreciate to all of my committee members. Thank you Prof. dr. Alfredo Güemes, Prof. dr. Simon Watson, Prof. dr. Bernhard Brandl, Associate Prof. dr. ir. Richard Loendersloot and Associate Prof. dr. ir. Silvania Pereira. Thank you for accepting to be the independent members of my PhD defence committee and taking the time to read my thesis. It is my honour for you to participate in my PhD defence.

At the end of the acknowledgements, I would like to express my gratitude to my parents. Without your support, I cannot complete my PhD.

Xiang Wang
Delft, February 2023

CURRICULUM VITÆ

Xiang Wang was born in July 1991 in Jiangsu Province, China. He obtained his Bachelor's Degree in Applied Physics in Tianjin University of Technology and obtained his Master's Degree in Optical Engineering in Beihang University in China. From 16th November 2018, he started his PhD study in Aerospace NDT Laboratory in Aerospace Structure and Materials department in the Faculty of Aerospace Engineering in Delft University of Technology in the Netherlands. His supervisors are Prof. dr. ir. Rinze Benedictus, Dr. Roger Groves and Dr. Calvin Rans. His research is focused on the development of highly scattering fibre optic sensing for structural health monitoring.

LIST OF PUBLICATIONS

JOURNALS

5. **Xiang Wang**, Yuzhe Xiao, Calvin Rans, Rinze Benedictus, and Roger M. Groves, *Case study of strain acquisition of gold nanoparticle-doped distributed optical fibre sensing based on backscattering*, (under review).

4. **Xiang Wang**, Rinze Benedictus, and Roger M. Groves, *Spectral characteristics of gold nanoparticle doped optical fibre under axial strain*, Scientific Reports **12**, (2022): 16593.

3. **Xiang Wang**, Rinze Benedictus, and Roger M. Groves, *Plasmon resonance based gold nanoparticle doped optical fibre strain sensing*, Optics and Laser Technology **159**, (2022): 108272.

2. **Xiang Wang**, Rinze Benedictus, and Roger M. Groves, *Optimization of light scattering enhancement by gold nanoparticles in fused silica optical fiber*, Optics Express **29**, 13 (2021): 19450-19464.

1. **Xiang Wang**, Rinze Benedictus, and Roger M. Groves, *Modelling of light scattering by gold nanoparticles at optical fibre interfaces*, Journal of Optics (United Kingdom) **23**, 3 (2021): 035602.

CONFERENCES

4. **Xiang Wang**, Rinze Benedictus, and Roger M. Groves, *Influence on the backscattered spectra of gold nanoparticle doped optical fibres for different sensing lengths and nanoparticle concentrations*, Photon (2022). (abstract and oral presentation)

3. **Xiang Wang**, Rinze Benedictus, and Roger M. Groves, *Plasmon resonance spectral peak shift due to morphing of gold nanoparticles for strain sensing*, SPIE Photonics Europe (2022). (conference paper and oral presentation)

2. **Xiang Wang**, Rinze Benedictus, and Roger M. Groves, *Light scattering by gold nanoparticles cured in optical adhesive at optical fibre interface*, SPIE Optical Metrology (2021). (conference paper and oral presentation)

1. **Xiang Wang**, Rinze Benedictus, and Roger M. Groves, *Light scattering and rheological effects in an optical fibre coupled nanoparticle suspension*, SPIE Photonics Europe (2020). (conference paper and oral presentation)

EVENTS

2. **Xiang Wang** and Roger M. Groves. Poster: *Development of highly scattering distributed fibre optic sensing for structural health monitoring*, won DutchPhotonicsEvent '**Best Poster Presentation Award**' (2022).

1. Amit Reza, Ajay Tiwari, Fernando Mendonca Filho, Remko Fermin and **Xiang Wang**, *Inverted astronomy: high resolution seabed imaging from the ocean surface*, Proceedings Physics with Industry (2021).

MAGAZINES

1. **Xiang Wang**. *Gold nanoparticle highly scattering optical fibres for structural health monitoring*, Photonics Magazine Netherlands (Fotonica Magazine) (2022).